LISA CHEN

Flavour Dependence of Hadroproduced Charm-Strange Mesons

Robert Jedicke

University of Toronto
Toronto, Canada

© Copyright by Robert Jedicke 1991

Table of Contents

The E769 Tagged Photon Spectrometer Collaboration

Dedication

Statement of Contribution to E769

Abstract

Table of Contents

List of Figures

List of Tables

Introduction

Chapter 1

The Theory of Hadroproduction of Charm 1

Introduction 1

Overview 1

Parton-Parton Cross Sections 4

Parton Distribution Functions 7

Total Cross Sections 11

Differential Cross Sections 15

Chapter 2

Accelerators and Beamlines 28

Production of the FNAL 800 GeV protons 28

The P-East beamline 29

Chapter 3

The E769 Detector 32

The Differential Isochronous Self-Collimating Cerenkov Counter (DISC) 33

Theory 33

DISC Physical Characteristics and Electronics 34

DISC Operation and Performance 40

DISC Off-line Analysis 46

The Transition Radiation Detector (TRD) 47

Theory, Design and Construction 47

System Performance 50

The E769 segmented target 54

The Downstream SMD system 57

General Properties 57

System Performance and Efficiency 59

The Downstream PWC system 60
The Drift Chamber System 60
Physical Characteristics including the Gas System 60
Calibration and On-line Monitoring 67
Off-line Analysis, Alignment and Performance 68
The Analysis magnets 73
Cerenkov Counters 73
Physical Characteristics 73
Cerenkov Performance and Data Analysis 76
Cerenkov Kaon Efficiency 77
Electromagnetic Calorimetry 79
Hadronic Calorimetry 82
The E769 Trigger System 85
The Data Acquistion System 88
E769 Data Format 90
ON-line monitoring 92
The DAP/CDP system 93
The INTERSPILL System 95
GPIG and the E769 Event Display 95
Chapter 4
Reconstruction, Strip and Analysis Code 97
PASS 0 97
PASS 1 98
PASS 2 and Data Summary Tapes 98
The Pair Strip 99
The $\varphi\pi$ and K^*K sub-strips 101
Chapter 5
The E769 Monte Carlo 109
Chapter 6
Results and Discussion 116
Cross Section × Branching Ratio and Total Cross Section Measurements 118
Differential Cross Section Measurements 121
Chapter 7
Conclusions 127
APPENDIX A 129
E769 D_s Cross Section Measurement 129

The E769 Tagged Photon Spectrometer Collaboration

G.A. Alves[a], J.C. Anjos[a], J.A. Appel[b], S.B. Bracker[f], L.M. Cremaldi[d], R. Dixon[b], D. Errede[h], H.C. Fenker[b], C. Gay[f], D.R. Green[b], R. Jedicke[f], D. Kaplan[e], P.E. Karchin[i], I. Leedom[e], L.H. Lueking[b], P.M. Mantsch[b], J. Metheny[g], R. Milburn[g], H. da Motta[a], A. Napier[g], A. Rafatian[d], W. Ross[i], A.F.S. Santoro[a], M. Sheaff[h], W.J. Spalding[b], C. Stoughton[b], M.H.G. Souza[a], M.E. Streetman[b], D. Summers[b], Z. Wu[i]

[a] Centro Braseleiro de Pesquisas Fisicas (CBPF), Rio de Janeiro, Brazil

[b] Fermi National Accelerator Laboratory (FNAL), Batavia, Illinois, USA

[c] Instituto de Fisica Teorica (UNESP), Sao Paulo, Brazil

[d] University of Mississippi, Oxford, Mississippi

[e] Northeastern University, Boston, Massachusetts, USA

[f] University of Toronto, Toronto, Ontario, Canada

[g] Tufts University, Medford, Massachusetts, USA

[h] University of Wisconsin, Madison, Wisconsin, USA

[i] Yale University, New Haven, Connecticut, USA

Dedication

To my wife Victoria who patiently waited while "only two more years" of work turned into four,

To my father who taught me through example that there is more to life than money and intellectualism,

To my brother Peter for long, late night, philosophical conversations about astronomy and physics ever since I was a young boy,

To my mother and sister for their pride in me and my work and boosting my ego even when I didn't need it,

To Roger Dixon for daily afternoon meetings where I had some of the most interesting conversations of my days at Fermilab,

To Jeff Appel and Jeff Spalding for help in all manners and especially with understanding drift chambers,

To Lee Lueking for his down-home Nebraska, easy going, Type B personality, friendly ways and conversations that didn't have anything to do with physics,

To Chris Stoughton, a fellow Scooper's Fan, Silicon Graphics Expert, and singing referee,

To Helio da Motta for teaching me the meaning of puxe socu,

To Greg Sellberg and John Gran for their easy laughs and technical expertise,

To Tony Key for making the University of Toronto Physics Department a better place for graduate students,

To Dr. Dean Gaily, Dr. Graham Rose, 'Uncle' Bill Imrie, and Krsyztov Sliwa, for teaching me physics, politics in physics, football and more physics,

To all the unmentioned people who contributed in many ways to this mammoth undertaking,

and, finally, to the Right Honourable Prime Minister Brian Mulroney for doing one hell of a job.

Formulation of the E769 Cross Section measurement 129
Detailed calculation of the elements of the Probability Matrices 137
Calculation of the corrected beam particle ratios for NON-DISC tagged beam... 137
Calculation of the number of incident $\pi'/K'/p'$ 138
Correcting TRDGB for Upstream Interactions 140
Correcting TRDGB for multi-particle bucket occupancy and KB Livetime..... 142
Calculation of the contamination of the K' beam 146
Calculation of the contamination of the π' beam 146
Calculation of the contamination of the p' beam 149
Elimination of duplicate events and events from bad runs and spills 150
APPENDIX B 154
Calculating Statistical and Systematic Errors in the D_s Cross Section 154
APPENDIX C 158
The Maximum Likelihood fit 158
List of Publications 162
List of Published Talks presented by E769 members 162

List of Figures

The $\pi/K/p \rightarrow N \rightarrow$ charm $\rightarrow$ observable particles process....2
The LO charm producing q-annihilation and gg-fusion diagrams....4
NLO $gq \rightarrow QQq$ Feynman diagrams....6
parton-parton cross sections at LO and NLO....7
A) Proton parton distributions B) Pion parton distributions....8
Kaon quark distribution functions of El Hassouni and O. Napoly....10
The variation of the total charm cross section with CM energy for π, K and p beams....12
The variation of the total charm cross section with CM energy for kaons....13
The various elements of the NLO $\pi p \rightarrow$charm cross section....14
LO π and p induced charm quark x_F distributions....16
LO kaon induced charm quark x_F distributions....17
LO p_T^2 distributions for π and p induced charm quarks....18
LO p_T^2 distributions for K induced charm quarks....19
The relationship between x and x_F for various values of p_T^2....22
5 different Fragmentation Functions used in this analysis....23
The differential x_F distribution after fragmentation with the functions of Kartvelishvili et al., Peterson et al., and Collins and Spiller for π induced D_s....25
Schematic of the PE beamline....30
Scale View of the E769 Spectrometer....32
Schematic View of the E769 Spectrometer....33
DISC Pressure Vessel and Gasline Schematic....35
DISC Counting Room Gas Distribution Schematic....36
DISC Electronics....37
DISC Optical Assembly....39
DISC Phototube coincidences....39
Fitted DISC Pressure Curve....40
Elements of the fit to the DISC Pressure Curves....41
Particle Peak Pressure vs. Temperature in DISC....43
Pion Contamination level vs. Pressure Offset from Kaon Peak....44
DISC efficiency vs. Pressure Offset from Kaon Peak....45
Schematic of one of the E769 TRD radiator-chamber assemblies....49
Fitted TRD plane distribution for positive data....51
DISC PMT coincidences vs. TRD plane counts....51
π probability as a function of p probability....52
TRD pion contamination and Efficiency....53
The E769 target and counter/scintillator arrangement....55
Schematic construction of a SMD plane....58
Primary vertex z-location using SMD tracks....59
Drift Chamber Sense and HV plane orientation....61
Orientation of the U, X, and V planes in the DC system....62
Schematic View of the Drift Chamber Electronic Readout system....66
Drift Chamber TDC time distribution with EAT....68
The effect of the DC velocity correction on DC residuals....70
Drift Chamber Measured Plane Efficiencies and Resolutions....71
D1-1X hole....72
C1 and C2 Light paths....75
Example of plots used in Cerenkov Kaon efficiency Analysis....78
Cerenkov Kaon Efficiency calculated from data....79
SLIC radiator-scintillator assembly....81

Schematic of the Hadrometer 83
Weighting Scheme for the ET trigger 86
Schematic of the E769 Data Acquisition System 89
Basic Configuration of the Online Monitoring System 94
Various cuts used in the Pair and subsequent Strips 100
Efficiency and Signal to background as a function 104
Schematic representation of the angle q in resonant Ds decays 106
Schematic representation of the DIP and ISO cuts 107
The ratio of the MC to data D^+ x_F distribution 110
The ratio of the MC to data D^+ p_T^2 distribution 111
Acceptance corrected x_F distributions for the D^+ signal 112
Acceptance corrected p_T^2 distributions for the $D^\pm$ signal 113
MC x_F distribution of charm quarks and the D_s mesons they produce 114
MC x_F (D_s) / x_F(charm) 114
MC p_T^2 distribution of charm quarks and the D_s mesons they produce 115
Final combined $D_s \rightarrow \phi\pi$ and $D_s \rightarrow K^*K$ signals 116
$D_s \rightarrow \phi\pi$ and $D_s \rightarrow K^*K$ signals 117
x_F acceptance as calculated from the MC 122
p_T^2 acceptance as calculated from the MC 122
Background subtracted, acceptance corrected D_s x_F and p_T^2 distribution 124
Schematic view of the Scaler system applicable to Livetime calculations 142
$\text{LIVETIME}_{\text{KILLER}}$ as a function of TRDGB (beam rate) 144

List of Tables

(π/K/p)p charm quark cross sections at 250GeV for all x_F 14
Summary of fits to LO differential charm quark distributions 20
n for D_s differential x_F distributions after fragmentation 26
Secondary collimator hole sizes and beam parameters at the DISC 31
DISC PMT logical conditions 38
E769 Expected and Measured Beam Composition 44
Aggregrate Properties of the Segmented Target 55
Specifications of the Segmented Target 56
SMD Vertex Detector Summary 57
D1 Sense Wire plane Characteristics 63
D2 Sense Wire plane Characteristics 64
D3 Sense Wire plane Characteristics 64
D4 Sense Wire plane Characteristics 65
Parameters of the DC holes in both Positive and Negative beam 72
E769 Cerenkov Counter Thresholds 74
Summary of important Scalers 91
A simplified/schematic view of the E769 Trigger system 92
Pair Strip Cuts 99
Cuts used in the $\varphi\pi$ and K^*K sub-strips 103
Number of D_s decays divided into incident particle and trigger types (x_F>0.0) 118
σ(nucleon)×B for x_F>0.0 assuming A^1 and $A^{0.95\pm0.05}$ 119
σ(nucleon)×B for all x_F assuming A^1 and $A^{0.95\pm0.05}$ 120
σ(nucleon) assuming A^1 and $A^{0.95\pm0.05}$ for limited and all x_F 120
Ratios of the K and p cross sections to the pion cross section for D_s production 121
Maximum Likelihood fits to $(1-x_F)^n$ and $\exp(-bp_T^2)$ 125
Inelastic and Total Nucleon Cross Sections at 250 GeV 135
Materials and Interaction Lengths Upstream of the target 142
Cuts for determining Bad spills, tapes and runs 151
Values Used in the Ds Cross Section Determination for x_F>0.0 156
Values Used in the Ds Cross Section Determination for x_F>0.0 157
Coefficients of the fits to the Acceptance Functions 161

Introduction

During the 1987-88 fixed target running period at the Fermi National Accelerator Laboratory in Batavia, IL, Experiment 769 wrote more than 10,000 nine-track data tapes containing the details of approximately 400 million beam-target interactions. The 250GeV mixed hadronic beam (π, K and p) of both polarities was tagged using a Differential Isochronous Self-Collimating Cerenkov counter and a Transition Radiation Detector. It interacted in a target assembly consisting of 26 target foils. The target contained four different elements (Be, Al, Cu and W) in roughly equal proportion in order to determine the A-dependence of charm production.

The E769 spectrometer consisted of a vertex telescope of 11 Silicon Microstrip Detector planes, 35 Drift Chamber planes and two Proportional Wire Chamber planes, two magnets, two threshold Cerenkov Counters, an Electromagnetic and Hadronic Calorimeter and a muon wall following a one metre thick additional steel shield. A low bias trigger on the transverse energy of the event gave a rejection of about three while enhancing the amount of charm on tape by about 40% relative to what would have been obtained using only an interaction trigger. The Data Acquisition system could write approximately 500 events s^{-1} at about 40% dead time. About 2/3 of the offline reconstruction was performed on a set of Advanced Computer Project (ACP) parallel processor modules, while much of the rest of the reconstruction was performed on Silicon Graphics R2000 workstations. Reconstruction required a full year's worth of CPU time on these systems and was equivalent to about 165 VAX 11/780 years of computing.

Analysis of this data sample yields 1841±73 $D^+ \rightarrow K^-\pi^+\pi^+$ decays, 1330±61 $D^o \rightarrow K\pi$ decays, 83±13 $D_s^+ \rightarrow K^+K^-\pi^+$ decays as well as numerous other decays. All references to a particular decay mode refer to both the stated and the charge-conjugate mode unless otherwise noted. It will provide the world's best A-dependence measurement for open charm production as well as production distributions for the three different beam particles. This study attempts to determine if there is a difference in the production properties of the

D_s meson by different beam particles (often referred to as a flavour dependence). D_s meson production is particularly interesting in π and K beams since both the K and D_s contain a strange quark while the π does not.

We describe the determination of the average $\sigma \times B$ (cross section $\times$ branching ratio) for two resonant decay modes of the D_s ($D_s \rightarrow \phi\pi$, $\phi \rightarrow KK$ and $D_s \rightarrow K^*K$, $K^* \rightarrow K\pi$ where we normalize $B(D_s \rightarrow K^*K)$ to $B(D_s \rightarrow \phi\pi)$) for each of the three different beam particles. We find an average $\sigma \times B$ of $0.036 \pm 0.015 \mu b$/nucleon, $0.044 \pm 0.018 \mu b$/nucleon and $0.035 \pm 0.025 \mu b$/nucleon in the π, K and p beams respectively for $x_F > 0$ and an $A^{0.95 \pm 0.05}$ nuclear dependence. Using the world average for the branching ratio[1] for the $D_s \rightarrow \phi\pi$ mode of 0.027 ± 0.007, the cross section for production of D_s by each of our three beam particles (π, K, p), averaged over decay modes, are $1.3 \pm 0.6 \mu b$/nucleon, $1.6 \pm 0.8 \mu b$/nucleon and $1.3 \pm 1.0 \mu b$/nucleon respectively for $x_F > 0$ and for $A^{0.95 \pm 0.05}$. The quoted errors are the combined statistical and systematic errors. The ratio of the $K \rightarrow D_s$ to $\pi \rightarrow D_s$ cross section is 1.2 ± 0.7 assuming that common systematic errors cancel.

A maximum likelihood fit to the x_F and p_T^2 distributions for the sample of D_s mesons produced in the π and K beam to functions of the form $(1-x_F)^n$ and $\exp(-bp_T^2)$ respectively yields $n=3.1 \pm 1.0$ and $b=1.1 \pm 0.3$.

We find no evidence of a flavour dependence in the production of the D_s meson in the total and differential cross sections.

---

1 M. Aguilar-Benitez, The Particle Data Group, 1990 Review of Particle Properties, Physics Letters B239, p.VII.128.

Statement of Contribution to E769

E769 was a complex experiment operated by a small group of people. Although this had its disadvantages, it did allow me to make a significant contribution to the commissioning and operation of the experiment as well as to the data analysis. In particular, under the mentorship of Roger Dixon (FNAL) I was responsible for the DISC - an entirely new detector in the TPL spectrometer. This included designing and building the gas, electronic and readout systems for the instrument as well as writing the code used for operating the Differential Isochronous Self-collimating Cerenkov counter (DISC). During data analysis I was responsible for writing and implementing the code which used the results of the DISC counter for beam particle identification. It was natural at that point to assume responsibility for utilizing the Transition Radiation Device (TRD) in beam particle identification and writing the code to merge the results of the DISC and TRD for a final beam particle identification.

I was also responsible for commissioning the 6000 channel Drift Chamber (DC) system with the helpful advice of Jeff Spalding (FNAL). Twenty of the thirty-five Drift Chamber planes were painstakingly cleaned and checked for damage. I commissioned the electronic readout system with minor modifications to the system left by E691. A large part of the readout system work involved implementing new code to test and readout the DCs using new, Fermilab built, CAMAC readout modules.

During data analysis I developed the matrix method for calculating the E769 cross sections as described in Appendix A and B of this thesis. This method is now used in other E769 analyses. I wrote the code to implement the method. I was the only experimenter studying the production of D_s mesons in our experiment. I developed all of the code used to generate the plots shown in the theory section of this report.

Abstract

Experiment 769 at the Tagged Photon Laboratory of the Fermi National Accelerator Laboratory wrote approximately 400×10^6 events to tape from the reactions of a tagged hadronic beam consisting of π, K and p. The interactions took place within a foil target assembly including targets of W, Be, Cu and Al. We use the D_s meson to determine if there exists a dependence of the production properties of the meson on the incident beam particle flavour. A total sample of 83±13 D_s mesons in the $\phi\pi$ and K^*K decay modes yields 29±8, 15±5 and 5.6±4.2 D_s mesons using only the transverse energy trigger for the π, K and p beams respectively. This is the world's largest sample of kaon induced D_s mesons. This indicates an average $\sigma\bullet B$ (normalizing $B(D_s\rightarrow K^*K)$ to $B(D_s\rightarrow\phi\pi)$) over the two modes of 0.036±0.015μb/nucleon, 0.044±0.018μb/nucleon and 0.035±0.025μb/nucleon for each of the three different beam particles respectively using $A^{0.95\pm0.05}$ for $x_F>0$. These values are consistent with recent measurements by the ACCMOR collaboration at CERN. The absolute cross sections for production of D_s by each of the three beam particles are calculated using the world average of the branching ratio to the $\phi\pi$ decay mode. Assuming that all systematic errors cancel, the ratio of the K to π absolute D_s production cross section is found to be 1.2±0.7 for $x_F>0$. The x_F and p_T^2 distributions of the D_s mesons for all three beam particles are also presented. All of these results are compared to QCD predictions as well as the LUND Monte Carlo. The differential distributions are consistent to within errors with other experimental results. We find no evidence for a flavour dependence of the production of the D_s meson in the total and differential cross sections.

Chapter 1: The Theory of Hadroproduction of Charm

Introduction

The goal of this thesis is to examine whether a flavour-dependence of the charm cross section manifests itself in the production of the D_s meson through (π/K/p)N interactions. In this case, a flavour dependence is simply a difference in the production of a D_s meson depending on the type of incident beam particle. A flavour dependence study of D_s production is particularly interesting with a π and K beam since the D_s and K both contain a strange quark while the π does not. E769 is well suited to this measurement since it uses an incoming 250GeV tagged beam of π, K and p. If it is possible to measure the total and differential cross sections precisely enough for the three different beam particles it will be possible to confront theory with data. This chapter deals with the theoretical framework of the production of the charm quark and charmed mesons.

Overview

Hadronic production of heavy flavours including charm is described by the perturbative theory of Quantum Chromo-Dynamics (QCD)[2,3,4]. QCD gives the prescription for calculating the basic parton-parton cross sections as a power series expansion in $\alpha_s(\mu)$. The quantity α_s is the strong coupling constant and μ is an arbitrary energy scale which should be chosen to be of the order of the energy of the hard scattering process producing the heavy quark. A full solution for the cross section would be independent of μ but any partial solution will have a residual dependence on the energy scale. The utility of the power series expansion relies on $\alpha_s(\mu)$ being much less than unity in order that the series converge quickly, since each successive term in the calculation becomes increasingly more difficult to calculate. At the energy scale of charm quark production α_s is still large

---

2 R.K. Ellis, FERMILAB-Conf-89/168-T, August 9, 1989.
3 P. Nason, S. Dawson and R.K. Ellis, Nuclear Physics B303 (1988), p. 607.
4 P. Nason, S. Dawson and R.K. Ellis, Nuclear Physics B327 (1989), p. 49-92.

(~0.3 in this analysis). This, as well as an ambiguity in the choice of the renormalization scale and the charm quark mass, leads to uncertainties in the theoretical calculation of the charm cross section. These problems are highlighted by recent extensions of the QCD Leading Order (LO) calculations (Ellis, ref. 2) to the Next-to-Leading Order (NLO) level (Nason, Dawson and Ellis, ref. 3 and 4) showing that the calculated cross section increases by about a factor of three.

The production of heavy quarks is illustrated in FIGURE 1.1. Only the LO calculation of the cross section will be discussed in detail here. The interaction can be divided into three pieces: the two incoming particles with given parton distribution functions, the parton-parton hard scattering process which produces the charm quark pair, and the hadronization (or fragmentation) of the heavy quarks into observable particles.

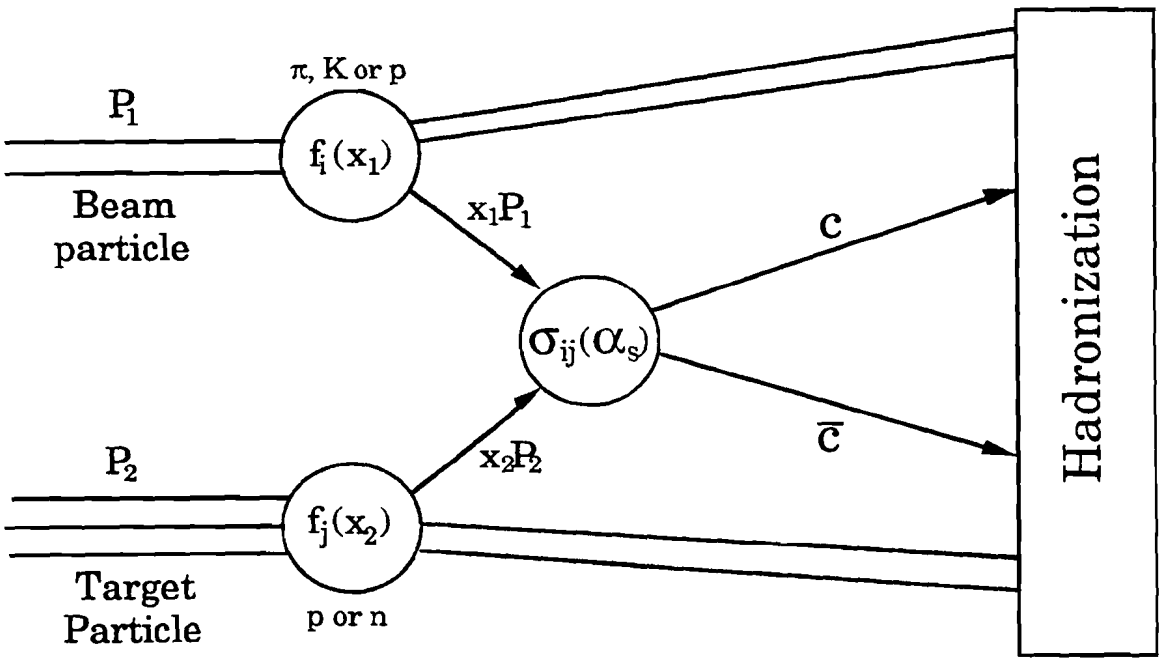

FIGURE 1.1
The π/K/p $\rightarrow$ N $\rightarrow$ charm $\rightarrow$ observable particles process

The total cross section (σ) for the interaction of two hadrons with incoming momenta P_1 and P_2 to produce a heavy quark pair is described by the following equation (Ellis, ref. 2):

$$\sigma(P_1,P_2) = \sum_{i,j} \int dx_1 dx_2 f_i(x_1,\mu) f_j(x_2,\mu) \hat{\sigma}_{ij}(\alpha_s(\mu), x_1P_1, x_2P_2)$$

where x_1 or x_2 is the fraction of the incoming particle's momentum carried by the interacting parton. The functions f_i and f_j represent the parton momentum distributions (the probability that parton i carries a fraction x_1 of the first particle's momentum) which must also be evaluated at the energy scale of the interaction. The hadronization of these heavy quarks into observable particles is a distinctly non-perturbative process and has not been calculated analytically. The description of this process is reserved for later in this discussion.

A flavour dependence (a difference in cross section for the production of the same particle by different incident particles) of the cross section might arise at any one of the three stages of the interaction. In particular, comparing the cross section for kaon to pion production of charmed particles, one might expect that since the strange quark is heavier than the up and down quarks it would affect the parton momentum distribution functions within the incoming kaon. At the parton-parton interaction level the presence of a heavier valence s-quark in the kaon alters the cross section when the strange quark participates directly in the interaction. Theoretical calculations ignore the masses of the three lighter quarks (u, d and s) and therefore do not make any predictions for such a flavour dependence. Finally, in the hadronization of the quarks, the presence of a s-quark in the kaon might change the manner in which the heavy quarks 'dress' themselves once produced. Modern fragmentation functions do not allow for any interaction between the spectator quarks (valence quarks in the incoming particles which do not participate directly in the heavy quark producing reaction) and the heavy quarks.

The following sections of this chapter deal successively with each of the elements of the total and differential (x_F and p_T^2) cross section measurements. I examine the theoretical predictions for the cross sections for (π/K/p)p interactions and the sensitivity of the Kp cross sections to changes in the kaon's gluon distribution function.

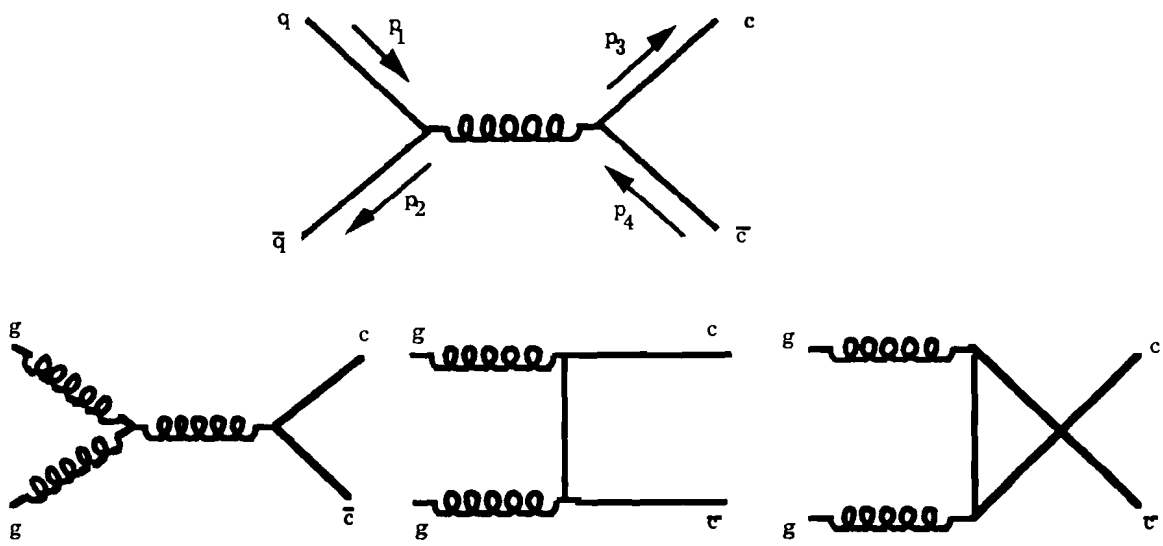

FIGURE 1.2
The LO charm producing q-annihilation and gg-fusion diagrams.

Parton-Parton Cross Sections

The quark level diagrams in LO perturbative QCD charm quark production are the quark-annihilation and gluon-gluon fusion diagrams shown in FIGURE 1.2. The parton-parton cross sections for these diagrams can be calculated using:

$$d\hat{\sigma}_{ij} = \frac{1}{2s}\frac{d^3p_3}{(2\pi)^3 2E_3}\frac{d^3p_4}{(2\pi)^3 2E_4}(2\pi)^4\delta^4(p_1+p_2-p_3-p_4)\overline{\sum|M_{ij}|}^2$$

where $(2s)^{-1}$ is the flux factor for massless incoming particles, $\overline{\sum|M_{ij}|}^2$ is the invariant matrix element squared for the parton sub-processes where the colour and spin indices have been averaged (summed) over the initial (final) states, and the other terms are the

phase space factors for 2→2 scattering (Ellis, ref. 2). The four momenta p_1 and p_2 are for the two incoming partons while p_3 and p_4 represent the four momenta of the outgoing heavy quarks. The matrix elements for the diagrams in FIGURE 1.2 have been calculated (Ellis, ref. 2) and are:

$$\overline{\sum \left|M_{gg\to c\bar{c}}\right|^2} = \frac{4}{9}(4\pi\alpha_s)^2\left(\tau_1^2+\tau_2^2+\frac{\rho}{2}\right)$$

$$\overline{\sum \left|M_{q\bar{q}\to c\bar{c}}\right|^2} = \frac{1}{144}(4\pi\alpha_s)^2\left(\frac{8}{\tau_1\tau_2}-18\right)\left(\tau_1^2+\tau_2^2+\rho+\frac{\rho^2}{4\tau_1\tau_2}\right)$$

where the number of colours has been set to 3 and

$$s=(p_1+p_2)^2 \qquad \tau_1=\frac{2p_1\cdot p_3}{s} \qquad \tau_2=\frac{2p_2\cdot p_3}{s} \qquad \rho=\frac{4m^2}{s}$$

where m is the mass of the charm quark and $\sqrt{s}$ is the parton-parton Centre of Mass (CM) energy.

We can integrate $d\hat{\sigma}_{ij}$ over all momenta and find that the parton-parton cross section may be written as (Ellis, ref. 2):

$$\hat{\sigma}_{ij}=\frac{\alpha_s^2(\mu)}{m^2}F_{ij}\left(\rho,\frac{\mu^2}{m^2}\right)$$

The dimensionless function F_{ij} has a perturbative expansion in the strong coupling constant:

$$F_{ij}\left(\rho,\frac{\mu^2}{m^2}\right)=f_{ij}^{(0)}(\rho)+4\pi\alpha_s(\mu)\left[f_{ij}^{(1)}(\rho)+\bar{f}_{ij}^{(1)}(\rho)\ln\left(\frac{\mu^2}{m^2}\right)\right]$$

where the NLO contributions ($f_{ij}^{(1)}$) have also been included. If we define

$$\beta=\sqrt{1-\rho}$$

$$\Im(\beta)=\frac{1}{\beta}\ln\left(\frac{1+\beta}{1-\beta}\right)-2$$

then the LO elements of the F_{ij} function are:

$$f_{q\bar{q}}^{(0)}(\rho) = \frac{\pi\beta\rho}{27}(2+\rho)$$
$$f_{gg}^{(0)}(\rho) = \frac{\pi\beta\rho}{576}\left\{3\left[\rho^2 + 16(\rho+1)\right]\Im(\beta) + 12(1+\rho) + \rho(6\rho-9)\right\}$$
$$f_{gq}^{(0)}(\rho) = f_{g\bar{q}}^{(0)}(\rho) = 0$$

In NLO calculations the processes shown in FIGURE 1.2 must be corrected for both real and virtual gluon emission (Ellis, ref. 2). A new class of diagrams involving gq interactions appears at the NLO level. The Feynman diagrams which contribute to the gq→QQq (QQ is

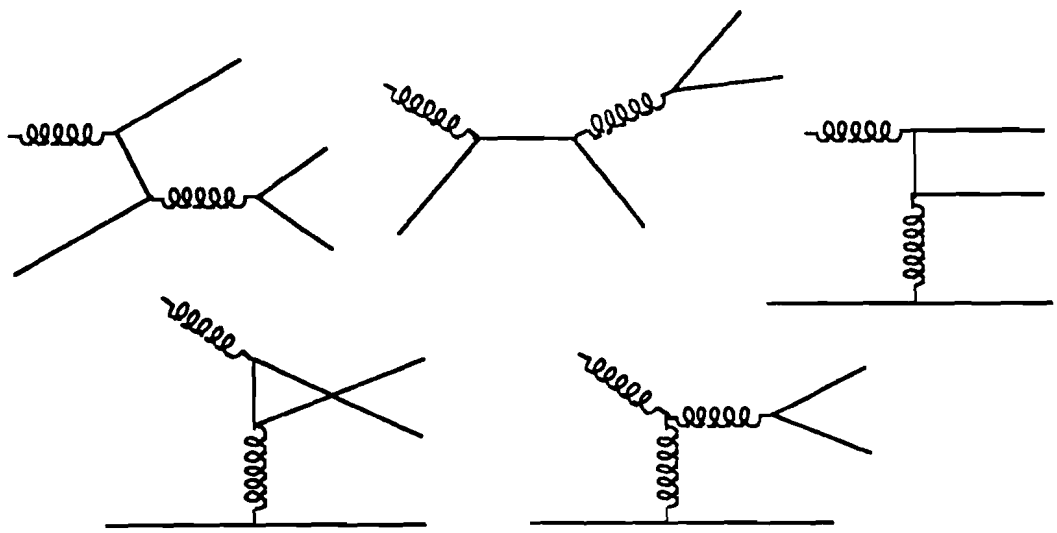

FIGURE 1.3
NLO gq→QQq Feynman diagrams

the heavy charm quark pair) process are shown in FIGURE 1.3. A full calculation of all of these terms has been made (Nason, Dawson and Ellis, ref. 3). All of the parton-parton cross section functions at the LO and NLO levels are plotted in FIGURE 1.4 as a function of ρ^{-1} ($=x_1x_2S/(4m^2)$) where S ($=m_\pi^2+m_p^2+2E_{beam}m_p$) is the square of the CM energy ($\sqrt{S}$~21.7GeV in E769) of the interacting hadrons. m_π and m_p are the masses of the pion and proton respectively while E_{beam} is the beam energy. In our experiment the maximum

ρ^{-1} (when $x_1=x_2=1$) was ~52. Most of the charm cross section is due to interactions at $\rho \sim 1$ because this is where the parton-parton interactions have their highest luminosity.

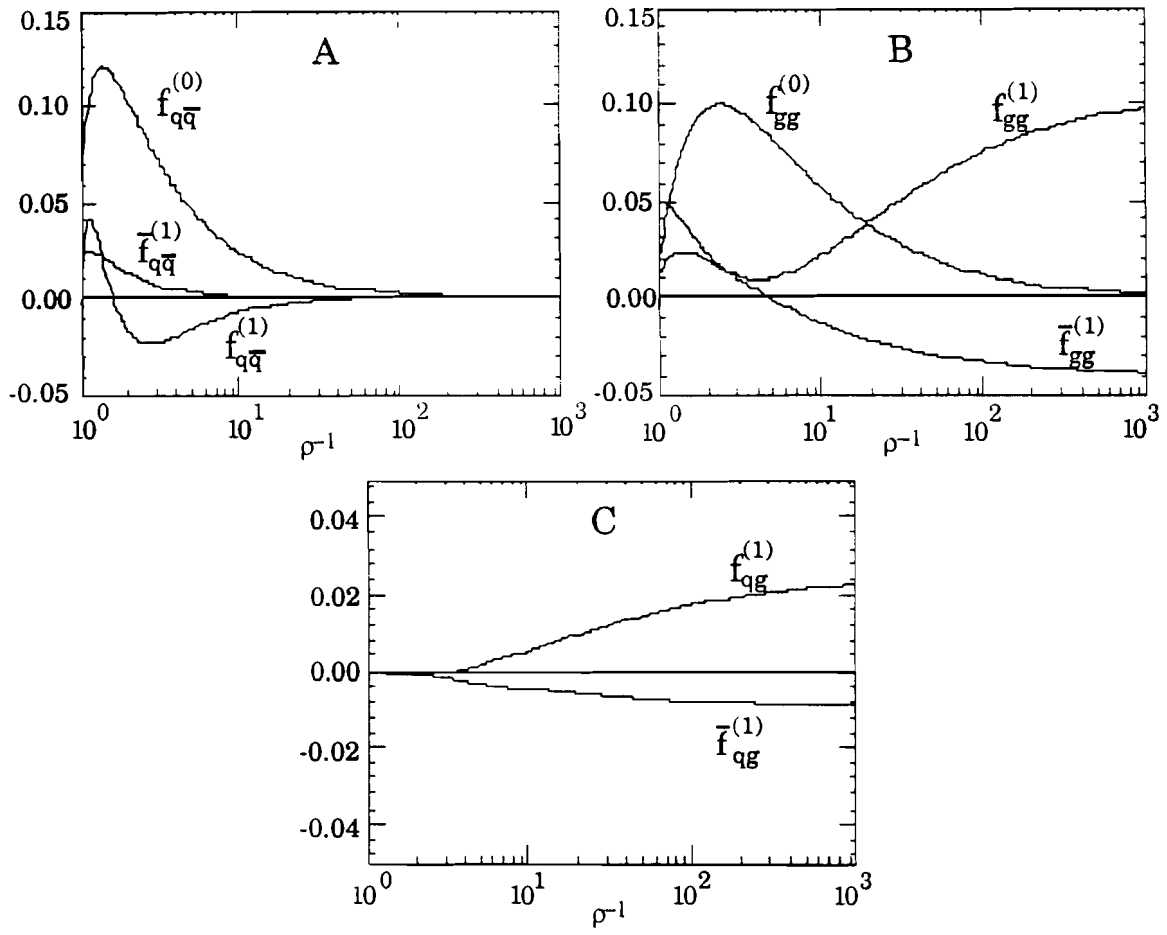

FIGURE 1.4
parton-parton cross sections at LO and NLO
A) qq annihilation B) gg fusion C) qg fusion

Parton Distribution Functions

Although the energy and momenta of two interacting hadrons may be well known the energy and momenta of the interacting partons within them is not known. The parton distribution functions give the probability density for finding a particular parton inside the hadron with a given fraction (x) of the hadrons momentum.

There are many possible choices for parameterizations of the parton distributions in pions, protons and neutrons.[5,6 7] These parameterizations are based on fits to Deep-Inelastic Scattering (DIS) experiments, di-lepton pair-production and the x_F distributions of the J/ψ. In order to be consistent with the work of Ellis and Quigg[8] I use the Λ=200MeV Duke and Owens[5,6] parameterizations of the pion and nucleon parton distributions. In order to be consistent with the work of Nason, Dawson and Ellis (ref. 3), as well as Altarelli et al,[9] I set the renormalization scale (μ) at the charm quark mass which I have taken to be 1.5GeV (midway between the extremes of 1.2GeV and 1.8GeV used by Ellis and Quigg[8]). Unless otherwise noted the charm quark mass (m) is always set to this value. The valence and sea quark as well as the gluon parton distribution functions (evaluated at $Q^2=\mu^2=m^2$) for the pion and proton are shown in FIGURE 1.5 (A and B). I assume that the distribution functions are independent of the nuclear environment.

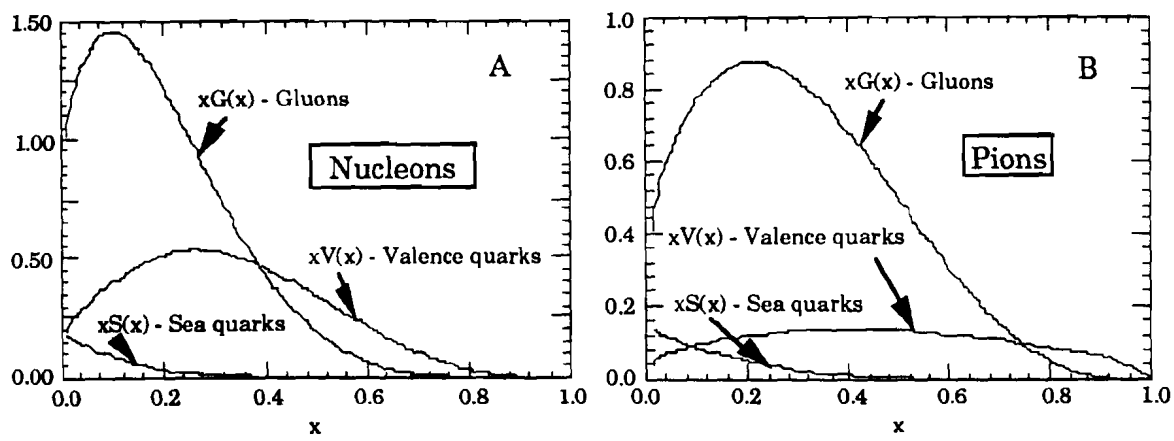

FIGURE 1.5
A) Proton parton distributions B) Pion parton distributions

5 D.W. Duke and J.F. Owens, Physical Review D30, Number 1, p. 49, 1984.
6 J.F. Owens, Physical Review D30, Number 5, p. 943, 1984.
7 J.G. Morfin and Wu-Ki Tung, FERMILAB-Pub-90/74, 1990.
8 R.K. Ellis and C. Quigg, FNAL publication, FN-445, 2013.000 (1987).
9 G. Altarelli et al., Nuclear Physics B308 (1988), p. 724.

No precise measurements exist for the kaon's parton distributions. There is some indication,[10] using data from high-p_T π^o production by a π and K beam at 100GeV and 200GeV, that at high x (>0.5) both the kaon's strange and up valence quark distributions fall more rapidly than for the pion valence quarks. A measurement[11] for x>0.7, using $\mu^+\mu^-$ production in a π and K beam at 150GeV, indicates that the ratio $R=u_K(x)/u_\pi(x)$ can be fit by $(1-x)^{0.18\pm0.07}$ in agreement with a more rapid fall off for the kaon distribution. The form of the valence and sea quark distributions in the kaon are quoted by another group,[12] using 70GeV $K^+p\rightarrow K^nX$ (n = +, -, 0) data from the BEBC experiment, for high-x as $u_K^{val}=(1-x)^1$, $s_K^{val}=(1-x)^{0.3}$ and $S_K^{sea}=(1-x)^{4-5}$. These measurements assume that the parton model at high-Q^2 (momentum transfer) is applicable to the hadrons in low energy interactions. They are only strictly appropriate for soft processes unlike the production of charm.

There are no measurements of the form of the kaon gluon distribution. The NA3 collaboration[13] assumed that the kaon gluon distribution, $G_K(x)$, had the same form as their measured pion gluon distribution ($G_\pi(x)\propto(1-x)^{2.38}$). Then they varied the normalization of the kaon gluon distribution to give the best fit to their J/ψ data. Their best fit indicated that the gluons carry 48.5% of the kaon's momentum with no error quoted on the value.

Several models exist for predicting the valence and sea quark distributions in mesons.[14,15,16] Two of these models[14,15] were compared to the experimental data of Badier et al.[11] Although the model of F. Martin[14] matched the data points better than that of El Hassouni and Napoly (ref. 15) the latter result was used because their functional form of

---

10 Kwan-Wu Lai and Robert L. Thewes, Physical Review Letters, Vol. 44, Number 26, p. 1729, 1984.
11 J. Badier et al., Physics Letters, Vol. 93B, Number 3, p. 354, 1980.
12 L. Gatignon et al., Physics Letters, Vol. 115B, Num. 4, p. 329, 1982.
13 J. Badier et al., Z. Phys. C - Particles and Fields, 28, p. 321 (1985).
14 F. Martin, paper presented at the XVth Recontre de Moriond (Les Arc, 1980), CERN preprint TH 2845.
15 A. El Hassouni and O. Napoly, Physical Review D, Vol. 23, Number 1, 193, 1981.
16 P.V. Chliapnikv et al., Nuclear Physics B148 (1979), p. 400.

the distributions was better matched to this calculation. They give the following parameterizations of the sea and valence quark distributions:

$$u_K^{valence}(x) = 0.82x^{-0.5}(1-x)^{1.33}$$
$$s_K^{valence}(x) = 1.52x^{-0.17}(1-x)^{1.0}$$
$$u(\text{ or } d)_K^{sea}(x) = 0.15x^{-1.0}(1-x)^{5.3}$$
$$s_K^{sea}(x) = 0.089x^{-1.0}(1-x)^{5.7}$$

They make no prediction for the form of the gluon distribution function in kaons. Since the pion and kaon are both mesons containing only light quarks (u, d and s) their gluon distributions should be similar. I chose to use Duke and Owens' (ref. 6) form of the gluon

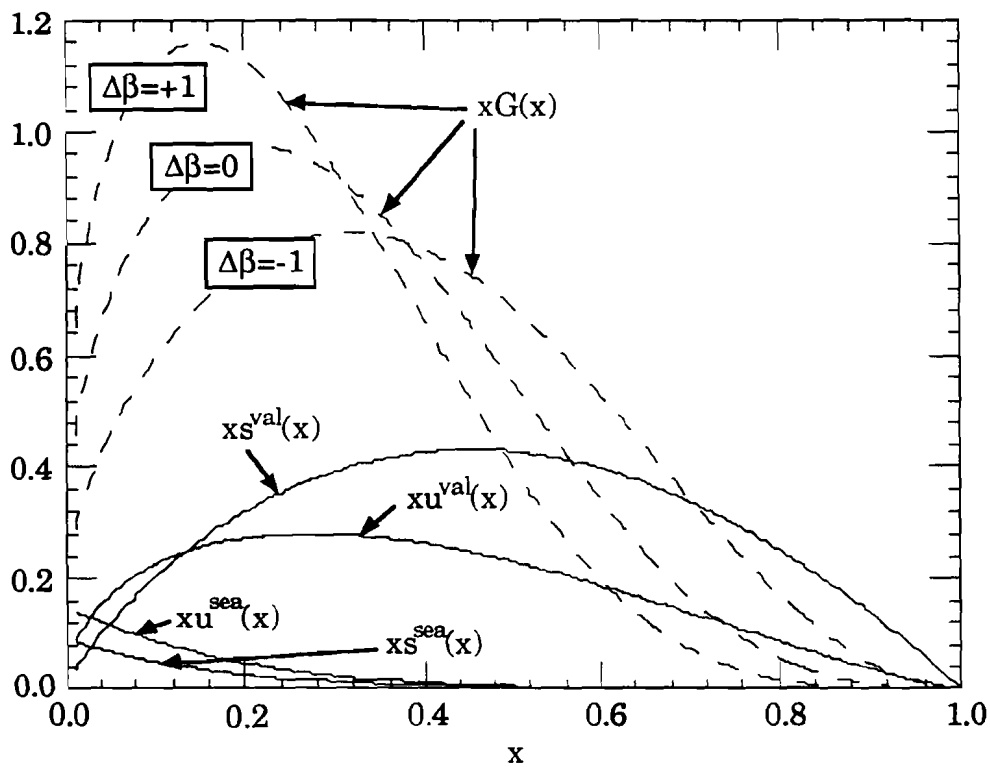

FIGURE 1.6
Kaon quark distribution functions of El Hassouni and O. Napoly
(see text for explanation of gluon distributions)

distribution in pions for the kaon:

$$G_K(x) \equiv G_\pi(x) = Nx^{\alpha-1}(1-x)^\beta(1+\gamma_1 x+\gamma_2 x^2)$$

since I already use their distributions for the pion and proton. The parameters α, β, γ_1, and γ_2 are all parameterized in terms of the energy scale of the interaction. I adjust the normalization of the pion gluon distribution to ensure that the gluons carry the momentum of the kaon not carried by the light quarks:

$$\sum_{\substack{\text{valence q}\\ \text{sea q}}} \langle xq_K(x)\rangle \equiv f$$

$$\text{where} \quad \langle xq_K(x)\rangle = \int_0^1 xq_K(x)dx$$

$$\text{then} \quad \langle xG_K(x)\rangle = \int_0^1 Nx^\alpha(1-x)^\beta(1+\gamma_1 x+\gamma_2 x^2) = 1-f$$

$$\text{thus} \qquad N = \frac{1-f}{B(\alpha+1,\beta+1)+\gamma_1 B(\alpha+2,\beta+1)+\gamma_2 B(\alpha+3,\beta+1)}$$

where f is the fraction of momentum carried by the valence and sea quarks in the kaon leaving a fraction (1-f) for the gluons. This determines the normalization of the kaon's gluon function when B is Euler's Beta function. The kaon distributions as parameterized above are shown in FIGURE 1.6. Also shown in the figure is the effect of changing the exponent β of the (1-x) term in the gluon distribution by ± 1. β is equal to 3.1 for the pion's gluon distribution. This is done in order to study our experiment's sensitivity to changes in the gluon distribution of the kaon.

Total Cross Sections

Substituting the functions given above for the parton distributions and parton-parton cross sections into

$$\sigma(P_1,P_2) = \sum_{i,j}\int dx_1 dx_2 f_i(x_1,\mu) f_j(x_2,\mu)\hat{\sigma}_{ij}(\alpha_s(\mu), x_1P_1, x_2P_2)$$

one can predict the variation of the total charm cross section with the beam energy as shown in FIGURE 1.7. The figure shows both the LO and the LO+NLO results highlighting the

importance of the NLO calculation. The NLO+LO calculation is about a factor of 2.5 higher than the LO only. The figure also shows the difference in the cross section for πp, Kp and pp interactions. At LO there is no difference between the cross sections for the incident pion and proton at our beam energy of 250GeV. At NLO the pp cross section is about 10% higher than the πp cross section although this factor varies sharply with the choice of the charm quark mass and renormalization scale. The total cross sections change by about a factor of 2 for μ in the range of 1GeV to 3GeV and about a factor of 3 as the charm quark mass is changed from 1.2GeV to 1.8GeV. The Kp cross section is everywhere higher than the πp cross section since, in the parton distributions used in this analysis, the gluons in the kaon carry a larger fraction of the kaon's momentum than the gluons in the pion.

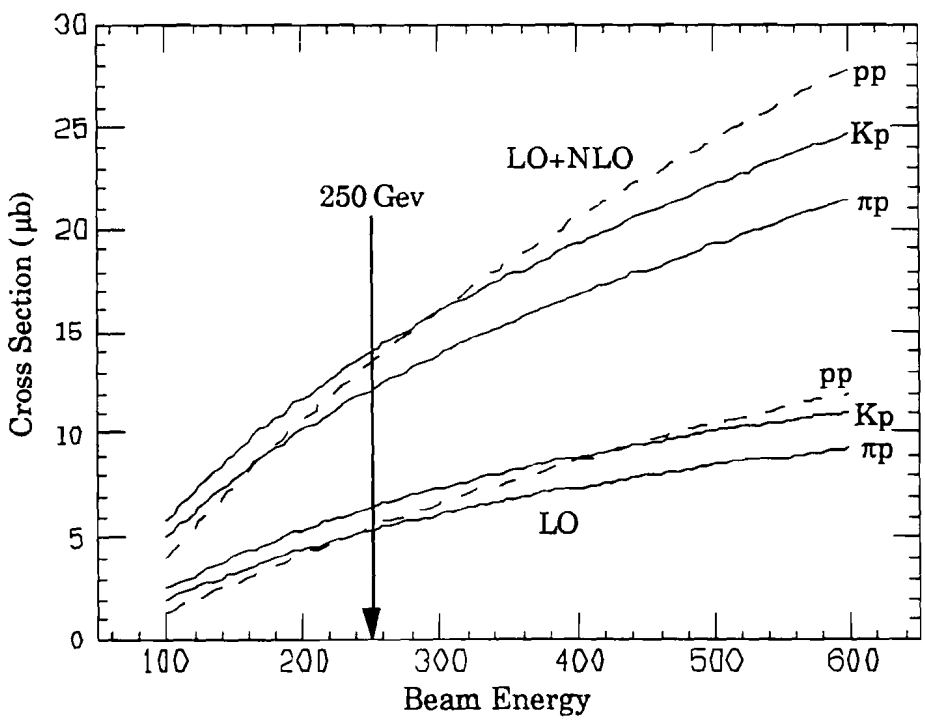

FIGURE 1.7
The variation of the total charm cross section with CM energy for π, K and p beams

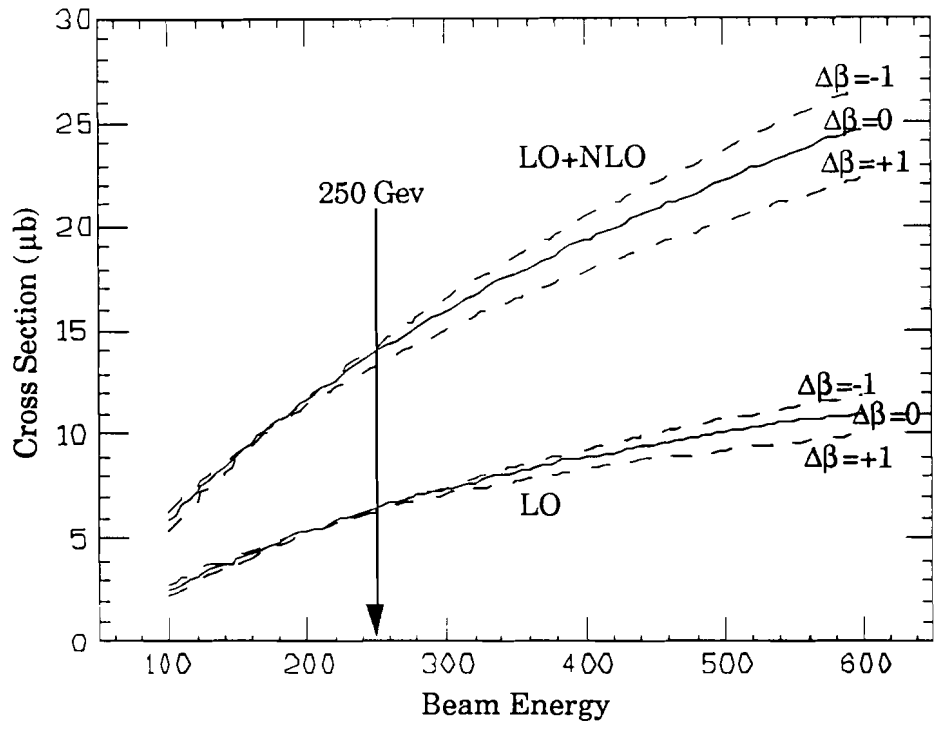

FIGURE 1.8
The variation of the total charm cross section with CM energy for kaons
Also shown are effects due to changes in the form of the kaon's gluon structure function as described in the text.

There is very little difference between the (πKp)p interaction and the (πKp)n interaction: only the interactions of the beam particle with the target protons have been calculated.

FIGURE 1.8 indicates how the Kp cross section changes as the shape of the gluon distribution is adjusted inside the kaon. Specifically, I alter the exponent of the (1-x) term in the gluon structure function (β) by ±1 while maintaining the momentum fraction carried by the gluons. At E769's beam energy the total Kp cross section is not sensitive to changes in the exponent β. The difference in the total cross section between the pion and kaon is an indication of the relative amount of momentum carried by the gluons in the kaon as compared to that carried by the gluons in the pion. TABLE 1.1 summarizes the calculated cross sections at E769's beam energy of 250GeV for the π, K and p beams.

TABLE 1.1
(π/K/p)p charm quark cross sections at 250GeV for all x_F

Beam Particle	NLO+LO Cross Section (μb)
π	12.1
p	13.5
K ($\Delta\beta$=0.0)	14.0
K ($\Delta\beta$=−1.0)	13.3
K ($\Delta\beta$=+1.0)	14.3

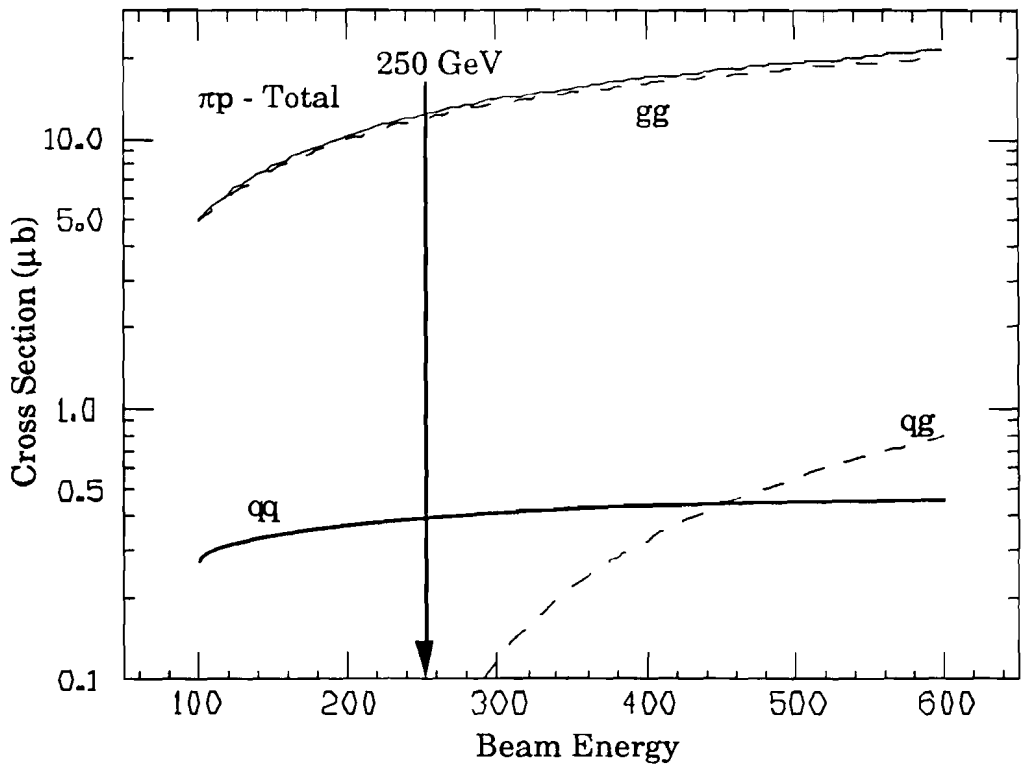

FIGURE 1.9
The various elements of the NLO $\pi p \rightarrow$charm cross section.

FIGURE 1.9 shows that greater than 95% of the NLO charm cross section at a beam energy of 250GeV is due to the gluon-gluon interaction. The NLO quark-glue interaction does not contribute at all.

Differential Cross Sections

The differential x_F and p_T^2 distributions have been calculated to NLO (Nason, Dawson and Ellis, ref. 4) but the shape of the NLO and LO differential distributions are very similar. x_F is Feynman's x variable defined as the fraction of the maximum possible momentum carried by the particle in the direction parallel to the beam in the CM. p_T^2 is the square of the momentum of the particle transverse to the beam direction. When studying the shape of the differential distributions it is only necessary to calculate the LO contribution to the differential cross sections.[17] The form of the theoretical differential distribution is given by:

$$\frac{d\sigma}{dy_3 dy_4 d^2p_T} = \frac{\alpha_s^2(\mu)}{4m_T^2[1+\cosh(\Delta y)]^2} \sum_{ij} x_1 f_i(x_1,\mu) x_2 f_j(x_2,\mu) \overline{\sum_{ij} |M_{ij}|^2}$$

where $m_T=\sqrt{m^2+p_T^2}$ is the transverse mass of the heavy quarks and $\Delta y=y_3-y_4$ is the difference in rapidity between the two outgoing charm quarks. The rapidity is defined as:

$$y = \frac{1}{2}\ln\left(\frac{E+p_z}{E-p_z}\right)$$

where E is the energy of the particle and p_z is its momentum longitudinal to the beam axis. Using energy and momentum conservation we can solve for x_1 and x_2 in terms of the rapidities:

$$x_1 = \frac{m_T}{\sqrt{S}}\left(e^{y_3}+e^{y_4}\right) \qquad x_2 = \frac{m_T}{\sqrt{S}}\left(e^{-y_3}+e^{-y_4}\right)$$

$$s = x_1 x_2 S = 2m_T^2[1+\cosh(\Delta y)]$$

The matrix elements for the qq and gg interactions in LO can also be expressed in terms of the rapidities and the transverse mass as

17 personal correspondence with K. Ellis, FNAL, June 1991 and ref. 4.

$$\overline{\sum \left|M_{q\bar{q}}\right|^2} = \frac{4}{9}\left(\frac{1}{1+\cosh(\Delta y)}\right)\left(\cosh(\Delta y) + \frac{m^2}{m_T^2}\right)$$

$$\overline{\sum \left|M_{gg}\right|^2} = \frac{1}{24}\left(\frac{8\cosh(\Delta y)-1}{1+\cosh(\Delta y)}\right)\left(\cosh(\Delta y) + 2\frac{m^2}{m_T^2} - 2\frac{m^4}{m_T^4}\right)$$

We would like to calculate the differential distributions in p_T^2 and x_F instead of y_3 and y_4. Since $d^2p_T = dp_T^2 d\phi/2$, where ϕ is the azimuthal production angle in polar coordinates, we can easily integrate over ϕ. We can integrate over y_4 and convert from y_3 to x_F in the following manner:

$$\frac{d\sigma}{dy_3 dp_T^2} = \frac{dx_F}{dy_3}\frac{d\sigma}{dx_F dp_T^2}$$

$$= \pi \int dy_4 \frac{\alpha_s^2(\mu)}{4m_T^2\left[1+\cosh(\Delta y)\right]^2} \sum_{ij} x_1 f_i(x_1,\mu) x_2 f_j(x_2,\mu) \overline{\sum_{ij} \left|M_{ij}\right|^2}$$

$$\frac{d\sigma}{dx_F dp_T^2} = \left(\frac{dx_F}{dy_3}\right)^{-1} \pi \int dy_4 \frac{\alpha_s^2(\mu)}{4m_T^2\left[1+\cosh(\Delta y)\right]^2} \sum_{ij} x_1 f_i(x_1,\mu) x_2 f_j(x_2,\mu) \overline{\sum_{ij} \left|M_{ij}\right|^2}$$

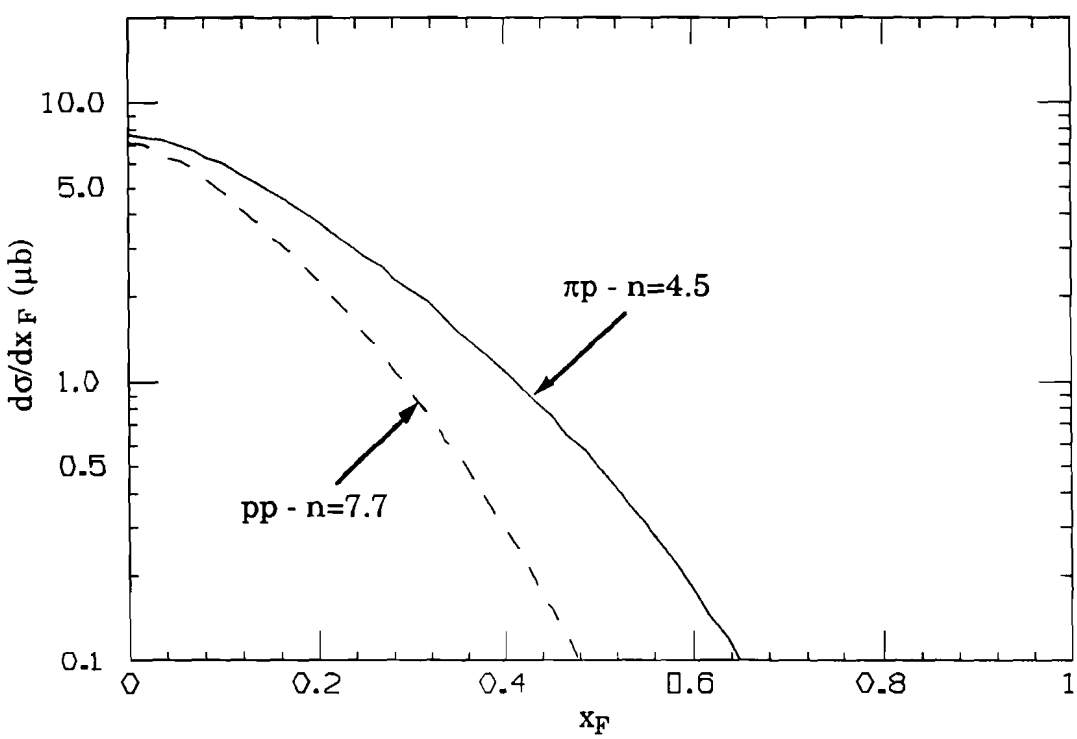

FIGURE 1.10
LO π and p induced charm quark x_F distributions

The differential distribution in x_F (p_T^2) may be obtained by numerically integrating the right hand side of the equation over y_4 and p_T^2 (x_F) with appropriate limits of integration on each variable.

FIGURE 1.10 shows the differential x_F charm quark distributions for pion and proton induced charm as a function of x_F. Since it is common experimentally to fit the x_F distribution to a function of the form $A(1-x_F)^n$, all of these theoretical distributions have been fit in this way for $x_F>0.1$. The values of the exponents n are shown on the figures. The following FIGURE 1.11 shows the same distributions for kaon induced charm. Also shown in the same figure is the change in the distribution as the exponent β in the gluon structure function is changed by ±1. With a sufficiently accurate measurement of n in the

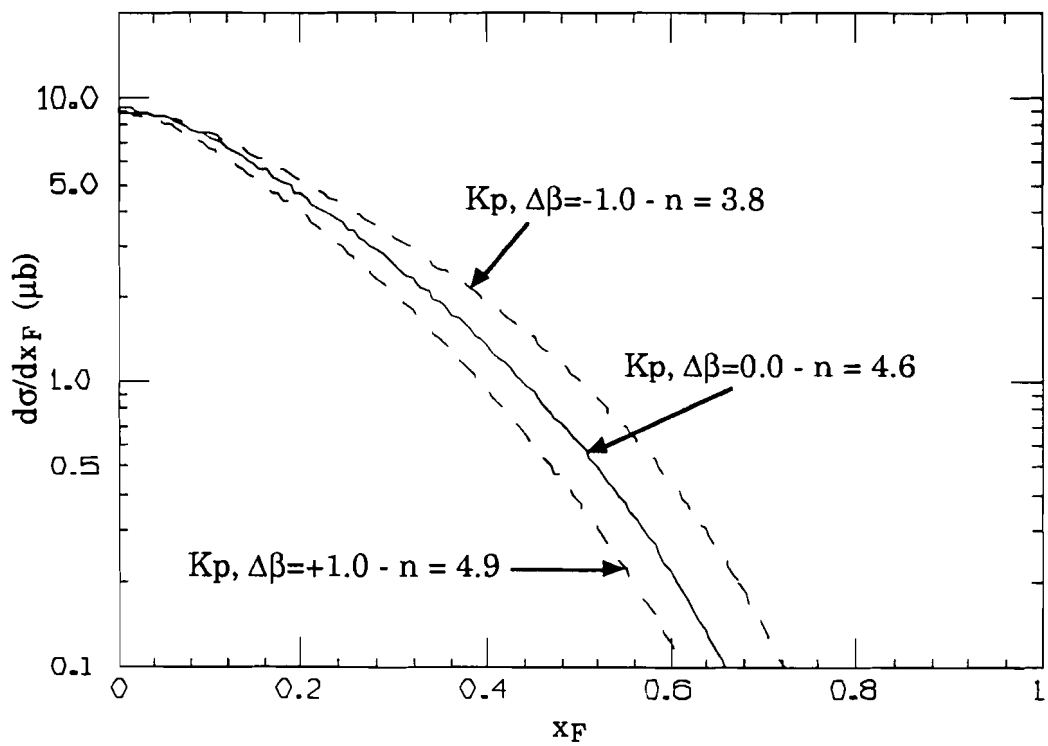

FIGURE 1.11
LO kaon induced charm quark x_F distributions
The variation of the differential cross section with changes to the kaon gluon structure function as described in the text is also shown.

data it would be possible to make a measurement of the exponent β in the kaon. This would require assuming a particular fragmentation model (described in the next section) in order to extrapolate from the charmed meson differential distribution to the bare charm quark distribution.

The p_T^2 distributions for (π/p)p interactions are shown in FIGURE 1.12. The p_T^2 distributions are commonly fit to a function of the form $A\exp(-bp_T^2)$. The theoretical values of b for $p_T^2>1.0$ are shown on the figure.

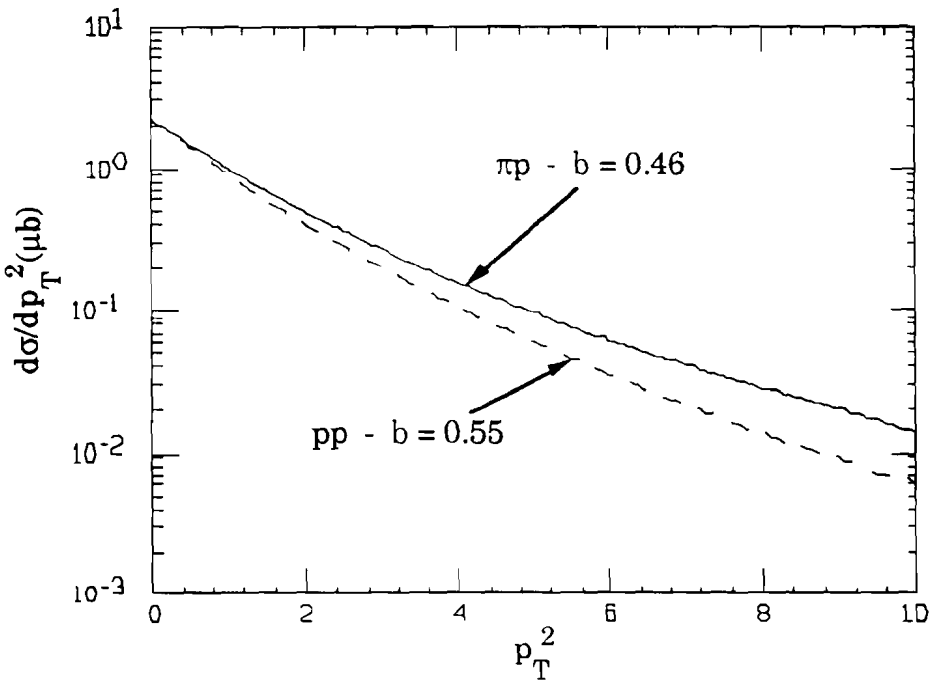

FIGURE 1.12
LO p_T^2 distributions for π and p induced charm quarks

In FIGURE 1.13 it is obvious that the p_T^2 distribution of the charm quarks is not very sensitive to the β exponent in the kaon gluon structure function. The value of b is very close to that of the πp p_T^2 distribution since both the π and K are light mesons and have similar parton distributions. Since the cross sections are dominated by the gluon distributions and $G_K(x)$ has the same form as $G_\pi(x)$ this is as expected.

Since E769 is only sensitive to $x_F>0.0$ it is interesting to study the behaviour of p_T^2 for $x_F>0.0$. A plot of the p_T^2 distribution in this x_F range differs in normalization from FIGURE 1.12 but there is no difference in the fitted parameter b.

The predicted values of b, as well as a summary of all of the results on differential cross sections shown above, are given in TABLE 1.2. I have not estimated the theoretical uncertainties in determining n and b, but a recent communication[18] suggests that the error is of the same order of magnitude (about ±1 unit in n) as the change expected by including fragmentation (discussed below) in the production of charmed hadrons.

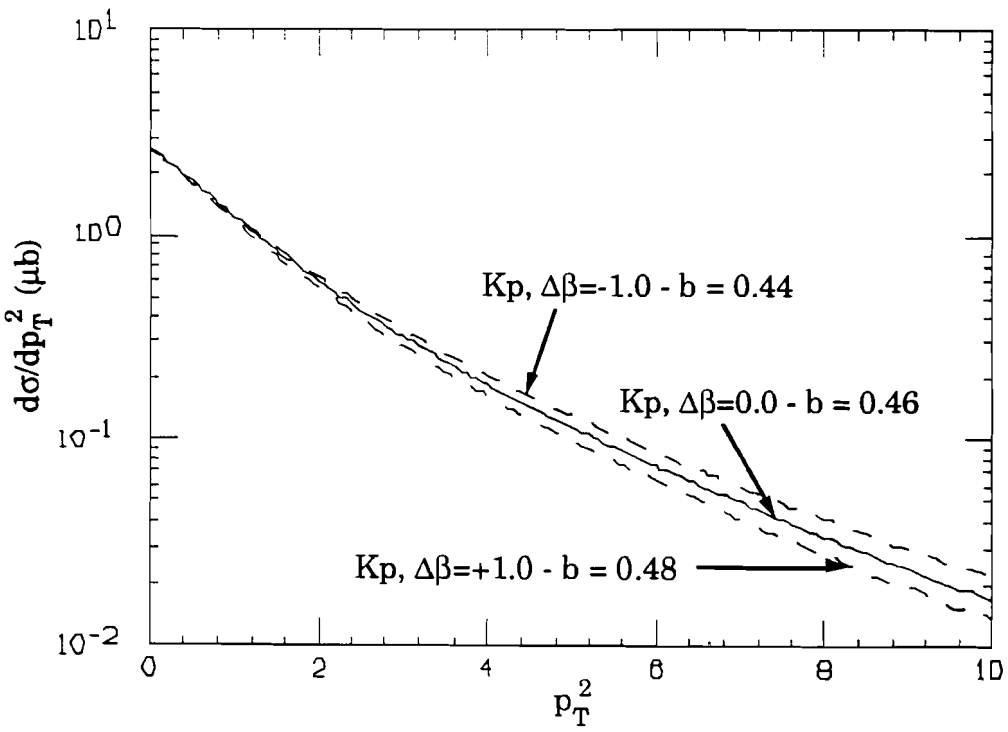

FIGURE 1.13
LO p_T^2 distributions for K induced charm quarks

18 reported by P. Karchin, E769 member, from a discussion with P. Nason at the Third Topical Seminar on Heavy Flavours, San Miniato, Italy, June, 1991.

TABLE 1.2
Summary of fits to LO differential charm quark distributions

Beam Particle	$n(x_F)$ $x_F>0.1$	$b(p_T^2)$ $p_T^2>1.0$	$b(p_T^2)$ $p_T^2>1.0$ $x_F>0$
Pion	4.5	0.46	0.46
Proton	7.7	0.55	
Kaon ($\Delta\beta$=0.0)	4.6	0.46	
Kaon ($\Delta\beta$=-1.0)	3.8	0.44	
Kaon ($\Delta\beta$=+1.0)	4.9	0.48	

Hadronization

Although the production of heavy quarks is understood in the framework of perturbative QCD ($\alpha_S<<1$), their hadronization (or fragmentation) into observable colourless hadrons seems to be determined by the colour-confining processes ($\alpha_S>1$).[19] The study of the hadronization process is therefore of great interest in understanding non-perturbative aspects of QCD. It is of concern to experimentalists since the fragmentation confuses the information in the parton-parton sub-process and must be accounted for when comparing experimental results to theoretical distributions for partons.

The fragmentation process is often handled by Monte Carlo algorithms based on one of three fragmentation models: Independent Fragmentation (IF), Cluster Fragmentation (CF) and String Fragmentation (SF).[20] All of these models rely on an iterative approach to hadron production. An outgoing heavy quark with a specific momentum and energy gradually loses energy through pair-production of light quark/anti-quark pairs. The splitting process continues until there is not enough energy to produce light quark pairs

19 D. Bortoletto et al., Physical Review D, Vol. 37, Number 7, p. 1719, 1988.
20 T. Sjostrand, International Journal of Modern Physics A., Vol. 3, No. 4 (1988) p. 751.

from the sea. The heavy quark becomes confined with one of the lighter quarks to become a hadron.

In IF the outgoing pair of heavy quarks fragment independently of one another regardless of colour, momentum and energy conservation. Once the splitting process is complete the colour, momentum and energy of the final state is adjusted to ensure conservation of these quantities. In CF and SF the hadronization process is envisioned as proceeding through the stretching and subsequent breaking of a colour string between the outgoing heavy quarks. At the break point of the strings, quark or di-quark pairs are produced. SF requires that adjacent quark pairs or triplets combine to form colourless hadrons. CF proceeds until the energy of the string is too small for pair production and only then are the quarks combined into hadron resonances. The most common hadronization method is the SF and it has enjoyed considerable success as implemented by the Lund Group[21].

The light hadrons (not containing heavy quarks) produced in an interaction are formed from the splitting of many strings. Their differential cross sections are correspondingly difficult to calculate. On the other hand, since the production of a heavy quark pair from the sea is suppressed by the large energy required, hadrons containing heavy quarks most likely contain the original primary quark. The differential cross sections for these hadrons are then related to the differential distributions of the primary quarks by the fragmentation functions.

The fragmentation functions $D_q^h(z)$ are defined as the probability that an outgoing quark (q) will produce a hadron (h) with a fraction (z) of the initial quark's momentum. Two quantities which are commonly used for parameterizing the fragmentation functions are the variables x and x_+ defined as:

21 FNAL Publication PM0050 or CERN Long Program Writeups W5035 and W5046.

$$x = \frac{p}{p_{max}} \qquad \text{and} \qquad x_+ = \frac{E + p_z}{E_{max} + p_{max}}$$

where p and E are the momentum and energy of the particle in the CM respectively while p_{max} and E_{max} are the maximum values of p and E respectively. p_z is the component of the momentum in the CM parallel to the original particle.

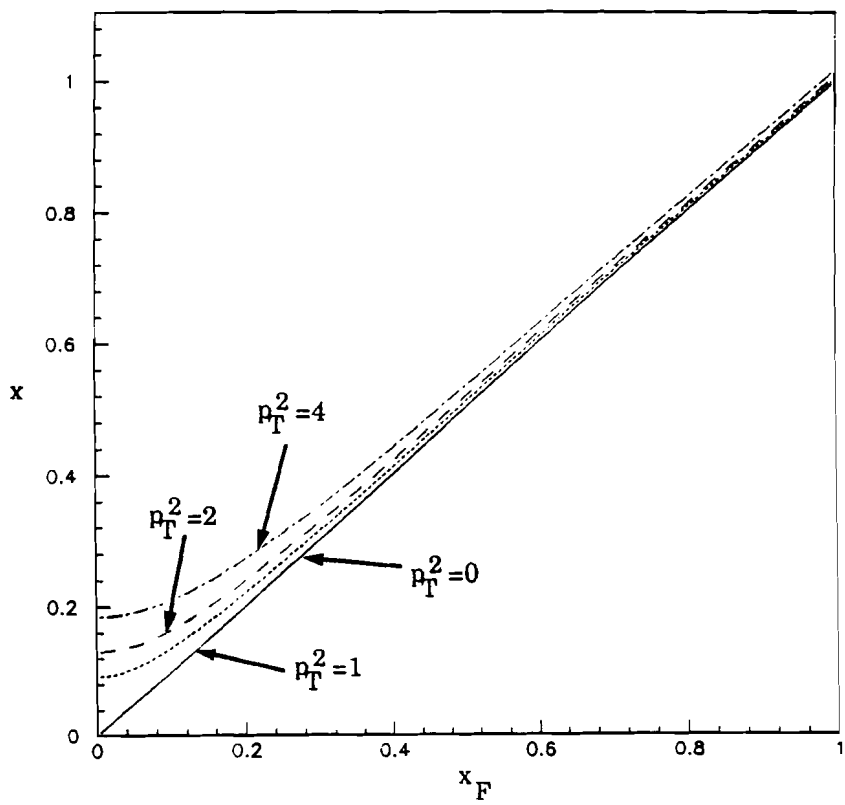

FIGURE 1.14
The relationship between x and x_F for various values of p_T^2

In the limit where $p_T^2 \rightarrow 0$ it can be shown that $x \rightarrow x_F$. FIGURE 1.14 shows the relationship between x and x_F for various values of p_T^2. Since the average p_T^2 of the produced charm quarks and hadrons is about 1 it can be seen that over a wide range of x_F we can use $x_F \sim x$. In the same limit it can also be shown that $x_+ \rightarrow x_F$.

Analytical formulae for the fragmentation functions based on the SF model have been developed by Andersson et al. and Bowler (Bortoletto et al., ref. 19). The Andersson et al.

formula is also known as the Lund Symmetric Fragmentation function as implemented in the LUND MC (see Chapter 5) They are parameterized in terms of the variable x_+:

$$D_q^h(x_+) = N\frac{(1-x_+)^\beta}{x_+}\exp\left(\frac{-B(m_h)_T^2}{x_+}\right) \qquad \text{Andersson et al.}$$

$$D_q^h(x_+) = N\frac{(1-x_+)^\beta}{x_+}\exp\left\{-Bm_q^2\left[\frac{m_h^2}{m_q^2 x_+} - 1 - \ln\left(\frac{m_h^2}{m_q^2 x_+}\right)\right]\right\} \qquad \text{Modified Bowler}$$

and are shown with arbitrary normalization in FIGURE 1.15A where I have converted from x_+ to x_F at $p_T^2=1$. m_h and m_q are the mass of the hadron and quark respectively while $(m_h)_T$ is the transverse mass of the hadron as defined above. B and β are fitted parameters and are equal to $0.52\pm0.05\pm0.03$ GeV^{-2} and $0.60\pm0.10\pm0.04$ respectively.

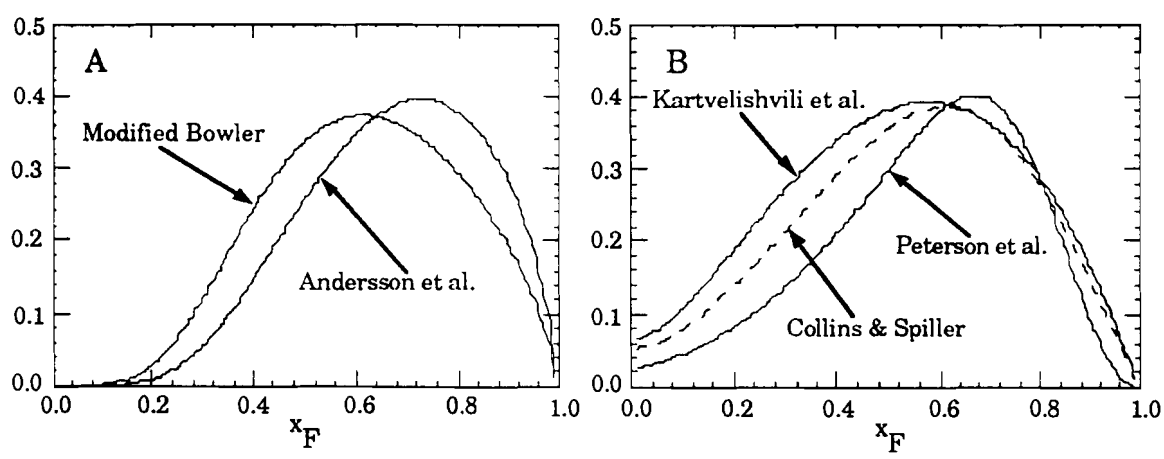

FIGURE 1.15
5 different Fragmentation Functions used in this analysis
A) The fragmentation functions of Andersson et al. and Bowler
B) The fragmentation functions of Kartvelishvili et al, Peterson et al. and Collins & Spiller
(all functions evaluated at $p_T^2=1$)

Three other parameterizations of the fragmentation function are (Bortoletto et al., ref. 19):

$$D_q^h(x) = Nx^{\alpha_Q}(1-x) \qquad \text{Kartvelishvili et al.}$$

where $\alpha_Q = 1.40 \pm 0.18$

$$D_q^h(x) = N\left\{x\left[1-\frac{1}{x}-\frac{\varepsilon_Q}{1-x}\right]^2\right\}^{-1} \qquad \text{Peterson et al.}$$

where $\varepsilon_Q = 0.156 \pm 0.015$

$$D_q^h(x) = N\left[\frac{1-x}{x}+\frac{2-x}{1-x}\varepsilon_Q\right]\left(1+x^2\right)\left[1-\frac{1}{x}-\frac{\varepsilon_Q}{1-x}\right]^{-2} \qquad \text{Collins \& Spiller}$$

where $\varepsilon_Q = 0.64 \pm 0.14$

They are shown in FIGURE 1.15B where I have also converted from x to x_F at $p_T^2=1$. All of these fragmentation functions use parameters selected to agree with data from e^+e^- interactions producing heavy quarks. If we assume that the quarks fragment independent of the environment in which they are produced, we may calculate the x_F distribution of the D_s mesons by convoluting the fragmentation functions with the calculated charm quark differential cross sections.

The number of quarks produced in the momentum range (p´,p´+dp´) is proportional to dσ(p´). The probability that the quark with momentum p´ fragments into a hadron in the momentum range (p,p+dp)<p´ is given by:

$$D_h\left(\frac{p}{p'}\right)d\left(\frac{p}{p'}\right) = D_h\left(\frac{p}{p'}\right)\frac{dp}{p'}$$

Therefore, the number of hadrons in (p,p+dp) due to quarks in (p´,p´+dp´) is:

$$\begin{aligned} d\sigma(p) &\propto d\sigma'(p')D_h\left(\frac{p}{p'}\right)\frac{dp}{p'} \\ &= \frac{d\sigma'(p')}{dp'}\frac{dp'}{p'}D_h\left(\frac{p}{p'}\right)dp \end{aligned}$$

where σ is the cross section for charmed hadrons and σ' is the cross section for charm quarks. Since quarks in the range $(p',p'+dp')$ may fragment into hadrons with any momentum less than p' the cross section for hadrons in $(p,p+dp)$ due to quarks with $p'>p$ is

$$\frac{d\sigma(p)}{dp} = \int_{p}^{p'_{max}} \frac{d\sigma'(p')}{dp'} \frac{dp'}{p'} D_h\left(\frac{p}{p'}\right)$$

where p'_{max} is the maximum momentum of the charmed quark. Since all of the momentum of the charmed quark may go into the momentum of the hadron $p_{max}=p'_{max}$. Defining $x'=p/p'$ and $x=p/p_{max}$ it is then possible to show that

$$\frac{d\sigma(x)}{dx} = \frac{1}{x}\int_{x}^{1} x' \frac{d\sigma'(x')}{dx'} D_h(x')dx'$$

In a similar way one can calculate $d\sigma/dx_+$ and find that it is the same as the expression

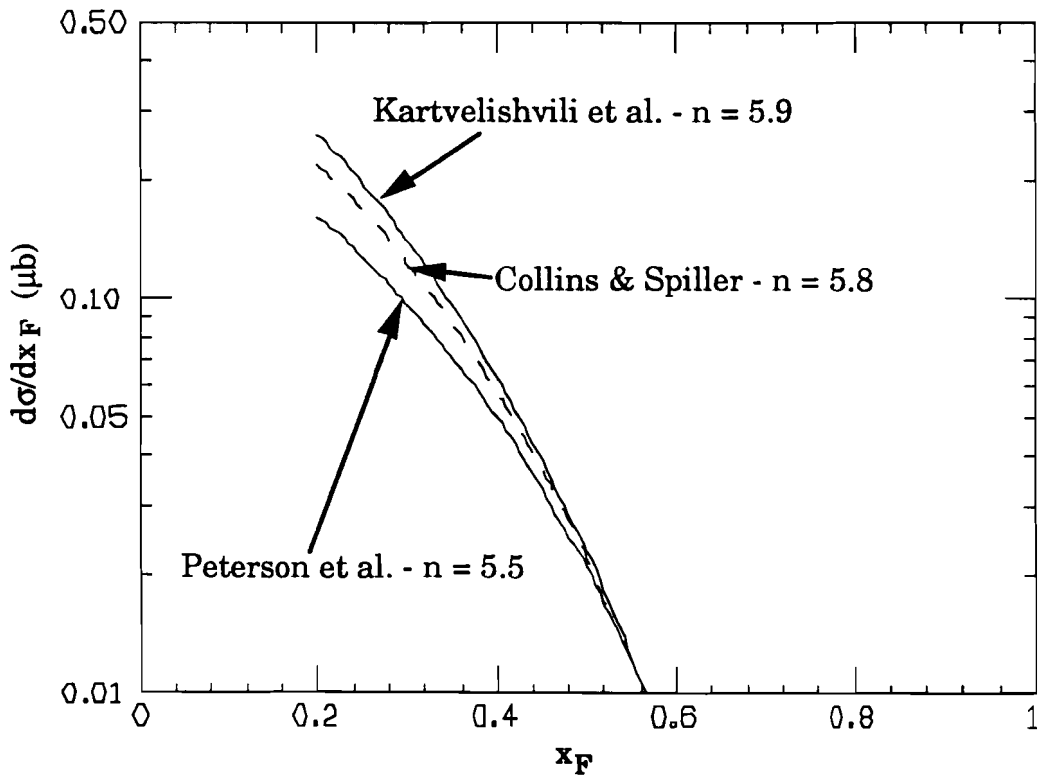

FIGURE 1.16

The differential x_F distribution after fragmentation with the functions of Kartvelishvili et al., Peterson et al., and Collins and Spiller for π induced D_s

given above with $x \rightarrow x_+$. Converting from x or x_+ to x_F is not difficult and allows a prediction of the x_F distribution of the charmed mesons given the x_F distribution of the charm quarks. The results of such a calculation are shown in FIGURE 1.16 for the three fragmentation functions which depend on x. The distributions were only calculated for $x_F>0.2$ since it is only in this range that $x \sim x_F$, and were fit to functions of the form $(1-x_F)^n$. The fitted values of n for each of the three functions is shown on the figure. The x_F distribution is softer for the D_s mesons than for the charm quarks by about one unit in n.

The results of convoluting the differential charm quark cross sections with each of the fragmentation functions are shown in TABLE 1.3. The values in TABLE 1.3 should be compared with those in TABLE 1.2 listing the fitted n for the charm quark before fragmentation. The values of n given there are 4.5, 4.6 and 7.7 for π, K and p beams respectively. The proton results are softer in x_F than the kaon or pion because the charm quarks from which the D_s derive were originally softer. For all three particles the average value of n over all 5 fragmentation functions is approximately one unit higher than for the bare charm quark.

TABLE 1.3
n for D_s differential x_F distributions after fragmentation

Fragmentation Function	$\pi \rightarrow c \rightarrow D_s$ (n)	$K \rightarrow c \rightarrow D_s$ (n)	$p \rightarrow c \rightarrow D_s$ (n)
Andersson et al.	5.1	5.4	8.1
Modified Bowler	5.6	5.9	8.7
Kartvelishvili et al.	5.9	6.3	9.1
Peterson et al.	5.5	5.8	8.6
Collins & Spiller	5.8	6.1	9.0

In order to determine if a flavour dependence exists in the production cross section for D_s mesons we may examine the total or differential cross sections for the D_s for each of a variety of incident beam particles. Disentangling the causes of the flavour dependence is

a more complicated problem requiring knowledge of the structure functions for each of the incident particles and especially of the hadronization process. Measuring the cross sections and determining if there are any observable differences is the first step in this process. This is the goal of this thesis.

Chapter 2: Accelerators and Beamlines

Production of the FNAL 800 GeV protons

The FNAL protons pass through five stages of acceleration before arriving at the proton-east (PE) beamline target used in E769. This section describes the production of the 800 GeV proton beam[22].

The protons derive from a hydrogen ion source located before the Cockcroft-Walton Accelerator (see FIGURE 2.1). An e^- is added to neutral H atoms by passing them over a Cesium source and then the H^- ion is accelerated. Although the intensity of H^- is less than the intensity of p^+ after the Cesium source, the use of H^- ions allows increased stacking of beam in the booster accelerator (described below) and therefore a net increase in proton intensity in the final stages of acceleration.

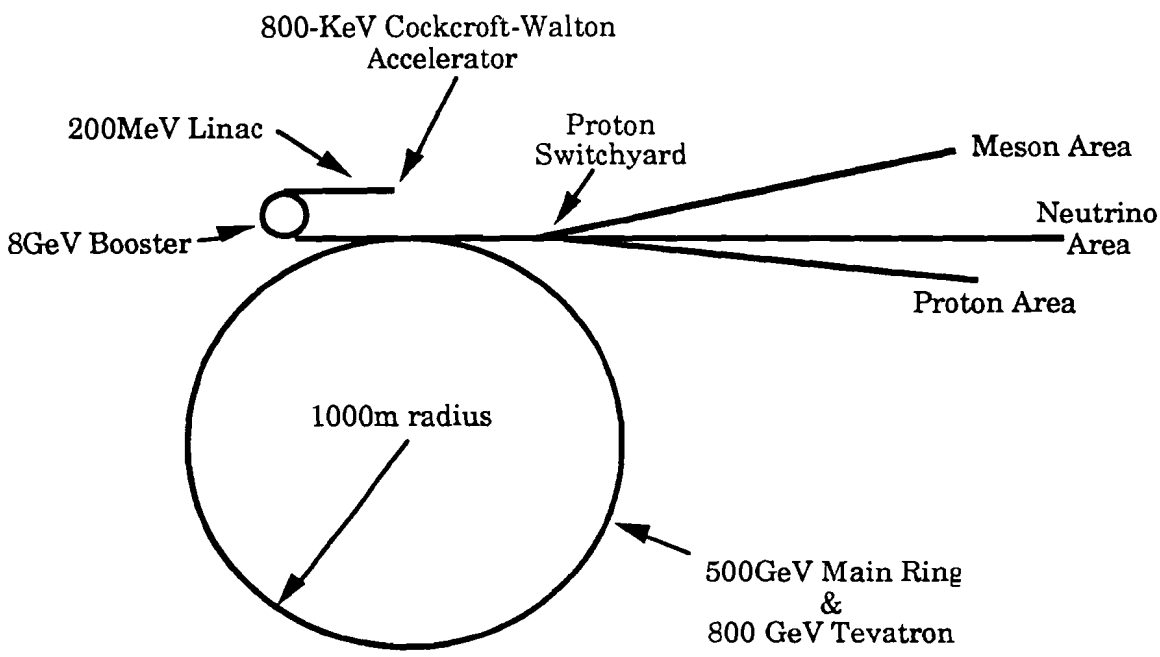

FIGURE 2.1
Schematic Layout of the Fermilab acceleration and beam-line system

22 John Crawford, FNAL Accelerator Division, personal correspondence.

The first stage of acceleration is the Cockcroft-Walton accelerator which injects a 750KeV, 50-60mA H^- beam into the LINAC. The LINAC is a linear accelerator which accelerates the H^- to 200MeV. At the same time, the RF frequency (about 52 MHz) in the LINAC 'bunches' the particles into 'buckets' of H^- separated by about 19ns. The H^- are stripped of both electrons at the entrance to the 8 GeV booster by passing them through a thin carbon foil (about 200μg/cm^2). The beam intensity at this point is about 35-40mA. The booster ring injects protons into the 1km radius FNAL main ring where the protons are accelerated up to 150 GeV. The main ring injects the accelerated protons into the Tevatron which raises the beam energy to its final value of 800 GeV with an intensity of about 1×10^{13} protons/pulse.

The last three stages of acceleration are proton synchrotrons. The first two rings (the Booster and Main Ring) use conventional iron core magnets for bending the particle's trajectory as they are accelerated in the synchronized rf cavities. The Tevatron uses superconducting magnets to bend the paths of the particles.

Once the protons reach their peak energy the beam is slowly extracted over a 22 second 'spill' and sent to the proton 'switchyard'. The switchyard splits the beam into three separate beams which are then sent to three experimental areas: Meson, Neutrino and Proton. The Tagged Photon Laboratory is in the Proton area where the beams are split again into four separate beamlines: Proton-West (PW), Proton-Central (PC), Proton-East (PE) and Proton-B-East (PBE).

The P-East beamline

The PE beam line received a typical flux of about 1.2×10^{12} protons/spill. The PE beam line is shown schematically in FIGURE 2.2.

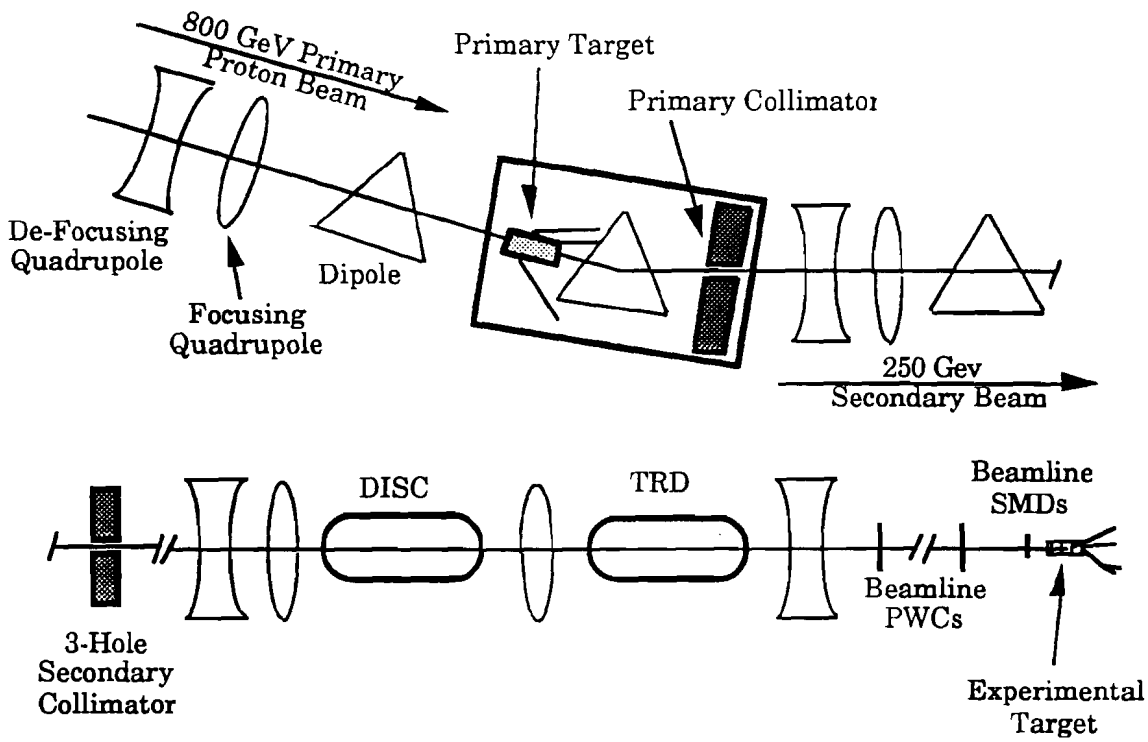

FIGURE 2.2
Schematic of the PE beamline

The 800GeV protons from the Tevatron interacted in a 30cm thick beryllium target. The particles produced in this target were momentum selected and collimated to provide a secondary beam energy of close to 250GeV with an energy spread of only ±0.2%. The predicted beam composition was in the ratio π:K:p ≈1:0.085:0.025 in the negative beam and about 1:0.11:0.57 in the positive beam.[23] The beam then passed through another collimator with three interchangeable holes for final collimation. The hole selection could be adjusted by the E769 experimenters at the experiment's control console.

The second collimator's hole and the next two quadrupole magnets produced the required parallel beam section through the DISC (Differential Isochronous Self-Collimating Cerenkov counter). The expected[24] beam size and divergence of the beam for

23 Jeff Spalding, E769 member and Head of the Research Facilities Dept. of the Research Division at FNAL, personal correspondence.

24 as reported by the TURTLE ray tracing program for the PE5 beamline as run by Anthony Malesek, beamline physicist, FNAL, personal correspondence.

each of the three collimator holes are shown in TABLE 2.1. For the smallest hole setting of the PE4 collimator the divergence of the beam at the DISC was dominated by an approximate 10μrad jitter due to the upstream quadrupole magnetic field 'ripple' and also an ~4μrad divergence due to multiple scattering in the mylar windows on the upstream side of the DISC.

TABLE 2.1
Secondary collimator hole sizes and beam parameters at the DISC

PE4 Collimator Hole size (x cm × y cm)	Beam Size† (x cm × y cm)	Beam divergence‡ (μrads)	Beam Energy Spread (%)
0.0625 × 0.1250	0.84 × 1.02	15	0.001
0.1250 × 0.2500	0.84 × 1.42	22	0.002
0.2500 × 0.5000	0.84 × 1.57	38	0.004

† The 1 sigma width assuming a gaussian beam profile.
‡ assumed to be identical in x and y. Value is 1 sigma in the divergence assuming a gaussian divergence of the beam. Includes a 10μrad jitter due to the upstream quadrupole magnetic field ripple and a 4μrad divergence due to multiple scattering in the mylar windows on the DISC added in quadrature with the intrinsic beam divergence.

The experiment usually used the second collimator hole. The collimator was opened to the largest hole for studies requiring high beam intensity but no particle ID and decreased to the smallest hole when searching for the Kaon 'shoulder' with the DISC.

The experiment's TRD (Transition Radiation Detector) was located between the last two quadrupole magnets which focused the beam at the E769 target. Two last dipoles steered the beam onto the Tagged Photon Laboratory target.

Chapter 3: The E769 Detector

E769 used a large acceptance multi-particle spectrometer located at the Tagged Photon Laboratory (TPL) at Fermilab. The detector has had a long history of involvement in charmed meson and baryon physics including E516, which used the recoil proton in elastic collisions as the charm tag[25], and E691, a very successful charm photo-production experiment.[26]

The spectrometer included a silicon microstrip vertex detector, 35 Drift Chamber planes, two Proportional Wire Chambers, two large magnets for tracking and momentum determination, two Cerenkov counters, muon and kaon scintillator walls, and electromagnetic and hadronic calorimetry. FIGURE 3.1 shows a scale view of the

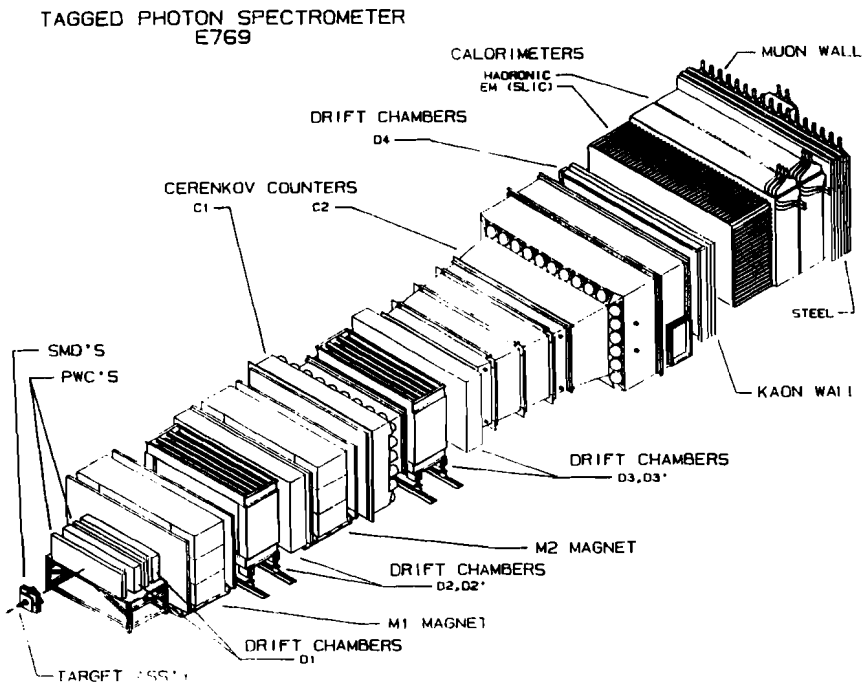

FIGURE 3.1
Scale View of the E769 Spectrometer

25 K. Sliwa et al., Phys. Rev. D, Particles & Fields, Third Series, Vol. 32, No. 5, 1 September 1985, p. 1053.

26 J. R. Raab et al., Phys. Rev. D, Vol. 37, #9, p. 2391.

spectrometer. FIGURE 3.2 is a schematic view of the detector indicating the arrangement of all major components.

The following sections of this chapter describe each of the components in detail. The reference system used throughout the text and the experiment has the +z-axis oriented along the direction of the beam. The x-axis is the horizontal direction and the positive y-axis points straight upwards.

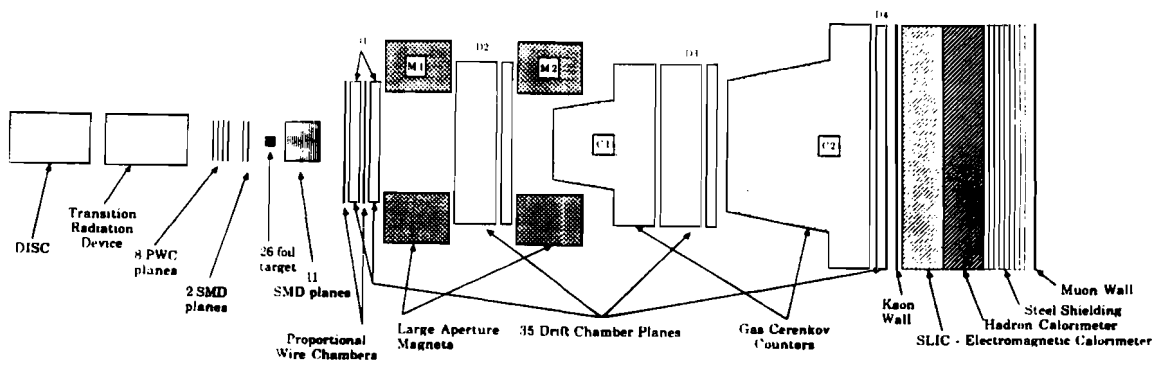

FIGURE 3.2
Schematic View of the E769 Spectrometer

The Differential Isochronous Self-Collimating Cerenkov Counter (DISC)

Theory

The DISC counter exploited the difference in the Cerenkov angle (θ_c) between the three beam particle types at 250 GeV to tag kaons in the beamline. The Cerenkov angle is related to the velocity of the particle (β) and index of refraction of the medium (n) by:

$$\cos\theta_c = \frac{1}{\beta n(\lambda)}$$

where

$$\beta = \left(1 + \frac{m^2}{p^2}\right)^{-\frac{1}{2}}$$

and the index of refraction of the medium depends on the wavelength of light.

At constant β the Cerenkov angle can be altered by changing the index of refraction of the medium. The index of refraction of the gas can be changed by altering its pressure (P). These two parameters are related by:

$$(n - 1) = (n_0 - 1)\frac{P(\propto T)}{P_0}$$

where n_0 is the index of refraction at the reference pressure P_0 normally taken as 1 atm. The equation indicates the linear relationship between the temperature (T) and pressure (P) of the gas medium as expressed by the ideal gas law.

DISC Physical Characteristics and Electronics

The DISC was designed and built at CERN in 1971 for use in the 2.5 mrad beamline of the focusing spectrometer facility for FNAL E96. A schematic diagram of the DISC's construction and gas lines as implemented for E769 is shown below. A sensitive gas pressure meter and electronic thermometer were used to determine relative changes in the refractive index of the DISC gas. The DISC was filled with He gas (n=1.00035 at STP) to a pressure of about 8.5atm. A relief valve set at about 8.8 atm ensured that the pressure could not exceed safety limits. The 'windows' on either side of the DISC through which the beam particles travelled were made of 8 sheets of .25mm thick Mylar.

The He filling process could be performed manually or through a computer controlled solenoid valve. We used one of two flow meters to control the rate of filling. A fast flow meter (5 to 25 l/m) was used when filling and purging the DISC of air and also to change the pressure to a value suitable for beginning a pressure curve. A slow flow meter (0 to 5 l/m) was used for fine tuning the DISC pressure to the best kaon signal and also during a pressure curve to provide incremental steps in the DISC pressure between successive good spills. An identical gas system could be used when exhausting the He from the DISC.

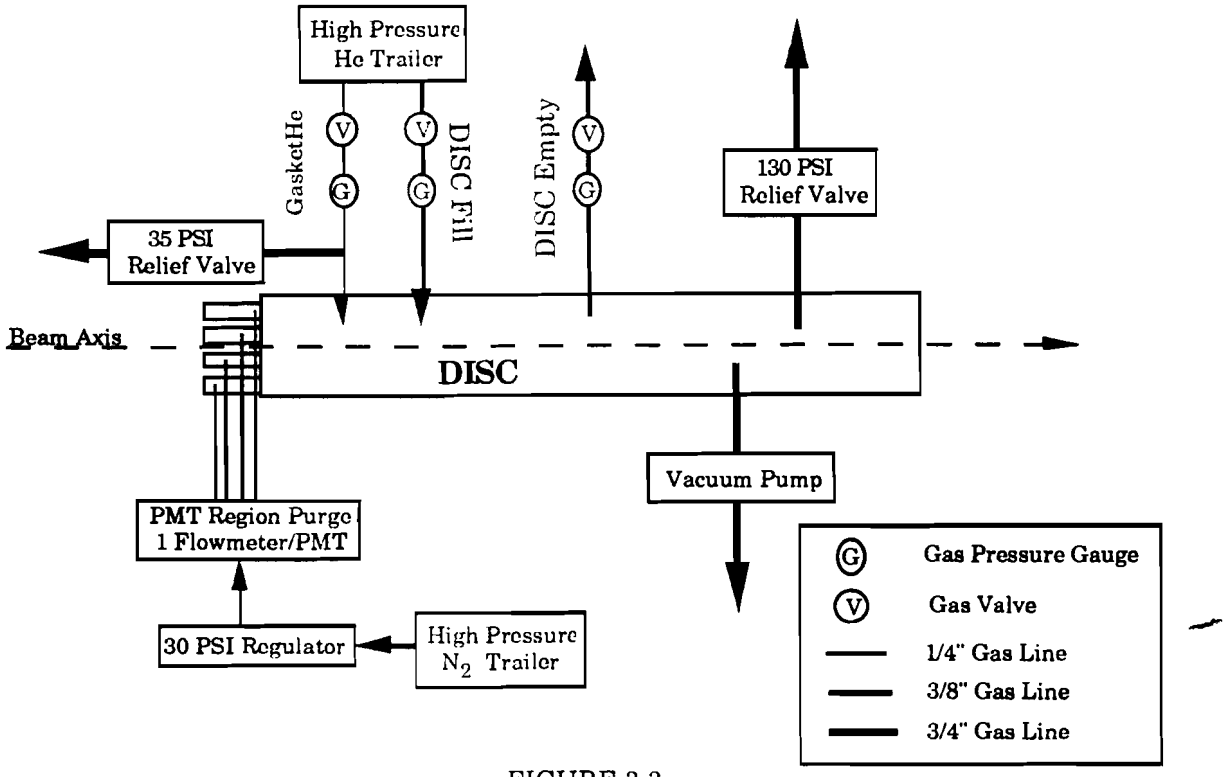

FIGURE 3.3
DISC Pressure Vessel and Gasline Schematic

We used a Texas Instruments PPG149 Pressure Meter and OMEGA 199P2 temperature monitor to provide a relative measure of the index of refraction of the Helium. The Pressure Meter was located in the counting room roughly 100m from the DISC. It had a digital readout with a resolution of 1 count in 150,000 or about 7×10^{-5}atm. The PPG149 had a rated accuracy of 0.01% and reproducibility of 1 or 2 counts. The digital output was available in binary format for electronic readout by a Fermilab built 007 24-bit input module. The pressure was recorded on tape once per spill in the scaler events (see Chapter 3: The Data Aquisition System: E769 Data Format).

The temperature monitor had a rated resolution of 0.1° and uniformity of 0.1°. It was also located in the counting room. The BCD output of this meter was read through another Fermilab 007 24-bit input module and was written to tape once per spill in the scaler events. The resistance of the long cable connecting the sensor to the readout unit caused a shift in the displayed temperature of about 10°.

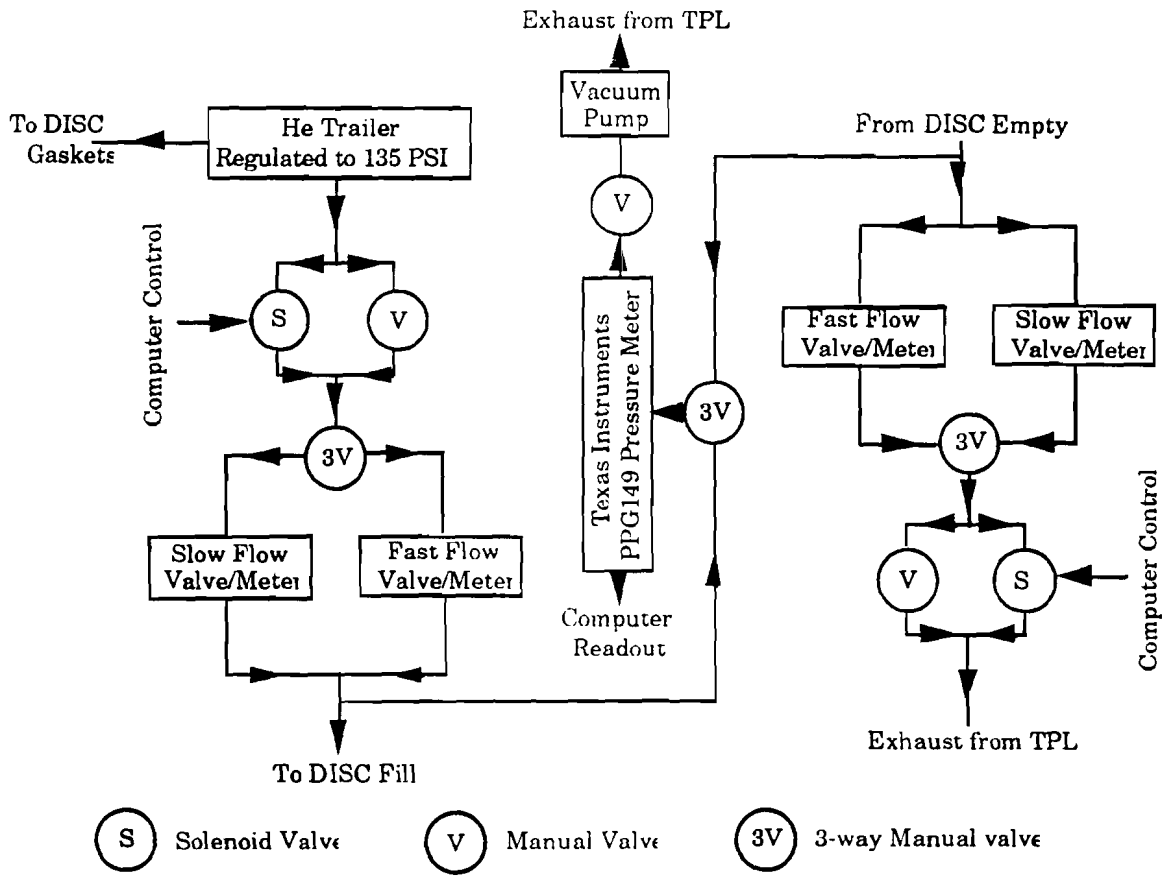

FIGURE 3.4
DISC Counting Room Gas Distribution Schematic

Each DISC phototube was enclosed in its own steel container and separated from the main DISC vessel by a quartz window. The volume surrounding each PMT was continuously flushed with N_2 to avoid possible He contamination of the phototubes.

The DISC utilized Hamamatsu R1332Q phototubes. Fifteen of these tubes were tested for uniformity in gain and resolution. Eight tubes with similar characteristics were chosen for the DISC as well as two backup tubes. The tubes were run at an average of about 1950V. The readout, testing and trigger electronics are shown in the following FIGURE 3.5.

The phototubes could be tested *in situ* using an LED placed near the PMT windows. The height and width of the voltage pulse to the LED was adjusted to provide about one photoelectron per pulse. Each PMT signal was amplified and sent into two different cables

using a Lecroy 621A amplifier. One of the signals was brought to the counting room on a RG-8 hard line (propagation speed at 1 MHZ = 0.84c[27]) for use in the trigger decision. The signal was sent through a Lecroy 4416 discriminator and then a Lecroy 4508 Programmable Logic Unit (PLU) provided eight output bits to the trigger corresponding to the PMT conditions shown in the following TABLE 3.1.

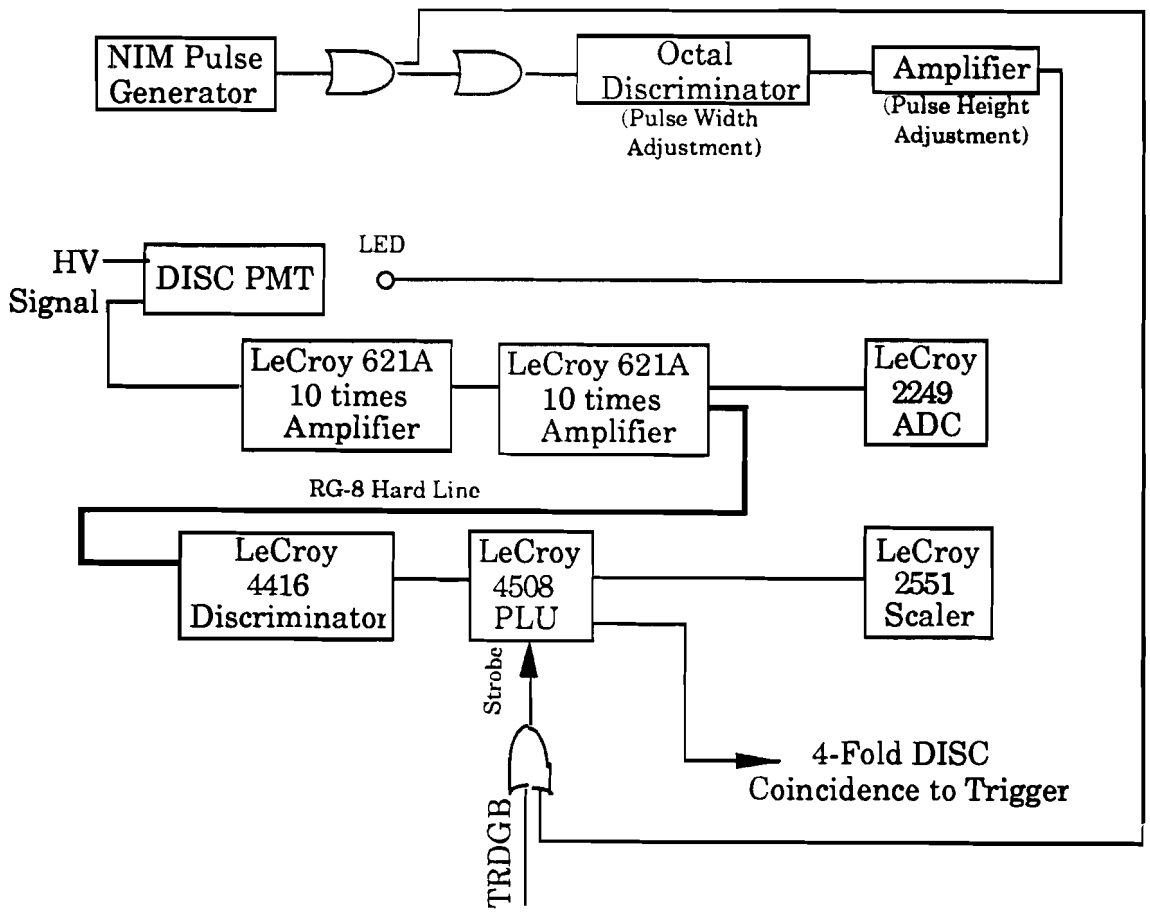

FIGURE 3.5
DISC Electronics

27 Belden Catalog, COOPER Industries, RG-8, Trade #9913, U.L. Type #80C.

TABLE 3.1
DISC PMT logical conditions

4508 PLU Output Bit	PMT coincidence condition
1	PMT1 + PMT2
2	PMT3 + PMT4
3	PMT5 + PMT6
4	PMT7 + PMT8
5	4-fold coincidence with 1 hit/quadrant
6	5-fold coincidence with 1 hit/quadrant
7	6-fold coincidence with 1 hit/quadrant
8	7-fold coincidence

The 4-fold coincidence condition with at least one hit per quadrant (a quadrant was a set of two adjacent tubes as defined for bits 1 through 4 in TABLE 3.1) was used to tag events with beam particle identification by the DISC. All DISC tagged events which passed the transverse energy trigger were written to tape.

The optical elements of the DISC are shown schematically in FIGURE 3.6. It was designed to accept Cerenkov light emitted at an angle of 24.5mrad with respect to the beam line axis. The chromatic corrector element corrected for the non-constant index of refraction of He with wavelength. The comatic corrector element corrected for spherical aberration in the mirror. All the optical elements were circularly symmetric about the optical axis.

It had an angular resolution of about 20μrad corresponding to a velocity resolution of $4\times10^{-7}c$. At 250GeV the difference in the Cerenkov angle between pions and kaons is ~75μrad and the difference in velocity is $\sim3.6\times10^{-6}c$ or about 1.1km/s.

At the beam line momentum of 250GeV the chromatic corrector was required to be as close as possible to the PMT windows. It was left in this position during the entire run. The slit width could be reduced to increase the resolution of the particle peaks during a pressure curve. This was often done during 'mini' pressure curves (explained below) around the kaon peak to ensure that the DISC was at the correct operating pressure. The standard opening width of the slit was about 0.25mm. The X and Y position of the mirror was

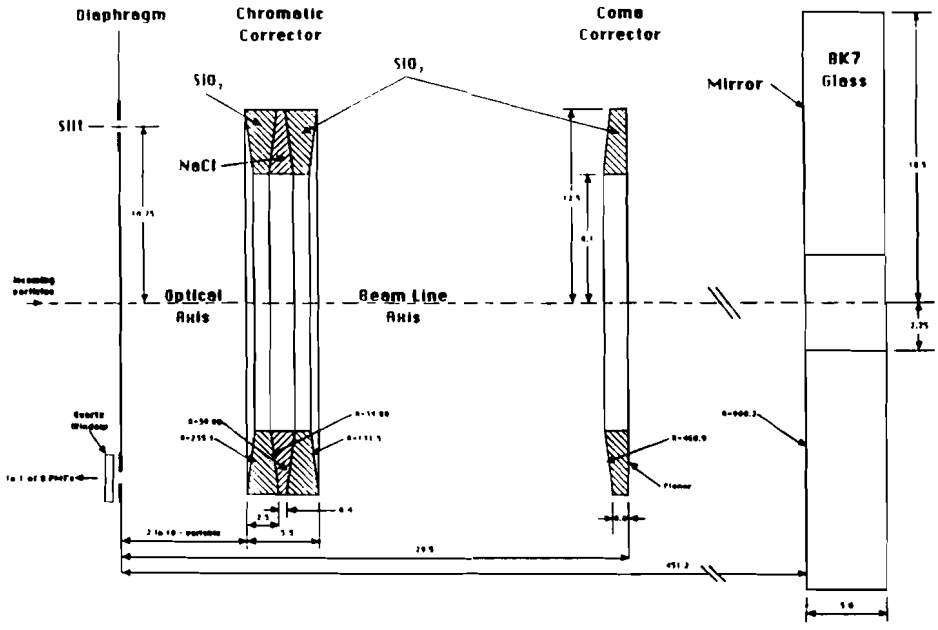

FIGURE 3.6
DISC Optical Assembly

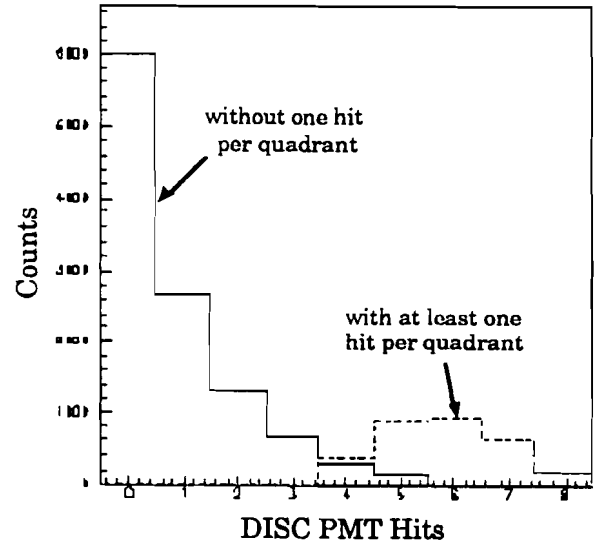

FIGURE 3.7
DISC Phototube coincidences

changed for different beam tunes which altered the path of the particles through the DISC.

FIGURE 3.7 shows the number of DISC PMT coincidences for each coincidence level as well as the number which also satisfied the 1 hit/quadrant requirement for a single tape.

DISC Operation and Performance

A vacuum pump was connected to the DISC main vessel as shown in FIGURE 3.3 to remove air from the DISC. The DISC would be pumped down and then filled with Helium gas. This process would be repeated until the location of the particle peaks did not change between purges indicating a pure He gas sample. Three successive fill/purges were sufficient to provide no observable He contamination.

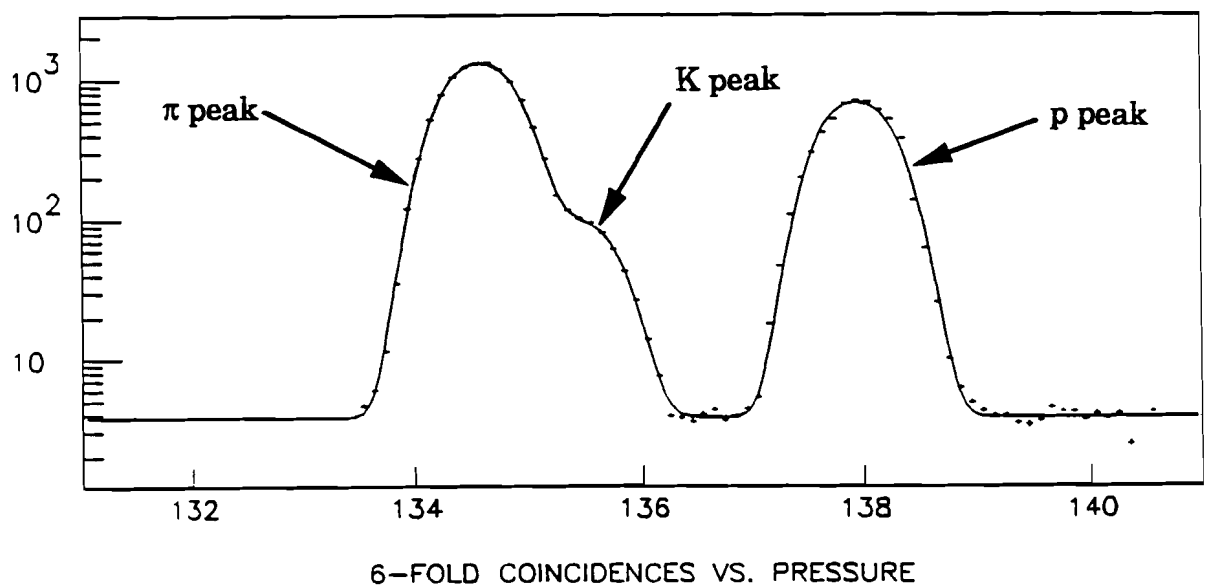

FIGURE 3.8
Fitted DISC Pressure Curve

A pressure curve allowed us to determine the correct He pressure for tagging incident kaons. The DISC pressure would first be set to a value less than the pressure required to tag pions. An online program would then incrementally increase the pressure in the DISC during the interspill period and record the number of DISC PMT coincidences of the types shown in TABLE 3.1. This process would be continued until the DISC pressure was

slightly higher than that required to tag protons. The results of a pressure curve are shown in FIGURE 3.8.

The kaon peak is visible as a bump on the high pressure side of the large pion peak. The bump was not visible in test plots which showed only coincidences in a single quadrant and becomes more prominent with increasing PMT coincidence level as expected. Increasing the coincidence level, decreasing the slit width or decreasing the beam collimator hole size provided much better separation of the π and K peaks. 'Mini' pressure curves using this better resolution covering the region around the kaon peak were performed regularly to ensure that the DISC system was operating properly.

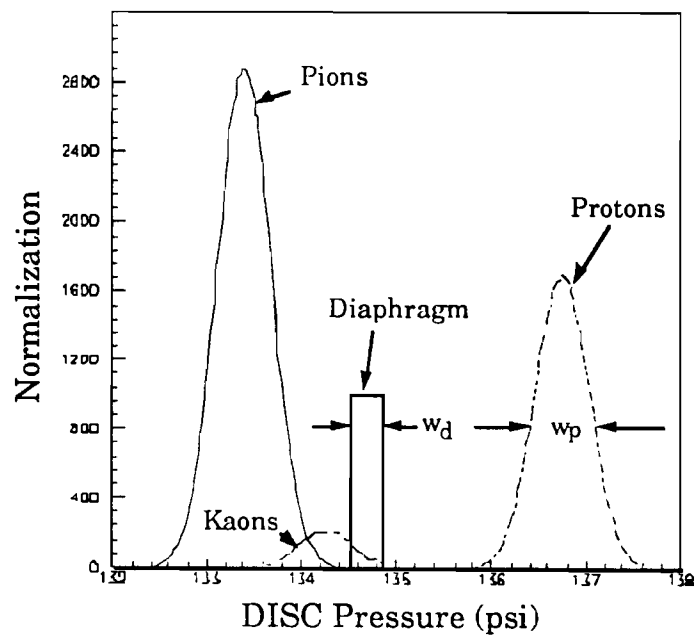

FIGURE 3.9
Elements of the fit to the DISC Pressure Curves

The DISC pressure curve shown in FIGURE 3.8 was fit to a set of three gaussians convoluted with a box function (as shown in FIGURE 3.9). The convolution results in the following equation:

$$S(P) \equiv S_\pi(P) + S_K(P) + S_p(P) + B$$

where
$$S_\pi(P) = N_\pi\left\{\mathrm{erf}\left[\frac{P_\pi - P + w_d}{w_p}\right] - \mathrm{erf}\left[\frac{P_\pi - P - w_d}{w_p}\right]\right\}$$

$$S_K(P) = N_K\left\{\mathrm{erf}\left[\frac{P_K - P + w_d}{w_p}\right] - \mathrm{erf}\left[\frac{P_K - P - w_d}{w_p}\right]\right\}$$

$$S_p(P) = N_p\left\{\mathrm{erf}\left[\frac{P_p - P + w_d}{w_p}\right] - \mathrm{erf}\left[\frac{P_p - P - w_d}{w_p}\right]\right\}$$

$$B = \text{constant}$$

and we have used the error function given by:

$$\mathrm{erf}(x) = \int_0^x e^{-t^2}\,dt$$

The gaussians, all with identical width (w_p), represent the radial hit distribution of the photons for each particle type in the plane of the diaphragm while the box function, of width w_d, represents the slit. P_π, P_K and P_p are the fitted locations of the centre of the pion, kaon and proton peaks respectively while N_π, N_K and N_p are their respective normalizations. The background term accounts for random coincidences between the DISC phototubes which were independent of the DISC He pressure. Seven full pressure curves were recorded during the run. The results of the fits to these pressure curves provide an indication of the linearity of the pressure-temperature relationship (FIGURE 3.10) and a measure of the beam composition (TABLE 3.2). The DISC-measured beam compositions (the *a priori* beam probabilities) are in rough agreement with the expected beam compositions calculated before the run. All subsequent calculations in the experiment use the measured values for the beam probabilities.

In practice, the proton curve was fit first because it was removed from the pion and kaon curves. It was fit with floating normalization, position, and diaphragm and photon peak widths. The entire curve was then fit after fixing the diaphragm and photon peak widths at the values given by the proton fit. Typical widths of the photon peaks were ~.350psi while the fitted diaphragm widths were ~.250psi.

The DISC pressure to tag kaons varied linearly with the He gas temperature as would be expected from the ideal gas law. This relationship was used to ensure that the DISC remained at the correct pressure throughout a run. An Interspill process (see Chapter 3: ON-Line Monitoring: The Interspill system) would check the DISC temperature and pressure and set an alarm if the DISC pressure strayed too far from its expected setting for the current temperature.

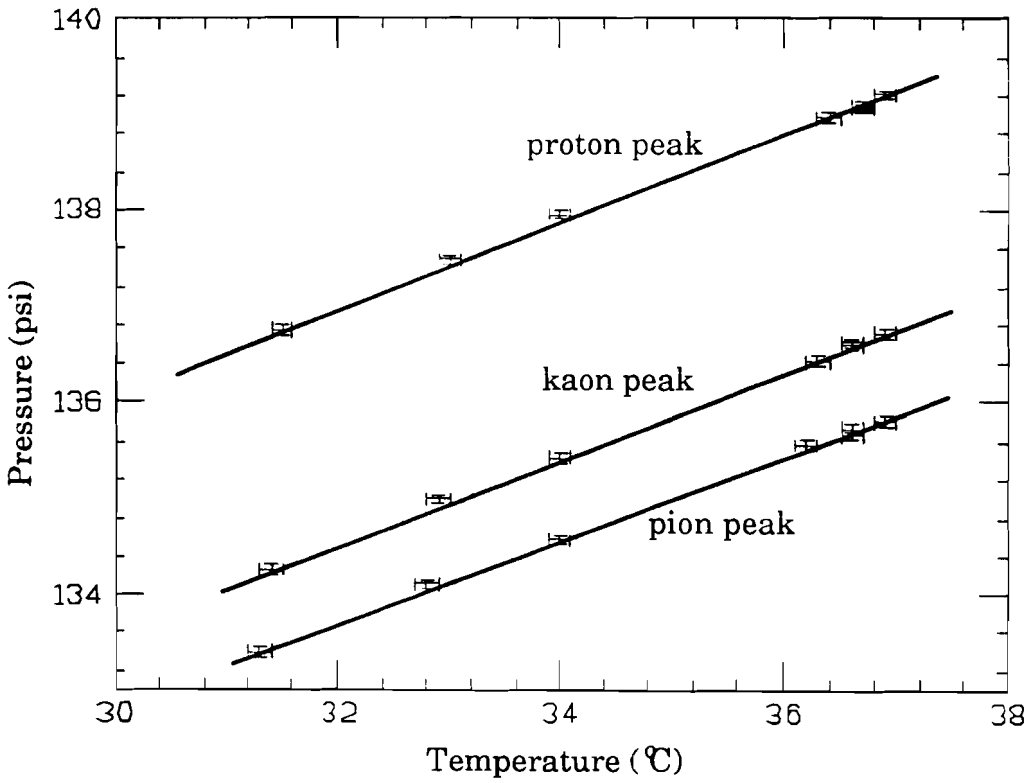

FIGURE 3.10
Particle Peak Pressure vs. Temperature in DISC

The fitted parameters of the full pressure curves also provided the information required to calculate π contamination levels in the kaon signal as a function of the offset from the fitted location of the K peak. FIGURE 3.11 shows the results of this calculation for a particular pressure curve. Pion contamination is less at a given pressure for higher

PMT coincidence levels and is less than about 1% at 0.4 p.s.i above the expected kaon peak pressure in all cases. We studied how the pion contamination changed as the parameters

TABLE 3.2
E769 Expected[28] and Measured Beam Composition

	Negative Beam		Positive Beam	
Particle Type	Expected	Measured	Expected	Measured
π	90%	93 ± 1%	60%	61 ± 3%
K	7.7%	5.2 ± 0.7%	6.5%	4.4 ± 0.2%
p	2.8%	1.5 ± 0.3%	34%	34 ± 3%

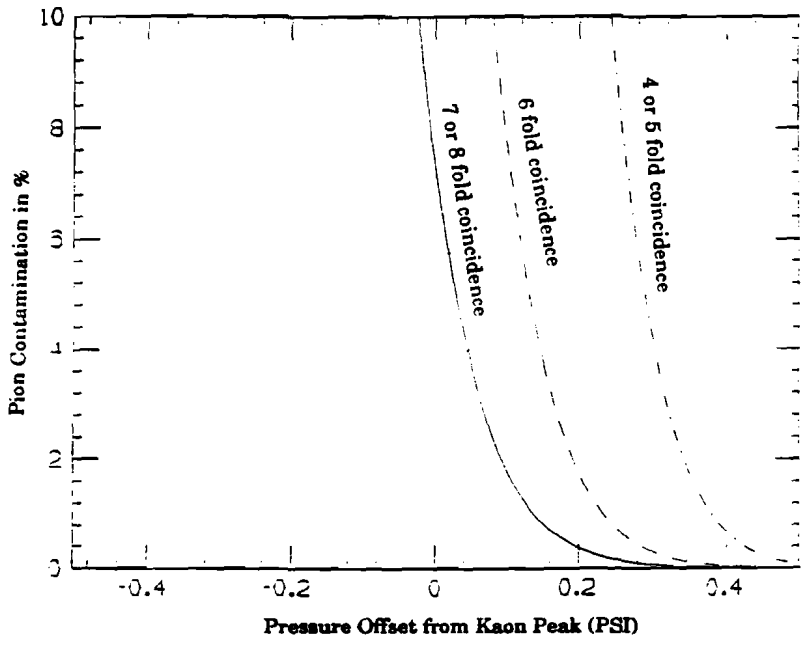

FIGURE 3.11
Pion Contamination level vs. Pressure Offset from Kaon Peak

28 Jeff Spalding, E769 member and Head of the Research Facilities Dept. of the Research Division at FNAL, personal correspondence. No errors were quoted on these values.

were varied from their fitted values by ±10% and found that changing the parameters in this range caused almost no change to the pion contamination levels at large offsets (>0.4 p.s.i.). The DISC pressure during the run was usually set to be about 0.4 p.s.i. above the expected location of the kaon peak.

The DISC efficiency for tagging kaons is shown in FIGURE 3.12 for 5 different pressure curves. The maximum efficiency always occurs at the kaon peak. The efficiency drops with increasing pressure away from the kaon peak but drops slowly for the four PMT coincidence condition so that even at an offset of +0.4 p.s.i. the efficiency is usually greater than 1/2 the maximum efficiency.

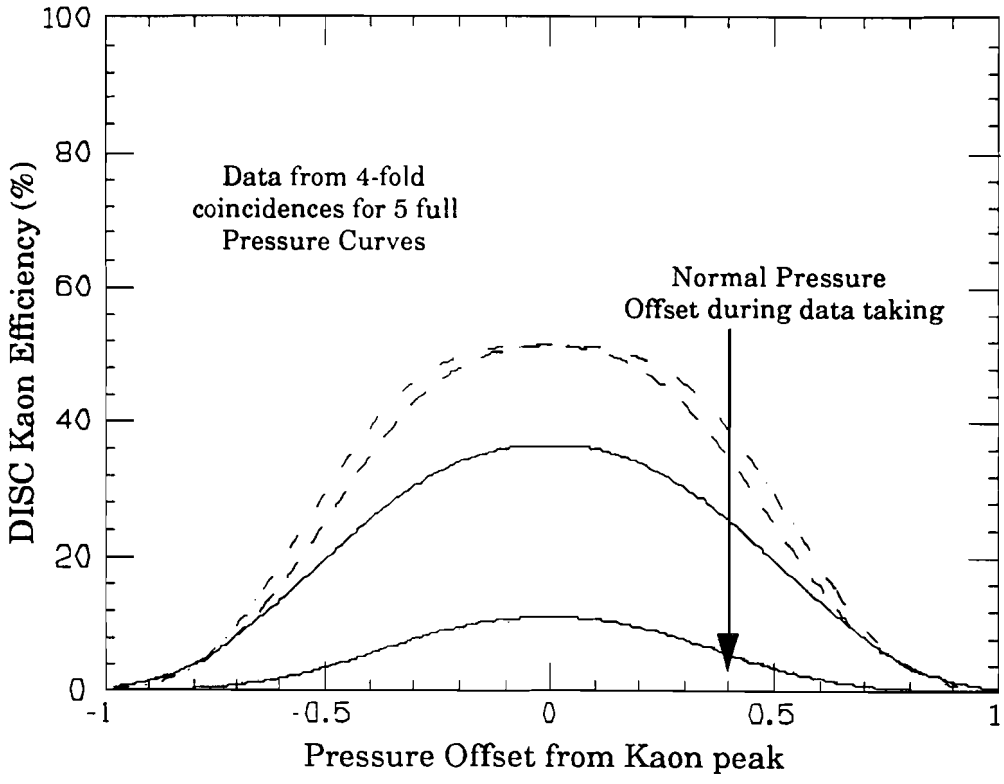

FIGURE 3.12
DISC efficiency vs. Pressure Offset from Kaon Peak

DISC Off-line Analysis

The DISC off-line analysis routine allowed the user to determine the beam particle identification probability on an event-by-event basis. It first created a database of DISC information from the scaler event records (see Chapter 3: The Data Acquisition System) throughout the run. For each scaler event we recorded the run and spill number and then calculated the beam particle probabilities from the DISC assuming a 4-fold DISC PMT coincidence level. If we know the DISC efficiency and there is NO DISC tag in a particular event we can calculate a *corrected a priori* probability for the beam particle. If the DISC efficiency for each particle type i ($i = \pi$, K, p) is represented by ε_i and the *a priori* probabilities for the three beam particles are given by f_π, f_K and f_p then in the sample of beam particles with NO DISC tag the corrected beam probabilities are given by:

$$f'_\pi = \frac{(1-\varepsilon_\pi)f_\pi}{S}$$

$$f'_K = \frac{(1-\varepsilon_K)f_K}{S}$$

$$f'_p = \frac{(1-\varepsilon_p)f_p}{S}$$

where $$S = \sum_{i=\pi,K,p}(1-\varepsilon_i)f_i = 1 - \sum_{i=\pi,K,p}\varepsilon_i f_i$$

All events within a given spill with the same number of PMT hits had identical beam particle probabilities.

When ≥4 PMTs fired, including at least one PMT in each of the four DISC quadrants, the particle probabilities were calculated from the fitted pressure curves. Since our experiment possessed no way of distinguishing different beam tune conditions off-line, we averaged the probabilities calculated from the parameters for all the existing pressure curves.

The DISC pressure curves could also be used to determine the energy of the beam. The separation in pressure (P) at which each particle produced light of the required Cerenkov angle (θ_c) is a measure of γ which is related to their momenta (p):

$$(n_o - 1)P_\pi \approx \frac{\theta_c^2}{2} + \frac{1}{2\gamma_\pi^2}$$

$$(n_o - 1)P_p \approx \frac{\theta_c^2}{2} + \frac{1}{2\gamma_p^2}$$

where the sub-scripts π and p refer to the pion and proton respectively while n_o is the index of refraction of He at STP. We use the pion and proton peaks because they were well defined and separated in the DISC pressure curves. Subtracting the second equation from the first yields

$$2(n_o - 1)(P_\pi - P_p) \approx \frac{1}{\gamma_\pi^2} - \frac{1}{\gamma_p^2}$$

$$= \frac{m_\pi^2}{p^2 + m_\pi^2} - \frac{m_p^2}{p^2 + m_p^2}$$

Letting

$$A = 2(n_o - 1)(P_\pi - P_p)$$

$$B = m_\pi^2(A - 1) + m_p^2(A + 1)$$

$$C = Am_\pi^2 m_p^2$$

the square of the beam momentum is the solution of a quadratic equation and is given by

$$p^2 = \frac{-B + \sqrt{B^2 - 4AC}}{2A}.$$

The beam line momentum was found to be 243±10GeV. This is in agreement with the expected momentum of 250GeV.

The Transition Radiation Detector (TRD)

Theory, Design and Construction

Charged particles passing from one medium into another with a different dielectric constant emit radiation due to the readjustment of charges in the medium associated with the changes in the particle's electro-magnetic field. Most of this Transition Radiation

(TR) is emitted in a characteristic depth[29] $D=\gamma(\omega_p)^{-1}$ in the new medium in the form of X-rays. ω_p is the plasma frequency of the medium given by $\omega_p^2 = 4\pi\alpha Z\rho N_A(Am_e)^{-1}$. γ is the Lorentz contraction factor, α is the fine structure constant, Z is the number of protons/nucleus in the gas, A is its atomic weight, N_A is Avogadro's number, ρ is the gas density and m_e is the mass of the electron. The TR is emitted almost exclusively in the forward direction into a cone with opening angle $\theta \sim \gamma^{-1}$. The total energy emitted in the form of TR is given by $E_{TR} = \frac{2}{3}\alpha\omega_p\gamma$ while the average number of X-rays emitted per surface transition is $\langle N_{TR}\rangle \sim \alpha/2$.[30]

To maximize the amount of TR the number of transitions between media should be made as large as possible. In order that the TR not be absorbed by the medium the material should be thin, yet it must also be thicker than the characteristic depth (*D*) for TR.

The E769 TR Detector (TRD) used 24 radiator-chamber modules in series as shown in FIGURE 3.13. A more detailed description of the detector can be found elsewhere[31,32]. Each of the assemblies contained 200 12.7μm thick polypropylene radiator foils separated by approximately 180μm gaps maintained by a nylon net material. The nylon net had a hole cut through the middle in order to reduce the self-absorption of the TR. The TRD provided an estimated 8.3% of an interaction length and 16.9% of a radiation length in the beam line.

TR photons (X-rays) emitted in the radiators were detected by two succesive multi-wire (64 wires per plane) proportional chambers with 1mm wire spacings and an active area of about 75cm×65cm. The chambers used a 90% xenon / 10% methylal gas mixture achieved

---

29 J.D. Jackson. Classical Electromagnetism, p.687.

30 R.C. Fernow, Introduction to Experimental Particle Physics, Cambridge University Press (1986) p. 295.

31 D. Errede, M. Sheaff, H. Fenker, L. Lueking, P. Mantsch, and R. Jedicke, Design and Performance Characteristics of the E769 Beamline Transition Radiation Detector, accepted by NIM for publication.

32 D. Errede, M. Sheaff, H. Fenker, L. Lueking, P. Mantsch, A High Rate Transition Radiation Detector for particle Identification in a hadron beam, Fermilab-Conf-89/170-[E769], August 1989.

by bubbling the xenon through methylal at 0°C. The gain of the chambers was very dependent on the Xe/methyal admixture which was determined by the methylal temperature. A refrigerating unit was built to maintain the methylal to within a few tenths of a degree of 0°C.

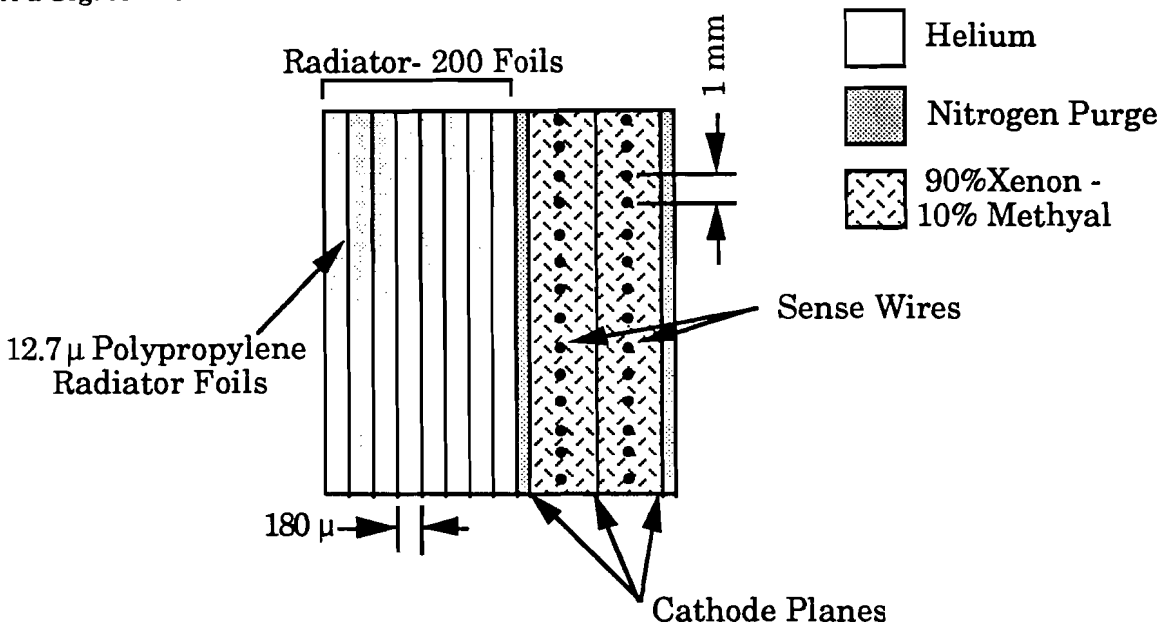

FIGURE 3.13
Schematic of one of the E769 TRD radiator-chamber assemblies

The radiator volume was flushed with Helium because it has a lower plasma frequency than air making it a better gap material. Nitrogen was continuously flushed through a buffer region between the Xe and the radiator region to eliminate the possibility of He contamination in the xenon/methylal mixture.

The 64 wires in each proportional chamber were divided into sets of four wires which were wire OR'd together. Each of these 16 signals was pre-amplified at the chamber and sent to amplifier/shaper/discriminator cards which were built at FNAL and based on a slightly modified design of a similar card for the Collider Detector Facility (CDF)[33]. The

33 R. J. Yarema et al., A Surface Mount Amplifier-Shaper-Discriminator and Pre-amplifier for the Fermilab CDF Tracking Chambers, IEEE Transactions on Nuclear Science, Vol. 33, No. 1, February 1986.

16 discriminated chamber signals were combined in a logical OR using a LeCroy 4564. Each of these digital signals from the 48 planes in the TRD were input to a LeCroy 4448 gated latch (with 48 bits). The latch was provided by a scintillator array just upstream of the TRD assembly.

An on-board Fe^{55} source built into the TRD assembly gave a readily observable signal for calibrating the TRD and ensured that the gain between individual TRD modules was identical.

System Performance

The TRD was necessary in the positive beam where protons provided a significant fraction of the beam (~34%). In the negative beam configuration ~93% of the incident particles were pions. In this case a positive tag for kaons (~5%) using only the DISC information was sufficient for beam ID. FIGURE 3.14 shows a TRD plane count distribution for positive beam. The peak near 5 planes is due to the protons while the peak at about 18 plane counts is due to pions. FIGURE 3.15 is a plot of the number of DISC phototubes to fire in an event versus the number of TRD plane counts in the same event. Note that there is very good separation between the kaon peak at high DISC PMT coincidence levels and the pion and proton peaks which are themselves separated by about 10 to 15 TRD plane counts.

The high mass and correspondingly lower γ for protons implies that they emit less energy in the form of TR than pions in the E769 TRD. The peak due to the protons was caused by energetic delta rays liberated by the passage of the proton through the radiator assembly.

A TRD distribution from at least one tape from almost every positive beam run was fit to a function which is the sum of four binomial terms. Two of the terms are used to fit the proton peak while the other two binomials represent the pion peak. The use of two terms to represent each of the peaks was motivated by the fact that the front and back planes of each

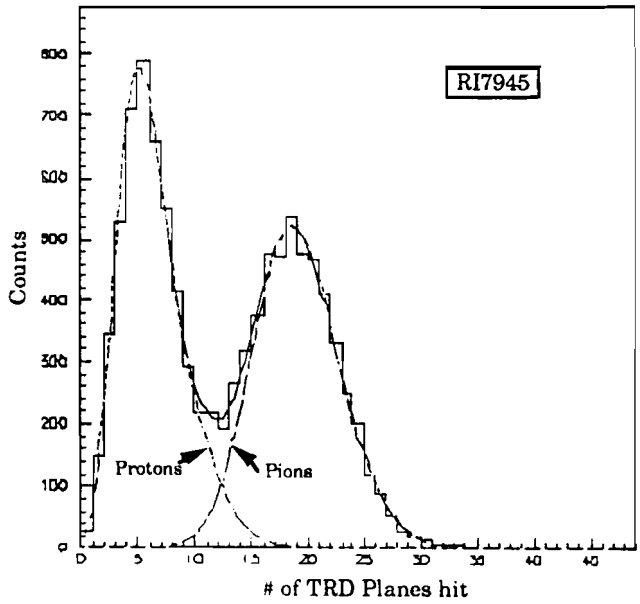

FIGURE 3.14
Fitted TRD plane distribution for positive data.
DISC tagged Kaons have been removed from this sample

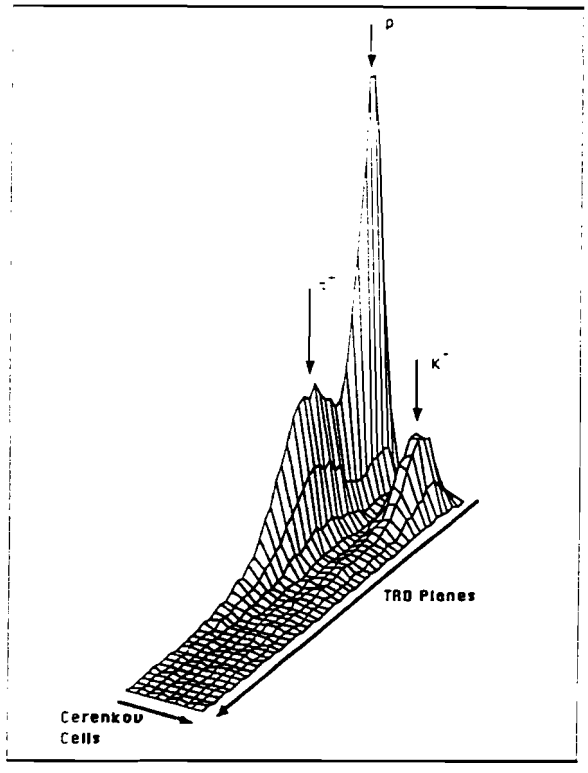

FIGURE 3.15
DISC PMT coincidences vs. TRD plane counts

of the TRD modules responded slightly differently to the TR. The relative normalization of the pion to proton curve was fixed at the ratio 4930:5070 determined from the average of fits to many different TRD distributions where the normalization was not fixed.

The function is given by:

$$F(n_{TRD}) = F_\pi + F_p$$

$$F_\pi = N_\pi \binom{48}{n_{TRD}} p_1^{n_{TRD}} (1-p_1)^{48-n_{TRD}} + (4930 - N_\pi)\binom{48}{n_{TRD}} p_2^{n_{TRD}} (1-p_2)^{48-n_{TRD}}$$

$$F_p = N_p \binom{48}{n_{TRD}} p_3^{n_{TRD}} (1-p_3)^{48-n_{TRD}} + (5070 - N_p)\binom{48}{n_{TRD}} p_4^{n_{TRD}} (1-p_4)^{48-n_{TRD}}$$

where p_1 and p_2 are the probabilities for the binomial distribution corresponding to the pion peak. N_π is the normalization of the first binomial in the pion distribution. p_3, p_4 and N_p have similar definitions for the proton peak. n_{TRD} is the number of TRD planes to fire. The results of the fit to a TRD distribution are included in FIGURE 3.14.

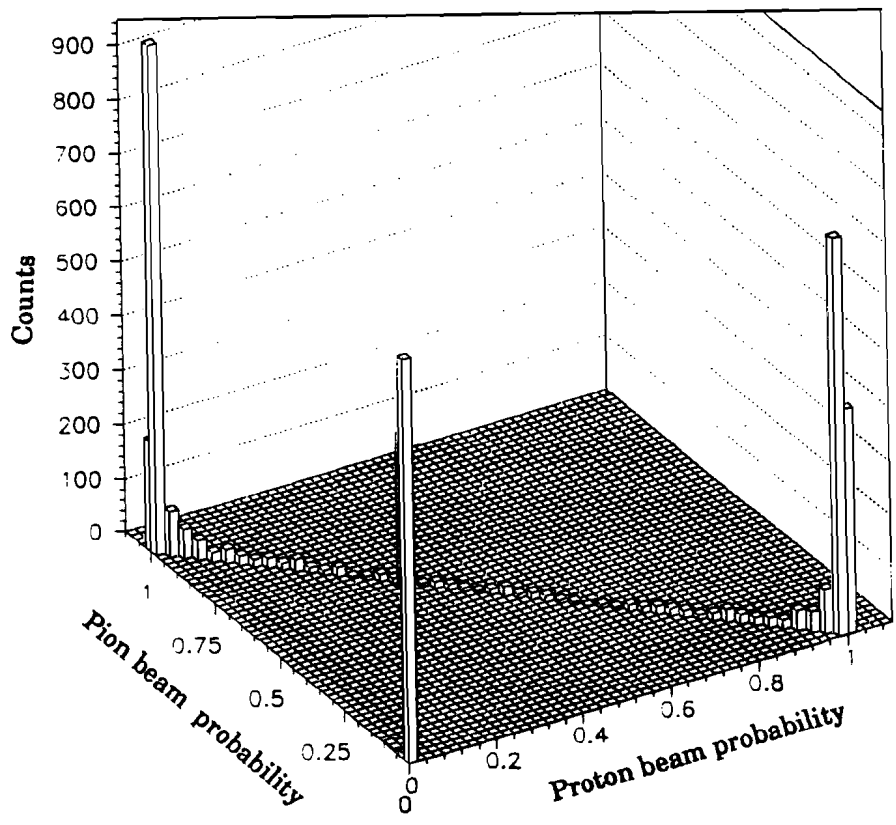

FIGURE 3.16
π probability as a function of p probability

These fits allow a determination of the probability that the incident particle was a proton (with a small contribution from non-DISC tagged K) or pion as well as the efficiency and contamination levels for each signal due to the other particle type. FIGURE 3.16 shows the pion probability plotted as a function of the proton probability. Note the very good separation between identified π and p. The peak near (0,0) is the DISC tagged kaon sample. FIGURE 3.17 shows the TRD pion signal contamination by protons and the efficiency for tagging pions as a function of the calculated pion probability. The values are the average over all the positive runs for which TRD distributions exist while the error bars are the standard deviation of these values. For a pion probability greater than 90% the average efficiency is about 85% while the proton contamination is only about 1%.

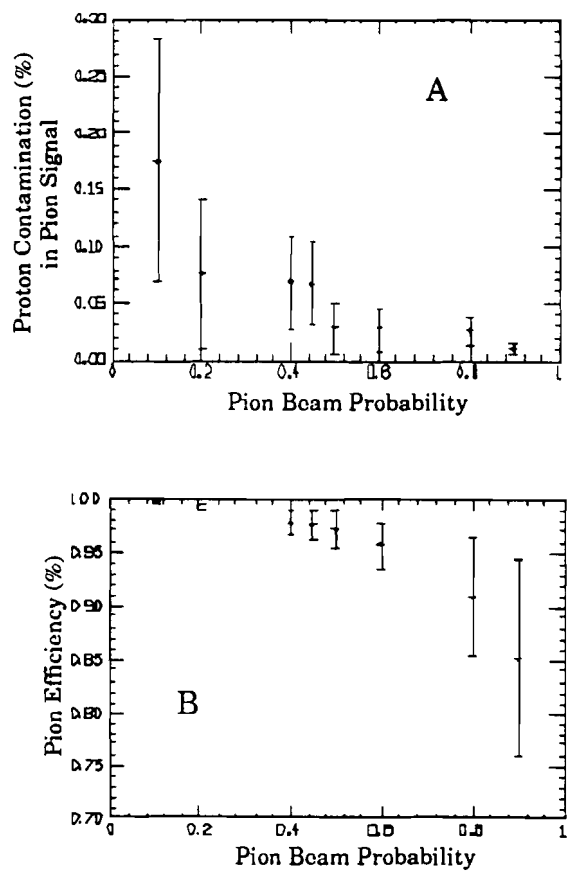

FIGURE 3.17
TRD pion contamination and Efficiency
A) pion contamination by protons as a function of pion probability
B) pion efficiency as a function of pion probability

The E769 segmented target

The E769 target assembly was designed to provide a series of thin targets of various atomic weight in order to study the A-dependence of the charm cross section. In addition, its configuration was optimized for simplification of the off-line analysis. Each of the foils had a thickness of about 100 to 250μm which was less than the expected vertex resolution of the SMD telescope in the beam direction. The foils were separated by an average distance of 1.367mm (std. dev. = .012mm) to ensure that we could determine the foil in which the primary interaction occured, and thereby know the z-position of the interaction, to an accuracy greater than that provided by the rest of the detector. The target was designed so that E769 could define a clear separation between an A^1 and $A^{2/3}$ dependence since $(A_W/A_{Be})^1 \sim 20$ and $(A_W/A_{Be})^{2/3} \sim 7.5$.[34]

The sequence of foil materials in the target was chosen to minimize multiple scattering in the downstream foils. The tungsten foils were placed in the second through fifth positions so that they could be eliminated from studies which are sensitive to multiple scattering. A detailed summary of the target is shown in TABLE 3.4. TABLE 3.3 shows the aggregate properties of the target.

A schematic of the target as well as the location of 3 target area scintillators are shown in FIGURE 3.20. The two scintillators upstream of the target overlapped completely except that one scintillator (the HALO scintillator) had a hole of ~9.5mm radius drilled through it and aligned with the target. A signal in the BEAM SPOT counter and NOT in the HALO counter defined a single incident beam particle. The interaction scintillator after the target had an active circular area of about 11.4cm^2. The signal threshold of ~5×(minimum ionizing) defined whether or not an interaction had occured in the target.

---

34 Pion and Kaon Production of Charm and Charm-Strange states - E769 FNAL Proposal, 1985.

TABLE 3.3
Aggregrate Properties of the Segmented Target

Material	Total Thickness (mm)	Total Interaction Lengths (%)	Total Radiation Lengths (%)
Be†	3.629±0.033	0.892±0.008	1.03±0.01
Al‡	1.261±0.008	0.320±0.002	1.42±0.01
Cu‡	0.761±0.006	0.504±0.004	5.32±0.04
W‡	0.383±0.008	0.399±0.008	11±0.5
Total	6.034±0.035	2.115±0.012	18.8±0.5

† purity greater than 99.5%
‡ purity greater than 99.95%

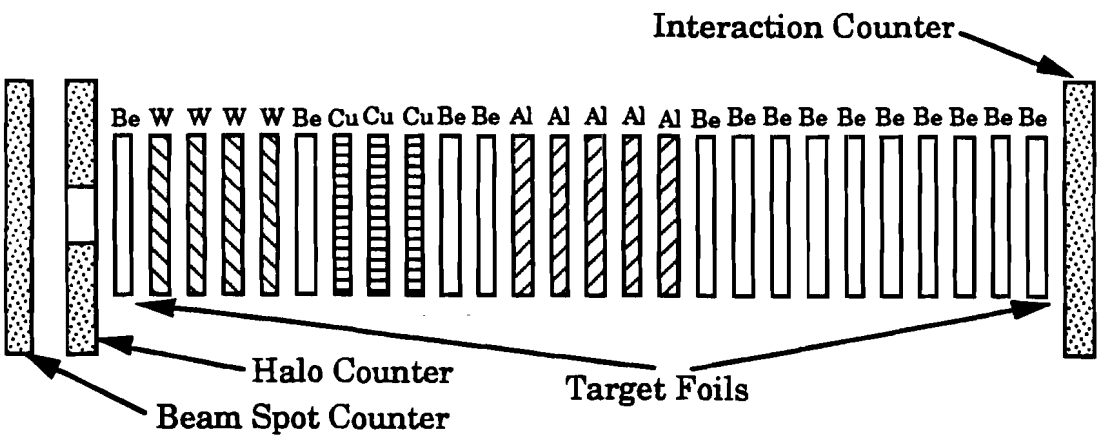

FIGURE 3.20
The E769 target and counter/scintillator arrangement

TABLE 3.4
Specifications of the Segmented Target

Foil No.	Material (Atomic Weight)	Thickness (±~0.006mm)	% Interaction Lengths (±~3%)	% Radiation Lengths (±~3%)	Z-position of foil* (±0.05mm)
1	Be (9)	0.250	0.0614	0.0708	43.46
2	W (184)	0.097	0.101±5%	2.8±5%	41.83
3	W (184)	0.095	0.0991±5%	2.7±5%	40.39
4	W (184)	0.094	0.0980±5%	2.7±5%	38.92
5	W (184)	0.097	0.101 ±5%	2.8±5%	37.45
6	Be (9)	0.255	0.0627	0.0722	35.99
7	Cu (63)	0.250	0.166	1.75	34.37
8	Cu (63)	0.258	0.171	1.80	32.75
9	Cu (63)	0.253	0.168	1.77	31.13
10	Be (9)	0.276	0.0678	0.0782	29.49
11	Be (9)	0.244	0.0600	0.0691	27.85
12	Al (27)	0.249	0.0632	0.28	26.24
13	Al (27)	0.257	0.0652	0.29	24.62
14	Al (27)	0.251	0.0637	0.28	23.01
15	Al (27)	0.251	0.0637	0.28	21.39
16	Al (27)	0.253	0.0642	0.28	19.77
17	Be (9)	0.266	0.0654	0.0754	18.14
18	Be (9)	0.256	0.0629	0.0725	16.52
19	Be (9)	0.267	0.0656	0.0756	14.89
20	Be (9)	0.266	0.0654	0.0754	13.25
21	Be (9)	0.263	0.0646	0.0745	11.63
22	Be (9)	0.261	0.0641	0.0739	10.03
23	Be (9)	0.262	0.0644	0.0742	8.38
24	Be (9)	0.245	0.0602	0.0694	6.77
25	Be (9)	0.263	0.0646	0.0745	5.15
26	Be (9)	0.255	0.0627	0.0722	3.52

* Z-position of foil is measured from the upstream side of the foil to the downstream end of the target container

The Downstream SMD system

General Properties

The vertex telescope of SMDs after the target used 11 planes of silicon incorporating over 6000 readout channels. TABLE 3.5 summmarizes some of the aspects of this system. The V-planes were rotated by 20.5° about the beamline with respect to the vertical axis. The active area of each SMD plane was square. The z-position is measured relative to the E769 reference frame in which z=0cm corresponds to a location between the first SMD plane and the interaction counter. A schematic representation of an SMD plane is shown in FIGURE 3.19.

TABLE 3.5
SMD Vertex Detector Summary

Plane No.	No. of strips†	Active width (mm)	Z-position (±~0.005cm)
BX	688	24.8	0.246
BY	688	24.8	0.503
X1	512	25.6	1.931
Y1	512	25.6	2.934
V1	512	25.6	6.655
Y2	767	38.4	10.979
X2	512	25.6	11.325
V2	767	38.4	14.932
X3	512	25.6	19.853
Y3	1000	50.0	20.202
V3	1000	50.0	23.878

† BX and BY have a 25μm pitch in their central 384 strips . All other downstream SMD planes have 50μm pitch.

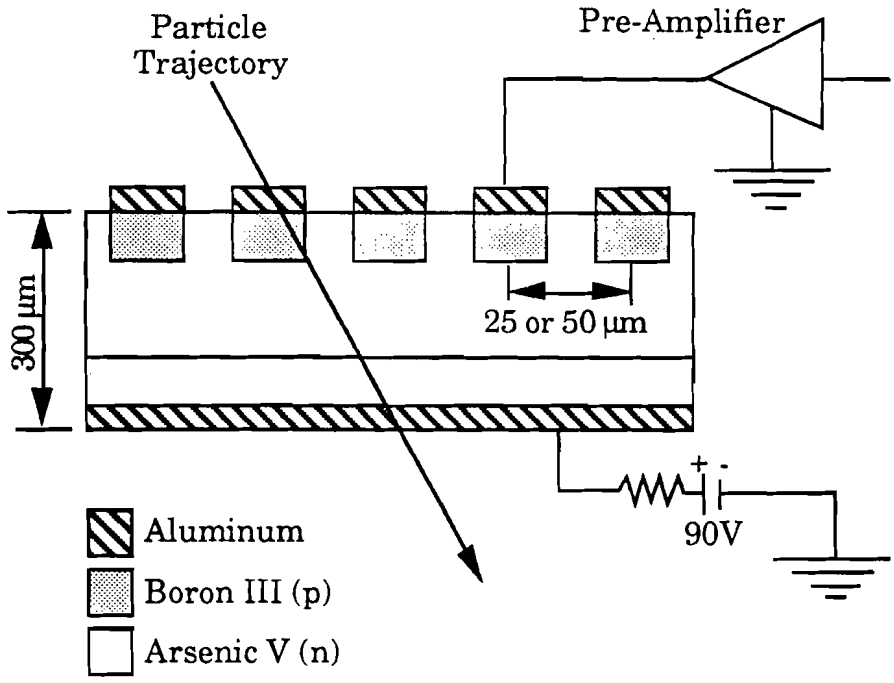

FIGURE 3.19
Schematic construction of a SMD plane

A minimum ionizing particle passing through the ~300µm thick silicon plane produced about 25000 e^-/e^+ hole pairs in the e^- depleted silicon along its trajectory. The e^- holes drift towards the aluminum strips due to a potential difference of about 70V across the silicon (except X1, Y1 and V1 which were at 90V). The small amount of charge collected at any strip necessitated the use of pre-amplifiers only a few centimetres from the silicon plane.

The preamplified signals were sent on shielded ribbon cables to amplifier/discriminator/latch cards located only a couple of metres from the planes. The average discriminator threshold was set to about 0.5mV (about 1/2 the signal produced by a single minimum ionizing particle). Each strip on an SMD plane set a latch bit in a corresponding card to 1 (On) if the strip was hit or 0 (Off) if the plane was not hit. These cards were chained together into groups, each group being read out serially by a method in which each successive card in the chain passed its 8 latch bits to the next card in the chain

until the entire group's record had been read by a NANOSCANNER CAMAC card located in the counting room.

System Performance and Efficiency

The 25μm planes had a reduced efficiency[35] (~70%) relative to the 50μm (~92%) planes because of electronic and noise problems. The achieved resolution of the planes, ~16μm and ~21μm for the 25μm and 50μm planes respectively, should be compared to the theoretical resolutions given by $25\mu m/(\sqrt{12})=7.2\mu m$ and $50\mu m/(\sqrt{12})=14.4\mu m$. The downstream SMD vertex telescope gave typical resolutions of 15μm, 15μm and 100μm in the x, y and z directions respectively. The following FIGURE 3.21 of primary vertex z-locations shows that the vertex telescope resolves the foil structure of the target. This plot should be compared to TABLE 3.3 giving the ordering of the foils in the target.

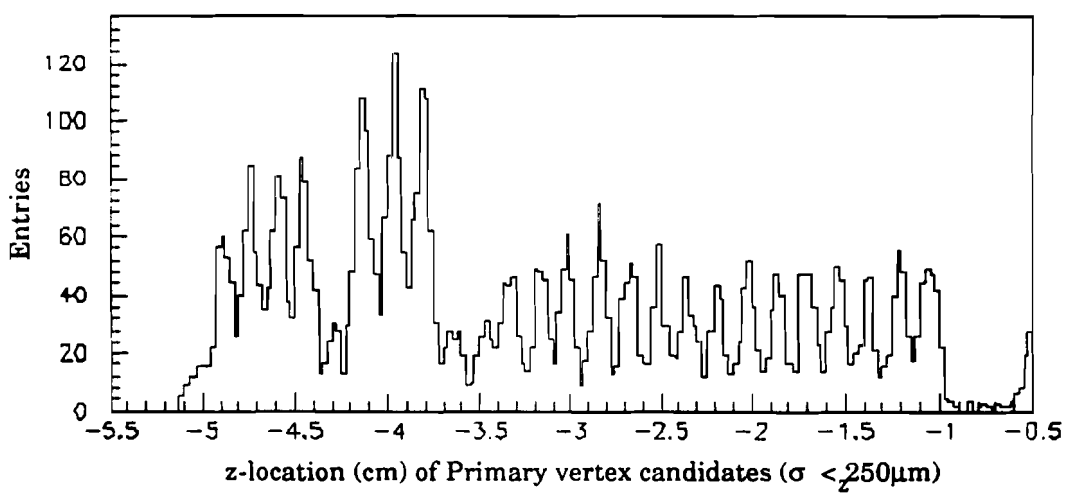

FIGURE 3.21
Primary vertex z-location using SMD tracks

35 P. Karchin, Z. Wu, E769 Internal Memo, The Efficiencies and resolution studies of the SMD planes, 12 April 1989.

The Downstream PWC system

To increase the downstream tracking redundancy and resolution in the y-direction E769 introduced two 288 wire PWCs with 2mm pitch downstream of the target to measure the y-position of tracks. Each of the chambers had an active area of about 0.576m × 0.576m. The first chamber (P1Y1) was situated just upstream of D1-1 while the second chamber (P1Y2) was placed between the two D1 chambers.

The chambers were constructed from five G10 boards. The outermost face on each side of the chamber was covered by a thin, grounded, aluminized mylar sheet. On both sides of the wire plane were thin aluminized mylar sheets held at about -1800V with respect to the grounded wires. An 83% Argon / 17% CO_2 / 0.3% Freon[36] mixture flowed through the chamber between the two cathode planes and also between the cathode planes and the outer grounded mylar sheets in order to minimize the pressure difference between the inside and outside faces of the cathode plane. This helped to ensure that the cathode plane remained at a constant distance from the wire plane and therefore kept the gain across the face of the chamber approximately constant.

The Drift Chamber System

Physical Characteristics including the Gas System

The E769 Drift Chamber (DC) system employed 35 planes of sense wires in seven separate gas box assemblies. The gas boxes were broken into four groups which were located 1) before the first analysis magnet (M1), 2) between M1 and the second analysis magnet (M2), 3) after M2 and 4) after the second Cerenkov counter (C2). These four groups were known as D1, D2, D3 and D4 respectively. The positions of the assemblies are shown on both the scale view (FIGURE 3.1) and schematic (FIGURE 3.2) of the spectrometer. Each group of chambers was divided into different assemblies containing sets of 4 (D1) or 3 (D2,

36 personal correspondence with Howard Fenker, E769 member.

D3 and D4) sense wire planes. The assemblies were labelled according to their group and order of appearance. e.g. D3-3 was the third DC assembly in the D3 grouping.

Each of the drift chamber assemblies was based on almost the same High Voltage (HV) and sense wire plane system. A sense wire plane was a plane of wires containing both sense wires (at which the electron avalanche occured) and HV wires for field shaping. The sense wires in all the DC planes were 25μm gold plated tungsten while all the field shaping (HV) wires were 127μm Be-Cu except for D2-4 and D3-4 where the HV wires were

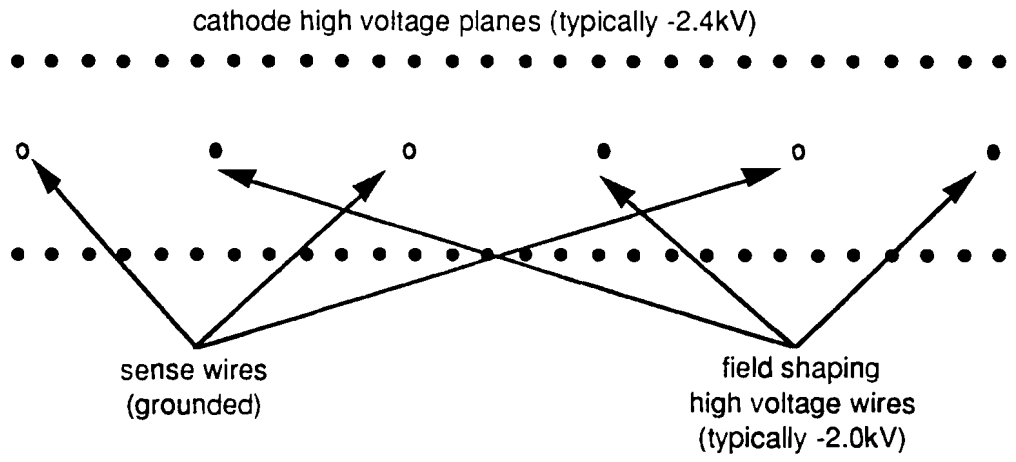

FIGURE 3.22
Drift Chamber Sense and HV plane orientation

slightly thinner at 125μm. An HV plane was a plane of wires which were all at the same HV setting. The sense wire planes were sandwiched between the HV planes as shown in FIGURE 3.22. Successive sense wire planes in the same assembly shared the HV plane between them.

The DC sense and HV wires were stretched at the same tension between G-10 polyurethane frames which were sandwiched together and placed into their airtight aluminum gas boxes. The gas boxes on all but D4 had thin Mylar windows to reduce the material seen by secondary particles as they traversed the detector. The windows on D4 were thin aluminum sheets.

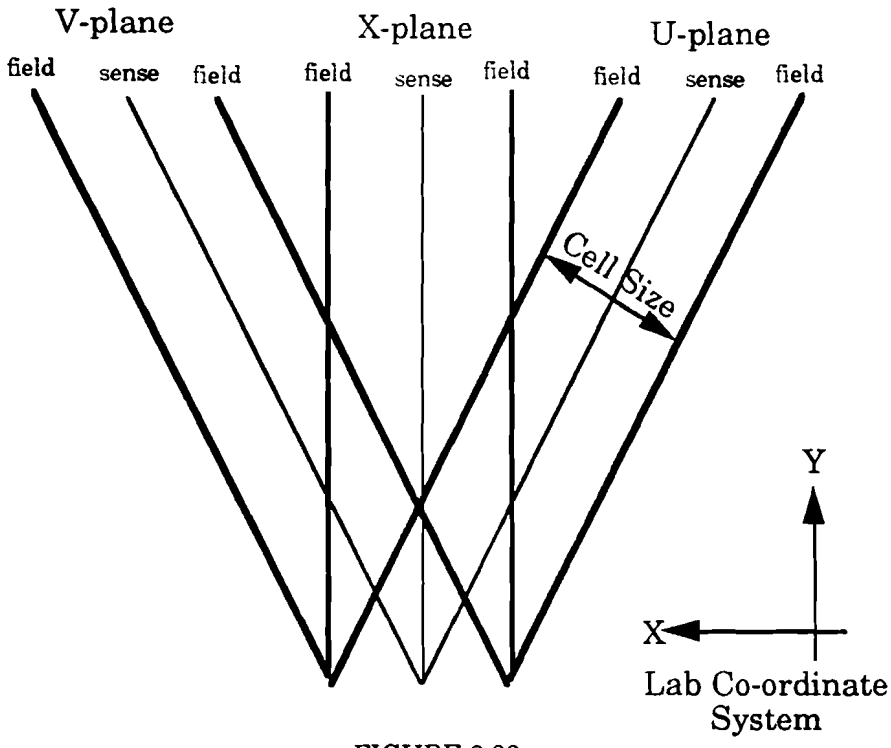

FIGURE 3.23
Orientation of the U, X, and V planes in the DC system

There were three different orientations of the wires in the sense planes. The X sense plane wires were stretched vertically to measure the x-position of the particle as defined in the E769 coordinate system (see FIGURE 3.23). The U and V sense plane wires were angled at ±20.5° from the vertical respectively. All the HV plane wires were aligned vertically except in D1 where they were horizontal. No correction was made in the reconstruction for the difference in z between the planes for a single space point measurement (a UXV combination) in a single DC assembly.

All the Drift Chambers received the same gas mixture of 50% ethane and 50% argon with ~1% ethanol used as a quenching and age-prevention agent. The ethanol was added by bubbling the 50/50 ethane-Ar mixture through 0° ethanol. The gas system automatically adjusted to different gas bottle and atmospheric pressure changes to maintain a constant pressure slightly above atmospheric pressure in each of the gas box assemblies.

The first drift chamber system (D1) was divided into two assemblies. The active area of the assemblies was about $0.91m^2$. Each of the assemblies had four sense wire planes in the order UVXX' as seen by the beam. The X' plane was an X-plane of wires offset from the first X-plane by half a cell width to solve the left-right ambiguity in track finding and aid in two track separation. Only the middle section of each of the D1 assemblies was covered by the X' wire plane since this section of the chambers received the highest flux of particles. Some of the sense wire plane characteristics in the D1 system are shown in TABLE 3.6.

TABLE 3.6
D1 Sense Wire plane Characteristics

Plane No.	Plane Type	Z-position (cm)	Sense Wire Separation‡(cm)	No. of sense wires
1	D1-1 U	153.6	0.4763	192
2	D1-1 V	154.6	0.4763	192
3	D1-1 X	158.7	0.4461	192
4	D1-1 X'	159.6	0.4461	96
5	D1-2 U	188.7	0.4763	256
6	D1-2 V	189.7	0.4763	256
7	D1-2 X	193.8	0.4461	256
8	D1-2 X'	194.7	0.4461	96

‡ Perpendicular distance between two sense wires in the same plane.

The second set of 12 drift chamber planes were divided into 4 assemblies of 3 planes each in the order UXV as seen by a beam particle. The first nine planes were located in a large gas box while the last three planes were in their own thinner gas box. These planes had an active area of about $3.9m^2$. The location and orientation of the sense wires in these planes are shown in TABLE 3.7.

The third set of 12 drift chamber planes were also broken into 4 assemblies of 3 planes each in the order UXV as seen by a beam particle. The first nine planes were located in a large gas box while the last three planes were in their own thinner gas box. These planes had an active area of about $4.6m^2$. The location and orientation of the sense wires in these planes are shown in TABLE 3.8.

TABLE 3.7
D2 Sense Wire plane Characteristics

Plane No.	Plane Type	Z-position (cm)	Sense Wire Separation‡(cm)	No. of sense wires
9	D2-1 U	382.4	0.8922	176
10	D2-1 X	384.0	0.9525	192
11	D2-1 V	385.5	0.8922	176
12	D2-2 U	424.9	0.8922	176
13	D2-2 X	426.5	0.9525	192
14	D2-2 V	428.1	0.8922	176
15	D2-3 U	466.6	0.8922	208
16	D2-3 X	468.2	0.9525	224
17	D2-3 V	469.8	0.8922	208
18	D2-4 U	497.7	0.8922	208
19	D2-4 X	499.3	0.9525	240
20	D2-4 V	500.9	0.8922	208

‡ Perpendicular distance between two sense wires in the same plane.

TABLE 3.8
D3 Sense Wire plane Characteristics

Plane No.	Plane Type	Z-position (cm)	Sense Wire Separation‡(cm)	No. of sense wires
21	D3-1 U	928.3	1.4870	160
22	D3-1 X	929.9	1.5875	160
23	D3-1 V	931.5	1.4870	160
24	D3-2 U	970.8	1.4870	160
25	D3-2 X	972.4	1.5875	160
26	D3-2 V	974.0	1.4870	160
27	D3-3 U	1012	1.4870	160
28	D3-3 X	1014	1.5875	160
29	D3-3 V	1016	1.4870	160
30	D3-4 U	1044	1.4870	160
31	D3-4 X	1046	1.5875	192
32	D3-4 V	1048	1.4870	160

‡ Perpendicular distance between two sense wires in the same plane.

The last drift chamber (D4) had three sense planes in the standard order of U, X and V. This chamber was very large with an active area of about 13.3m^2. Instead of a HV cathode plane of wires as in the other 10 drift chamber assemblies D4 used a grounded aluminum sheet while the sense wires were capacitively held at a high positive voltage of about 3000V.

The field wires in the sense planes were held at a small negative voltage of about 200V for field shaping. The orientation and location of the sense wire planes in this chamber are shown in TABLE 3.9.

TABLE 3.9
D4 Sense Wire plane Characteristics

Plane No.	Plane Type	Z-position (cm)	Sense Wire Separation‡(cm)	No. of sense wires
33	D4 U	1738	2.974	128
34	D4 X	1744	3.175	160
35	D4 V	1749	2.974	128

‡ Perpendicular distance between two sense wires in the same plane.

Electronic Readout

The DC system contained a total of 6288 sense wires. The signals on these wires were amplified and discriminated at the chamber by LeCroy DC201 amplifier/discriminator chips or Nanomaker N-277C amplifier/discriminator chips (see FIGURE 3.24). Both D1 assemblies, D3-3 and D3-4 used the Nanomaker system while all the other assemblies used the LeCroy chips. The chips were arranged on cards which plugged into the top of the drift chamber assemblies and read out 16 sense wires each. The ECL (Emitter Coupled Logic) signal output was carried to the counting room by twisted wire pair cable where the signal STARTed a clock in a LeCroy 4291 TDC.

Each 4291 module contained 32 channels (two amplifier/discriminator cards) and resided in a CAMAC crate with up to 29 other 4291 modules. The 4291 gain was set by a side panel switch to one nanosecond per count with an absolute accuracy of 1 count.

A double width LeCroy 4298 module occupied the command location of the CAMAC crate containing the 4291s. It received the experimental STOP signal, distributed the STOP to all the 4291 modules in its crate and then instructed them to digitize their data. It then read the digitized times from the 4291 modules and sent the data to a dedicated, Fermilab built,

P4299 module residing in one of the experiment's 7 DA CAMAC crates (see Chapter 3: The E769 Detector: Data Acquisition).

The P4299 replaced the LeCroy 4299 module which was used in the E691 Drift Chamber 4290 system. It accepted the data from the 4298 module, re-formatted it, and then raised a LAM to signal that it was ready to be read out by the Smart Crate Controller (see Chapter 3:

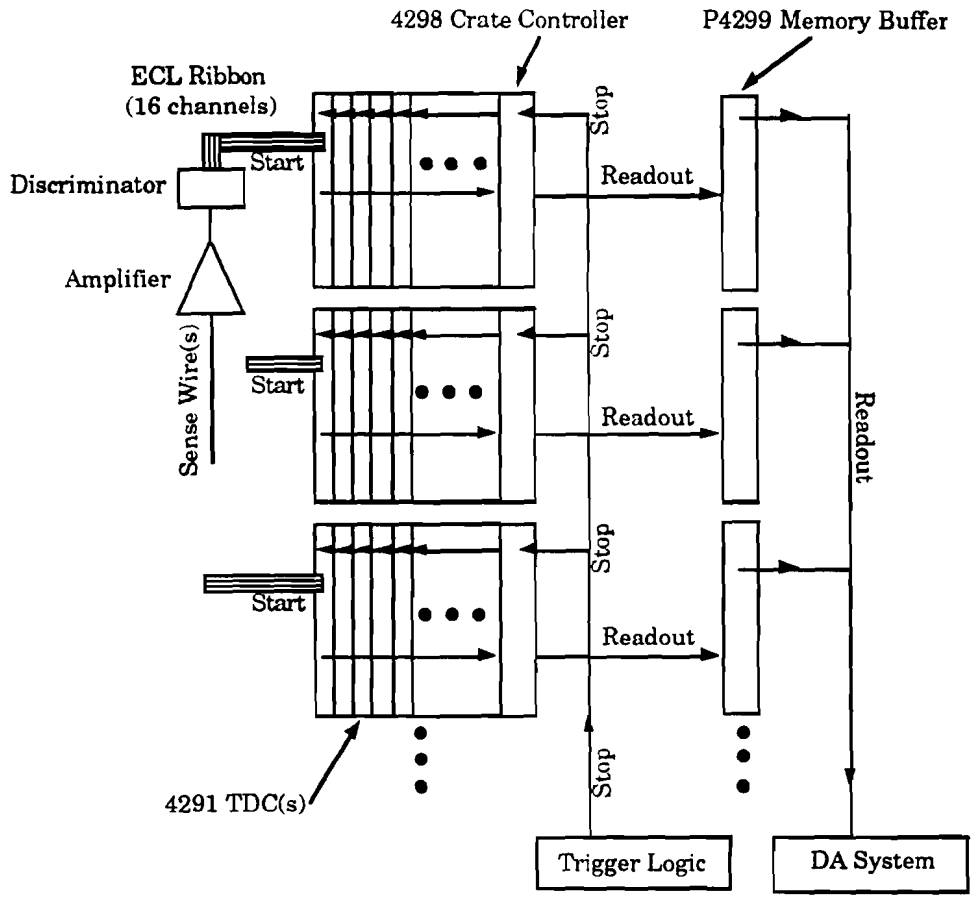

FIGURE 3.24
Schematic View of the Drift Chamber Electronic Readout system

The E769 Detector: Data Acquisition). Since each 4298 had its own P4299 the parallel readout of this system was much faster than the serial readout system used by E691.

The DC 4290 system worked in COMMON STOP mode. In this mode the signal from the sense wire STARTed the clock while the experimental trigger sent the STOP signal to the TDC (see FIGURE 3.25). The longest TDC times were due to hits which occured at the

sense wire. The returned TDC time was the time between the *latest* START and the STOP signal. This effect could be important in high rate environments where more than one particle has a high probability of passing through the same drift cell.

Calibration and On-line Monitoring

The performance of the DC system was monitored continuously during runs using the on-line DAP/CDP processes described later (see Chapter 3: The E769 Detector: ON-Line monitoring). In particular, the on-line routines monitored the structure of the data going to tape, the clustering effects within chambers, the number of triplets (three sense wire matches) per chamber, the number of hot and dead wires, and the plane hit profiles and time distributions. This Drift Chamber DAP would send alarm warnings and messages to the Alarm screen at the control console so that the people operating the experiment would not have to concern themselves with constant checks of the DC system.

Another DAP was left continuously running to monitor many of the High and Low Voltage levels (the HV and LV DAPs). In particular, these DAPs monitored all the HV levels on all the drift chambers as well as the discriminator card thresholds for all the planes. Messages would also be sent by these DAPs to the Alarm screen when any of these voltage levels moved outside of prescribed tolerances.

The time returned by an uncalibrated individual TDC channel was given by: $TDC_{uncalibrated} = t_{plane} + t_{wire} + t_{drift}$. The zero time for an entire sense plane of wires was given by t_{plane} It could be adjusted to lie anywhere within the TDC's 512ns timing range by a time-offset side-panel switch on the 4298. Its final value was determined from fits to the data TDC distributions. t_{wire} was due to differences in cable lengths to the discriminator cards for individual channels in a plane as well as electronic timing differences within the TDCs and on the amplifier cards. t_{wire} was automatically calibrated and effectively set to zero by a pulsing system and the programmable features of the 4290 system (an External Auto-Trim - EAT). t_{drift} was just the drift time of the electrons to the sense wire

given by the product of the drift velocity of the electrons (v_{drift}) and the impact parameter of the particles trajectory to the sense wire (d_{impact}). The drift velocity of the electrons within an assembly was approximately constant except near the edges of the cells (near the HV field shaping wires) as described below.

After an EAT the drift time for a given hit was given by $t_{drift} = t_{plane} - TDC_{calibrated}$ and, except for the left/right ambiguity, one can solve for the particles distance from the sense wire. A representative t_{drift} distribution is shown in FIGURE 3.25. If v_{drift} were constant across the entire drift cell the TDC time distribution would be a perfect box with a width of $v_{drift} \times$ (cell size). A non-constant drift velocity produces the ragged upper edge of the box seen in the figure.

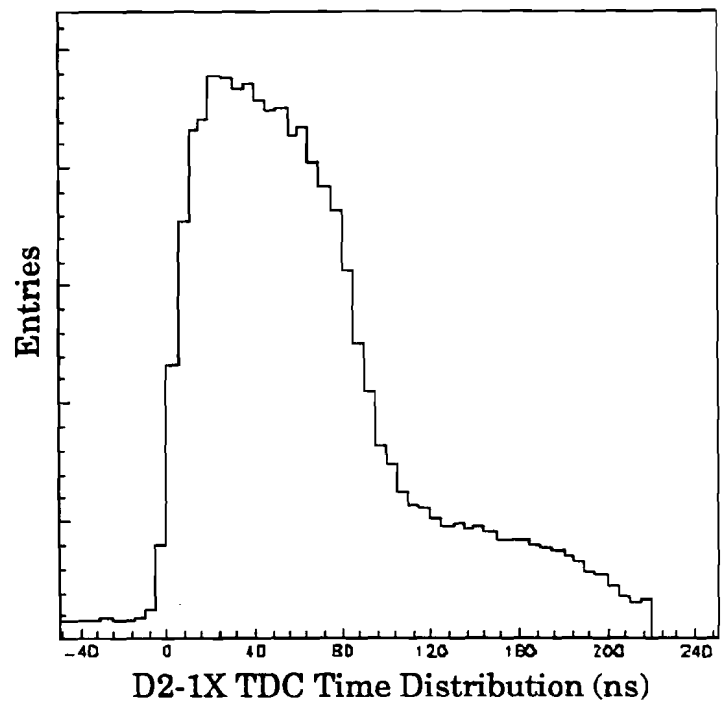

FIGURE 3.25
Drift Chamber TDC time distribution with EAT

Off-line Analysis, Alignment and Performance

The alignment constants (x, y, θ_x, θ_y), drift velocities (v_{drift}) and t_{plane} for each of the DC assemblies was determined off-line using a series of muon runs. TPL was continuously sprayed with stray muons largely from the PE primary target. Turning off

the E769 analysis magnets and using the 'DC paddle counters', a pair of ~0.25m^2 scintillators separated by about 1m located on a movable platform behind the muon wall, to trigger the experiment provided a large sample of straight tracks through the DC system.

Each of the muon tracks was fit to a straight line and

$$\chi^2 = \sum_{i}^{\text{tracks}} \sum_{m}^{\text{planes}} \omega_m r_{im}^2$$

was minimized for the tracks in a muon run (typically one tape of data). The plane resolution is given by $(\omega_m)^{-1/2}$ while the plane residual (r_{im}) is the difference between the fitted location of the particles trajectory at the plane and the predicted location which is a function of the v_{drift}, t_{plane} and the offset for the plane. The minimization procedure for χ^2 was repeated using the updated calibration constants and a narrower road for the track hit selection (which may change the left/right hit choice for a wire) until the narrowest possible road for the track selection was obtained.

In practice, a non-constant drift velocity decreased the residual in the D3 and D4 planes and increased the number of tracks found in the analysis routines. The velocity was parameterized by:

$$v(d) = v_{drift} \qquad d < D$$

$$v(d) = v_{drift} - (v_{drift} - v_{edge})\frac{d - D}{D - W} \qquad D \le d \le W$$

where v_{drift} is clearly a constant drift velocity out to a distance D from the sense wire. From D out to the edge of the cell (W) the drift velocity changes linearly to its value at the edge of the cell (v_{edge}). The effect of the velocity correction on the track residual can be seen in FIGURE 3.26. The residual is defined as the difference between the location of the track as observed by a single chamber and the predicted location of the track as extrapolated from a fit to the track using all the other chambers. It is obvious from this figure that the velocity correction reduces the residual at the edges of a drift cell.

The final measured DC plane efficiencies and resolutions for all reconstructed tracks in the data on one tape are shown in TABLE 3.10. The single track efficiency of the chambers is about 5% higher than what is quoted in this table while the single track resolution of the chambers is ~250μm.

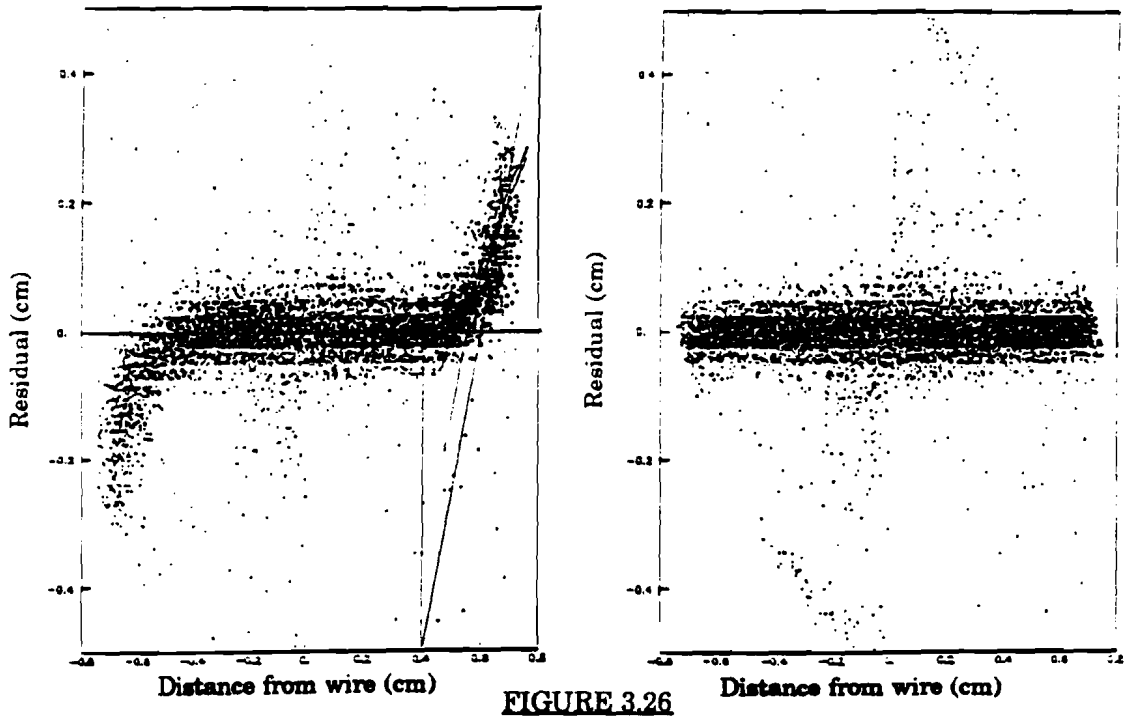

FIGURE 3.26
The effect of the DC velocity correction on DC residuals
a) DC residuals without the velocity correction and
b) DC residual with the velocity correction

The high rate through, and age of, the Drift Chambers caused a 'hole', an area of reduced efficiency, to appear in the central region of most of the DC planes. Most of the aging effect probably occured in the first few weeks of the run and the reduced efficiency has been shown to be rate dependent. FIGURE 3.27 shows the affect of the hole on a DC profile distribution. The holes are only visible in DC profiles for thin slices in the X and Y direction centred on the beam

The shape of the hole has been parameterized for modelling in the E769 Monte Carlo (MC) (see Chapter 5: The E769 Monte Carlo) using two gaussians: the first represents the

distribution of particles across the DC and the other negative gaussian represents the affect of the DC hole.

TABLE 3.10
Drift Chamber Measured Plane Efficiencies and Resolutions

DC Plane #	DC Plane Type	Plane Efficiency	Plane Resolution (μm)
1	D1-1U	0.925	390
2	D1-1V	0.925	380
3	D1-1X	0.910	390
4	D1-1X′	0.908	390
5	D1-2U	0.918	440
6	D1-2V	0.927	400
7	D1-2X	0.890	450
8	D1-2X′	0.854	430
9	D2-1U	0.828	340
10	D2-1X	0.874	310
11	D2-1V	0.899	350
12	D2-2U	0.831	370
13	D2-2X	0.782	350
14	D2-2V	0.776	360
15	D2-3U	0.799	370
16	D2-3X	0.850	350
17	D2-3V	0.826	380
18	D2-4U	0.906	330
19	D2-4X	0.879	350
20	D2-4V	0.916	350
21	D3-1U	0.872	310
22	D3-1X	0.869	330
23	D3-1V	0.876	320
24	D3-2U	0.890	300
25	D3-2X	0.886	290
26	D3-2V	0.862	300
27	D3-3U	0.765	360
28	D3-3X	0.887	360
29	D3-3V	0.906	410
30	D3-4U	0.924	280
31	D3-4X	0.864	280
32	D3-4V	0.900	330
33	D4U	0.701	1190
34	D4X	0.681	1220
35	D4V	0.684	1180

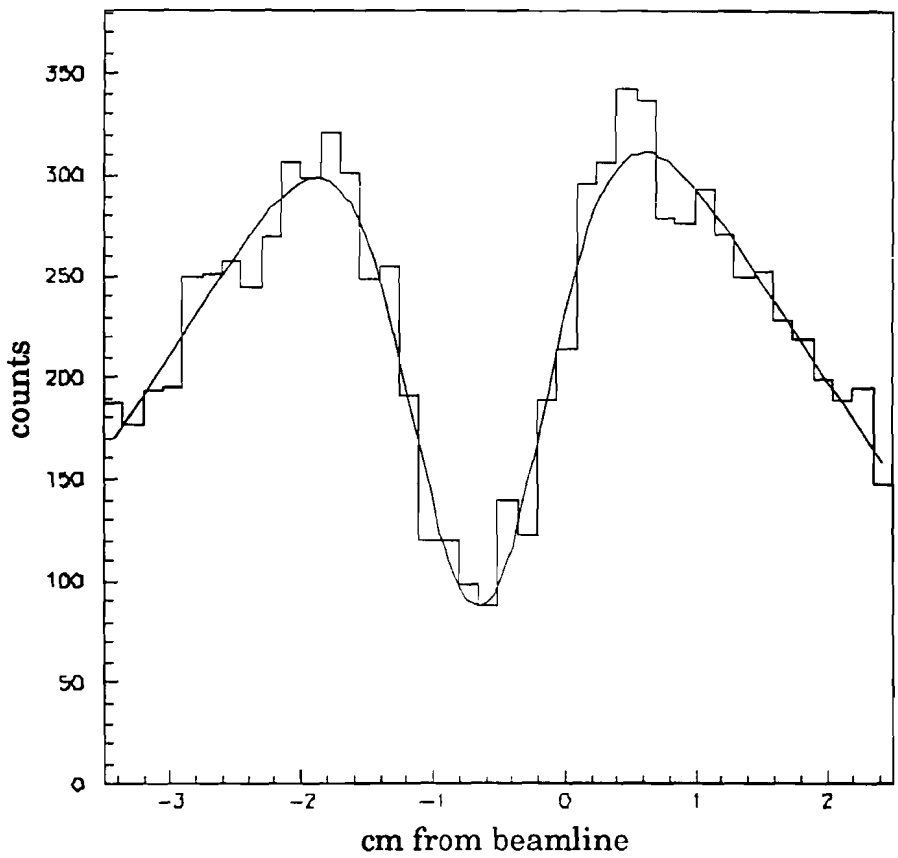

FIGURE 3.27
D1-1X hole.

The fitted hole widths and locations are shown in TABLE 3.11 for both positive and negative beam data. The values in this table represent averages over fitted hole parameters for many runs. The standard deviation of the values is typically ~50-75% of the average. A single hole parameterization was used for every plane within a DC

TABLE 3.11
Parameters of the DC holes in both Positive and Negative beam

Chamber	x_{centre} (cm) -(+)	y_{centre} (cm) -(+)	σ_x (cm) -(+)	σ_y (cm) -(+)
D1	-0.019 (0.19)	-0.064 (-0.69)	0.50 (0.35)	0.53 (0.38)
D2	-0.88 (0.77)	-0.17 (-0.60)	1.3 (0.96)	0.85 (0.60)
D3	-2.6 (-2.7)	-0.53 (-0.49)	4.2 (3.3)	1.9 (1.5)
D4	-6.3 (1.0)	-0.08 (-0.054)	10.4 (7.6)	5.1 (3.1)

assembly since the parameters for the hole did not change significantly within one assembly. The hole was larger for downstream chambers since the magnets and the p_T in the interaction tend to spread the beam outwards. The hole was bigger in the x-direction than the y-direction since the magnets generated their momentum kick in the x-direction. The hole has been shown to decrease our acceptance for high x_F and low p_T^2 particles.

The Analysis magnets

E769 used two large aperture magnets in tandem with the Drift Chamber system for momentum analysis. The first magnet (M1) operated at 2500A while the second magnet (M2) was set at 1800A. The p_T kick of each magnet was ~212.4MeV/c and ~320.7MeV/c respectively.

The magnetic field of each assembly was measured using a Zip-track apparatus before E516. These field parameters were incorporated into the analysis routines for 'swimming' the particles through the magnets during track reconstruction. The fields were constantly monitored throughout the run using hall probes (one per magnet) fixed inside the magnet's aperture.

Cerenkov Counters

Physical Characteristics

The two E769 threshold gas Cerenkov counters were inherited in almost their original state from E691 which in turn had inherited the detectors from E516. The large, downstream Cerenkov counters had been designed to accept and identify the non-leptonic decay products of charmed particles (mostly π, K, and p). Detailed accounts of the design and construction of the detectors can be found elsewhere.[37] Most of the information presented in this section was derived from this source.

---

37 Bartlett et al, NIM, A260(1987), 55-75.

The first and smaller Cerenkov counter (C1) was located inside of and after M2 while the second Cerenkov counter (C2) was placed after D3 (see FIGUREs 3.1 and 3.2). Both C1 and C2 were threshold Cerenkov counters where the different gas mixtures within the Cerenkov volume were chosen to provide maximum discrimination for the momentum range covered by the decay products of charmed particles.

C1 was filled with pure N_2 while C2 was filled with a mixture of 80% He and 20% N_2 yielding values of x=n-1 (where n is the index of refraction of the mixture) of about 350×10^{-6} and 88×10^{-6} respectively. Both Cerenkov gas mixtures were held at normal air pressure. Recall that the Cerenkov angle (θ_c) is given by $\cos\theta_c=(\beta n)^{-1}$ which is only defined for $(\beta n)^{-1}\leq 1$. The threshold momentum (p_{th}) at which a particle of mass m begins to emit Cerenkov light is then given by:

$$p_{th} = \frac{m}{\sqrt{x^2+2x}} \approx \frac{m}{\sqrt{2x}}$$

The threshold momentum for π, K and p in C1 and C2 are shown in TABLE 3.12. The two counters in tandem provide a method of particle identification (ID) in the range from about 5 to 71 GeV.

TABLE 3.12
E769 Cerenkov Counter Thresholds

Particle Type	C1 Momentum Threshold (GeV)	C2 Momentum Threshold (GeV)
π	5.35	10.5
K	18.7	37.2
p	35.5	70.7
e	0.0193	0.0385
μ	4.01	7.99

The Cerenkov light followed the light path shown schematically in FIGURE 3.28. The light paths have been bent in this peculiar fashion in order to place the phototubes in a convenient location and displace them from the fringe magnetic field of M2. The 5" diameter, RCA8854 phototube faces were located at the exit aperture of a Winston-cone

assembly which increased the light acceptance into the phototube. These cones were designed to pass light to the phototube as long as the light was incident at <20° to the symmetry axis of the cone/phototube assembly. To protect the C2 PMTs from the He gas mixture in the radiator volume, the faces of these phototubes were shielded from the C2 gas by a fused quartz window, and the volume between the phototube face and the window was continuously flushed with N_2.

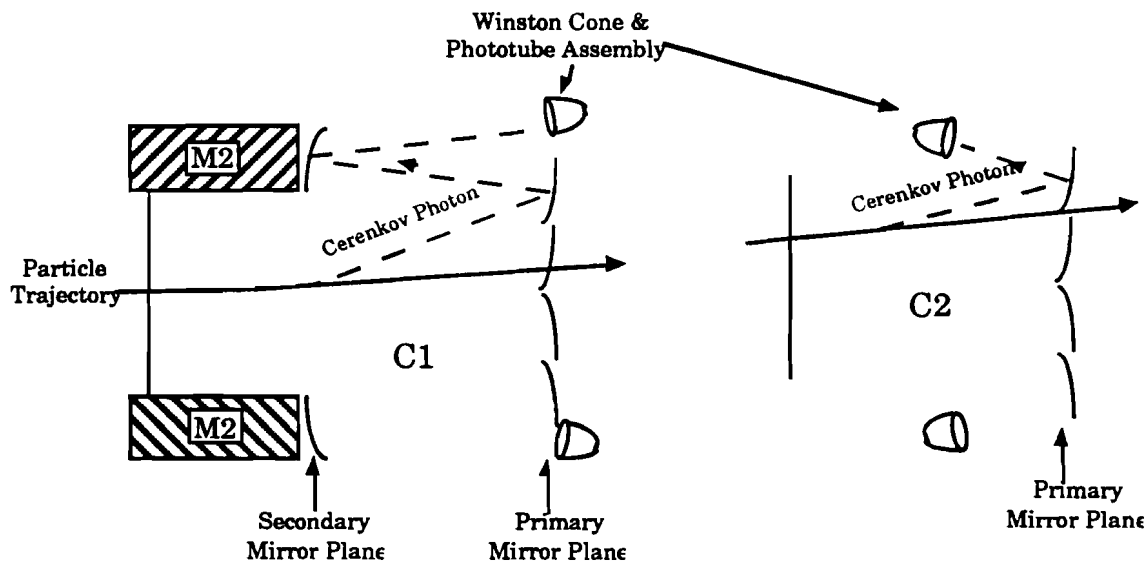

FIGURE 3.28
C1 and C2 Light paths

The large phototube faces were coated with an ~400Å thick layer of p-terphenyl (pTP) which shifted the wavelength of the incident Cerenkov light (1600 to 2500Å) to a wavelength region where the PMTs were sensitive (3500 to 5000Å). The coating was followed by an ~100Å thick layer of magnesium flouride which prevented evaporation of the pTP layer. The faces of the phototubes were kept at ground voltage and the last dynodes were kept at a high positive voltage of about 3000V. This configuration resulted in high gain and linear performance of the phototubes allowing detection of individual photons.

Despite the efforts to shield the PMTs from the effects of the fringe fields of M2 some of the PMTs in C1 were rendered useless by the effect of the fields. To compensate for the

fringe fields, a *bucking field* was produced in the PMTs by wrapping ~100 turns of wire around each of the C1 PMT assemblies and passing about 4A through the coils.

The PMT signals were digitized by LeCroy 2249 ADCs. The PMTs were calibrated using laser light signals carried by optical fibres to the face of the PMT. The intensity of the laser signal at each PMT could be adjusted using a neutral density light filter at the laser to produce about one photo-electron (PE) per phototube on average. The ADCs were set to generate roughly 20 counts per PE and were constantly monitored to ensure that their pedestals were greater than zero.

Cerenkov Performance and Data Analysis

The performance of the C2 counter was intimately linked to the He/N_2 mixture since $p_{th} \sim m(2x)^{-1/2}$ and x depended on the He/N_2 ratio (f). E769 used a Sonic Wave Monitor[38] (SWM) system designed and built at FNAL to determine the ratio. Using the SWM we have found that all the four-day averaged values were in the approximate range $0.185<f<0.230$. Most of the values were in the tighter range from about 0.20 to 0.22. Since $\Delta p_{th}/p_{th} = \Delta x/2x$, this corresponds to a change in the threshold momentum of about 5%. A single set of average threshold momenta determined from the data were used in reconstruction.

For a particular DC track with calculated momentum p, the particle identification code determined the number of photo-electrons detected at a PMT, predicted the number of photo-electrons *expected* at the PMT due to particles of momentum p but different masses, and used this information to determine the probability that the particle was of a given type (mass).

38 H. Fenker, E769 internal memo, C2 Gas Mixture Monitoring during E769.

The probability for each particle type was calculated for each Cerenkov counter (P_{C1} and P_{C2}). The final probability, incorporating the information from both counters and the *a priori* probability for each particle type A_i, is given by:

$$P_{final} = P_{C1} \times P_{C2} \times A_i$$

and then requiring $$\sum_{i=1}^{5} P_{final} = 1$$

The *a priori* probabilities are typical probabilities for particles produced in hadronic interactions. The *a priori* probabilities for each of the five particles listed in TABLE 3.13 are: e=.01, μ=.01, π=.84, K=.12, p=.04.

Cerenkov Kaon Efficiency

The Cerenkov kaon efficiency was determined as a function of the momentum of the kaon using $\phi \rightarrow K^+K^-$ decays. One of the two kaons was required to have a Cerenkov probability of >0.7 while no cut was placed on the other kaon. The efficiency was calculated by comparing the fitted number of ϕ in this signal for a given momentum range of the untagged kaon with a fit to the signal using the additional requirement that the Cerenkov probability of the originally untagged kaon be >0.13 (just above the *a priori* probability). Two such histograms are shown in FIGURE 3.29. The fitted mass of the ϕ is 1019.72±0.07MeV.

The momentum ranges were chosen to cover interesting Cerenkov light momentum thresholds in the detectors, and so the size of the signal in each range would be roughly equal. The efficiency as a function of momentum calculated in this way is shown in

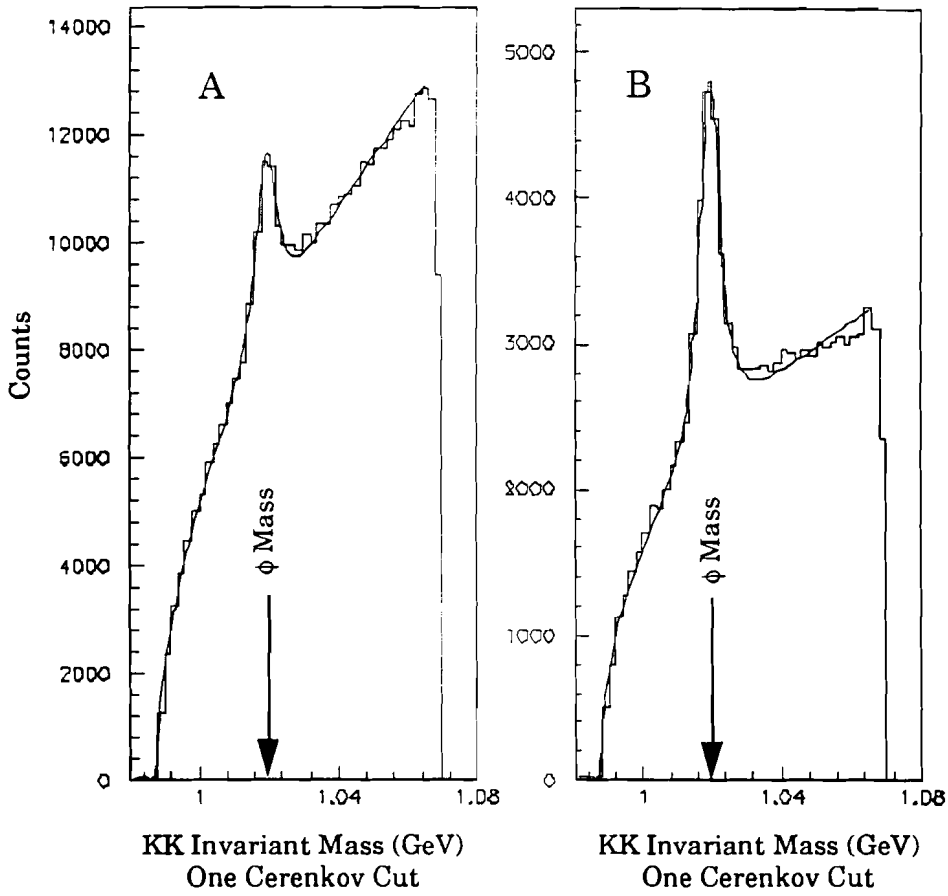

FIGURE 3.29
Example of plots used in Cerenkov Kaon efficiency Analysis
$\phi \rightarrow K^+K^-$ for A) one kaon probability >0.7 and
B) one kaon probability >0.7 and another >0.13

FIGURE 3.30. The efficiency (ε) and error ($\Delta\varepsilon$) on the efficiency were calculated as[39]:

$$\varepsilon = \frac{N_2}{N_1}$$

$$\Delta\varepsilon^2 = \frac{(1-2\varepsilon)\Delta N_2^2 + \varepsilon^2 \Delta N_1^2 + \varepsilon(1-\varepsilon)N_1}{N_1^2}$$

where N_1 and N_2 are the number of entries in the ϕ signal before and after the second Cerenkov cut respectively. In each case the ϕ signal was fit with a Breit-Wigner while the background was fit to a function of the form $A(m-m_{2K})^n$ for $m>m_{2K}$ and equal to 0 for

39 Zhongxin Wu, Error Analysis for Correlated Data Samples, January 8, 1991, E769 Internal Memo.

$m<m_{2K}$. A is the normalization for the background term, m is the mass at which the background is being evaluated, m_{2K} is twice the kaon mass and n is the power for the background shape. Also shown in FIGURE 3.30 is the kaon efficiency using the experiment's $D^+ \rightarrow K^-\pi^+\pi^+$ signal and the efficiency calculated from MC generated minimum bias events containing ϕ mesons.

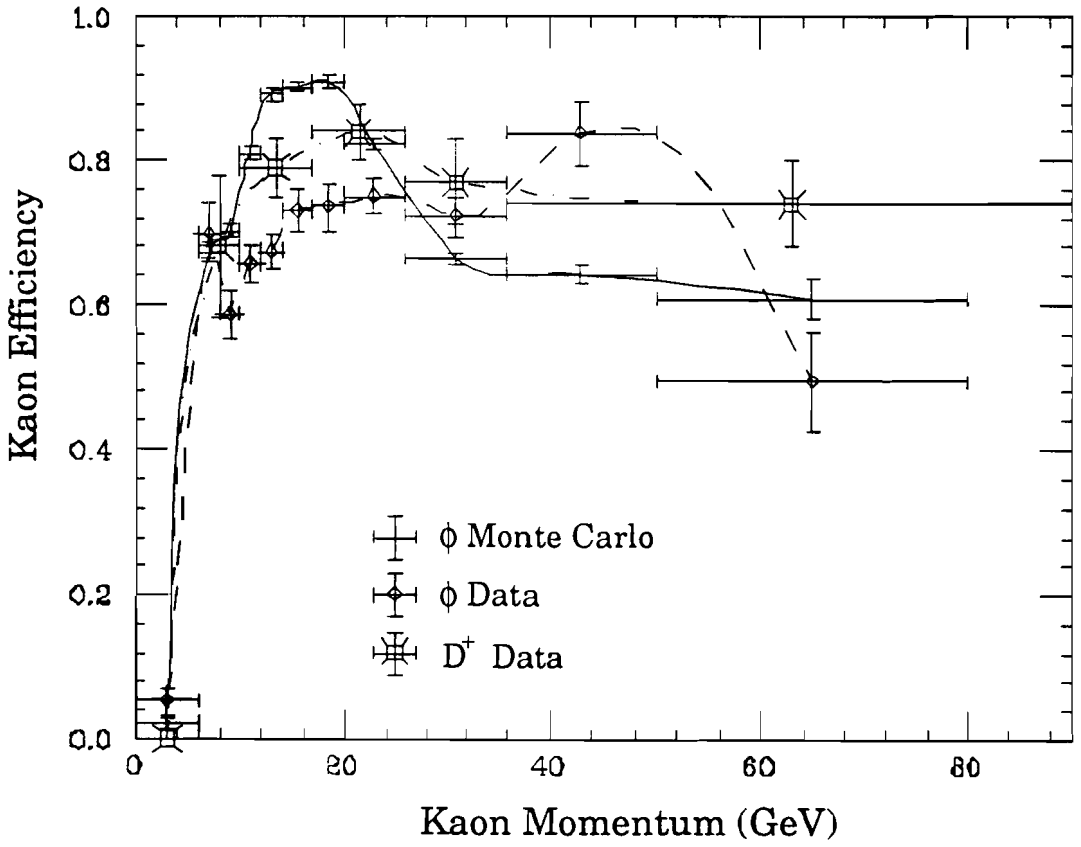

FIGURE 3.30
Cerenkov Kaon Efficiency calculated from data

Electromagnetic Calorimetry

The Segmented Liquid Ionization Calorimeter (SLIC) was used in determining the energy of particles which interacted predominantly through the electromagnetic interaction. Along with the Hadronic Calorimeter it also provided the main trigger for the experiment. A small prototype for this large detector was developed and tested in the mid-

1970s and is described in detail elsewhere.[40] The full scale detector was first used in E516. Its construction, operation and the algorithm used to reconstruct the particle showers are described in other references.[41,42] Most of the information in this section is derived from these sources.

SLIC Construction

The SLIC had an active area of about 2.44m × 4.88m. It was broken into 60 layers in the beam direction, each layer comprising a third of a radiation length. Each layer was used for measuring the position of a shower in one of three directions: U, V and Y, where the U and V planes were inclined at ±20.5° to the vertical respectively (the same system used in the Drift Chambers) and the Y-planes determined the vertical location of the shower. A beam particle passed through 20 of the UVY plane combinations before leaving the SLIC.

Each layer of the SLIC (except for a slightly different configuration of the first and last planes) consisted of a radiator-scintillator pair. The radiator was an Al-Pb-Al laminate with a total thickness of about 0.37cm. The laminates were as large as the full area of the SLIC and the aluminum sheets were folded around the edges of the lead sheets to shield the scintillator oil from the lead. Each of the laminates was covered with a ~0.0025cm thick teflon film.

The scintillator layers were formed from large, corrugated, ~0.0508cm thick aluminum sheets. The corrugations, which formed the U, V and Y channels of the detector, had a square-wave cross section forming channels about 3.17cm wide and 1.27cm thick. Each side of the aluminum sheet was entirely covered with teflon film so that when the radiator-scintillator-radiator unit was assembled, channels were formed which had an

40 V.K. Bharadwaj et al., NIM 155 (1978) 411.
41 V.K. Bharadwaj et al., NIM 228 (1985) 283.
42 D.J. Summers, NIM 228 (1985) 290.

interior surface which was entirely coated with teflon. This structure is shown in FIGURE 3.31.

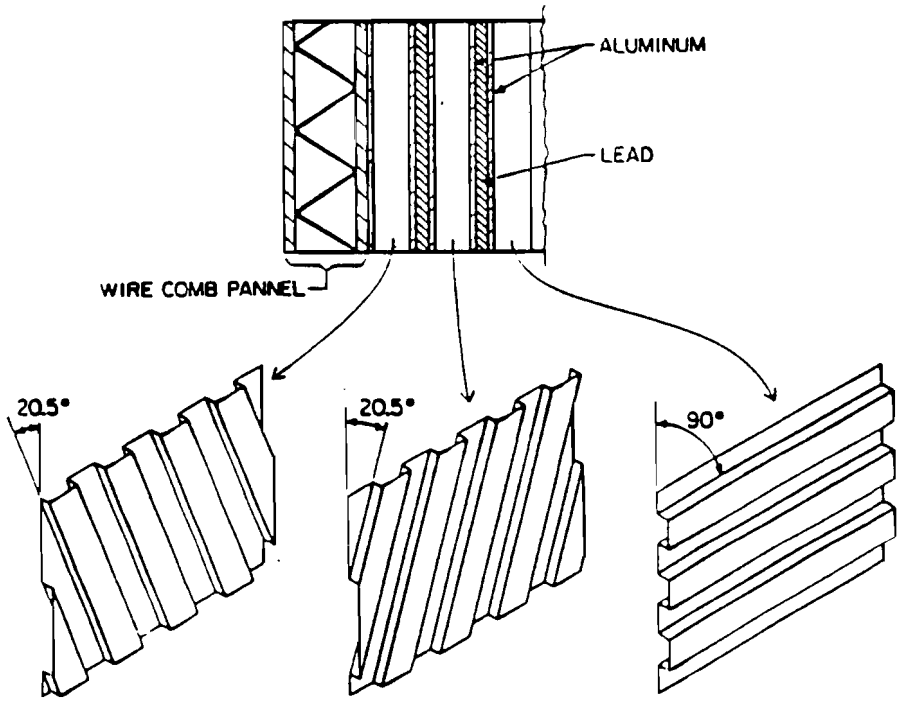

FIGURE 3.31
SLIC radiator-scintillator assembly

The scintillating medium was NE235A, a mineral-oil based liquid scintillator. It had an index of refraction which was greater than that of the teflon film so that each teflon-coated channel formed a light-pipe in which some of the scintillating light suffered total internal reflection. One end of each channel was terminated by a 90° mirror with a reflectivity of about 80%. They reflected light travelling towards them back to a wavebar on the other side of the channel.

All channels with the same orientation and distance from the beamline fed their light into the same wavebar. The wavebars were a lucite-type material doped with 90mg/l of the chemical BBQ. The BBQ shifted the wavelength of the scintillating light from the blue to the green where the phototubes were more efficient. In the central region of the SLIC, where particle multiplicity was high, each wavebar was connected to a single RCA 4902 phototube while in the outer regions pairs of wavebars were connected to a single RCA 4900 phototube.

In each case, the phototubes were mounted at an angle of 75° to the wavebar to increase the effective quantum efficiency of the phototube.

SLIC Readout and Calibration

Each of the SLIC phototubes was assigned to one channel of a 12-bit LeCroy 2285A ADC system. In this ADC system the signal ground was isolated from the high voltage ground of the phototube by 500Ω. The signal cable was also wound through many turns of a Ferrite toroidal coil. These two precautions managed to reduce the r.m.s. pedestal width for each ADC channel, a measure of intrinsic noise in the system, to typically <1 count.

The day to day calibration of the SLIC system was maintained through the same N_2-laser light system as was used for the threshold Cerenkov Counters. The laser sent 1 Hz light pulses to each of the SLIC phototubes through an optical fiber distribution system. This system was useful for determining system linearity, setting up the SLIC and correcting PMT gains. The overall energy calibration of the SLIC was determined by studying the signals from minimum ionizing muons traversing the SLIC.

Hadronic Calorimetry

Hadronic Calorimetry in E769 was obtained through use of information from the SLIC and the Hadrometer. A simple schematic view of the Hadrometer is shown in FIGURE 3.32. A full description of the Hadrometer can be found elsewhere.[43] Most of the information in this summary of the detector was derived from this reference.

The Hadrometer was about 2.7m high, 4.9m wide and formed of 36 radiator-scintillator assemblies. The first 18 assemblies were grouped together and referred to as the upstream Hadrometer while the last 18 assemblies formed the downstream Hadrometer. The radiators were ~2.5cm thick steel plate which had the same dimension as the entire

43 J.A. Appel et al., NIM A243 (1986) 361.

detector. The scintillator was polymethyl methacrylate acrylic doped with 1% napthalene, 1% PPO (2,5-Diphenyl-oxazole) and 0.01% POPOP ((1,4-di-(2-15-phenyl-oxazolyl))benzene).

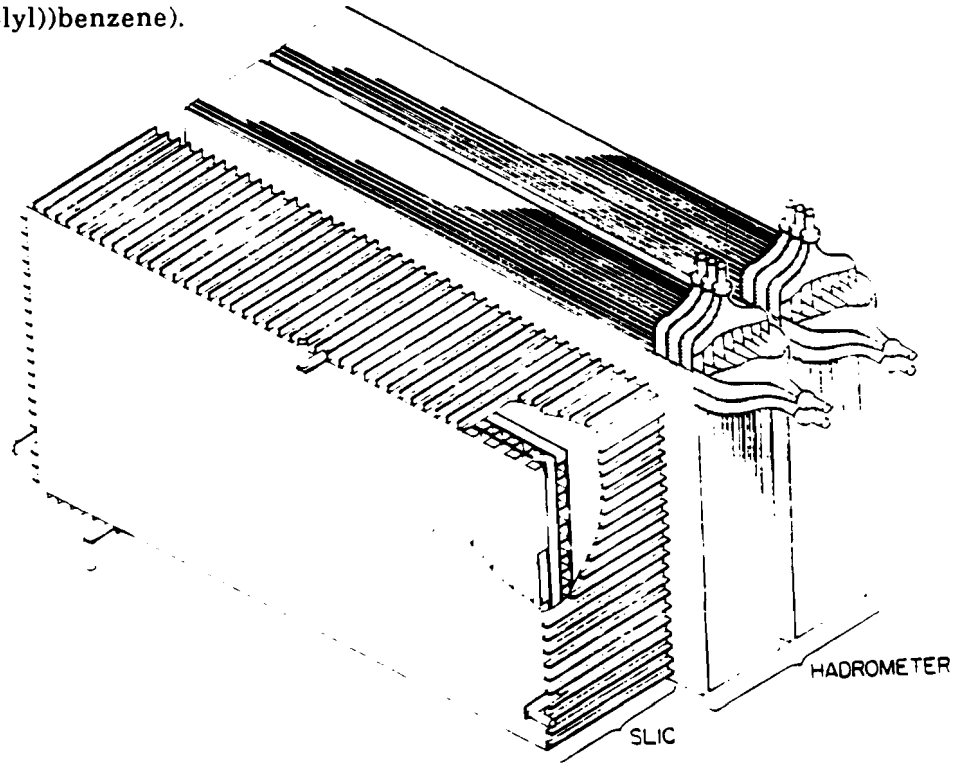

FIGURE 3.32
Schematic of the Hadrometer

The scintillator strips were ~14.3cm wide and 1cm±25% thick. In the upstream hadrometer the first scintillator plane was formed of vertical strips and the following scintillator planes alternated between horizontal and vertical strips. FIGURE 3.32 shows that the light from the first nine vertical strips was collected together through undoped acrylic (Type G) light guides as were the first nine horizontal strips. This sequence was repeated in the downstream Hadrometer.

The light guides end at EMI 9791KB phototubes. The phototubes were read out by the LeCroy 2285A ADC system in exactly the same manner as the SLIC. The Hadrometer ADC system also used coaxial input cable which was wrapped around Ferrite cores and the

signal ground was isolated from the HV ground by a 1kΩ resistor. The ADC signal integration time was 165ns for the SLIC and 250ns for the Hadrometer.

Hadrometer Calibration and Performance

The relative calibration of the 142 Hadrometer phototubes was accomplished using the minimum ionizing particle results from a series of muon runs strewn throughout the run.

The final values for hadronic energy deposition were obtained by treating the SLIC and Hadrometer as a single unit. Slightly more than half of all hadrons deposit more than minimum ionization energy in the SLIC. About 88% of the total hadronic energy in an event was deposited in the SLIC/Hadrometer combination. The final energy resolution was given by $\sigma_E(E)^{-1} \sim 75\%\ E^{-1/2}$.

The E769 Trigger System

E769 used five triggers: Interaction, E_T(standard), E_T(kaon), E_T(high) and Electron. All the triggers except the Interaction trigger were intended to enhance the fraction of charm-containing events written to tape. These triggers are discussed in this section.

The Interaction Trigger

The Interaction Trigger was a minimum bias trigger requiring a beam particle with no halo and a signal of ~5× minimum ionizing in the interaction counter. The trigger had an efficiency of close to 100% for high multiplicity charm events. Since the segmented target was ~2% (for protons) of an interaction length roughly every fiftieth particle interacted in the target. At a beam rate of 1 MHz the raw interaction rate would be 20KHz - much higher than the Data Acquisition System's event rate capability of about 500Hz and entirely swamping the relatively rare charm events. The trigger rate was therefore pre-scaled by factors from 100 to 500 in order to reduce the rate of writing Interaction triggers to tape but sufficient for providing the experiment with a sizable set of minimum bias events. The final set of Interaction data comprises about 6% of the total data set and it is anticipated that this large data sample (6% of 400×10^6 events) will be used for high statistics studies of Λ production at low x_F, the A-dependence of ϕ meson production, as well as other interesting studies.

The E_T(standard) Trigger

The E_T(standard) trigger was intended to be the main trigger of the experiment. It was identical to E691's trigger of the same name. The basic objective of the trigger was to make use of the higher transverse energy (E_T) of the charm quark interactions relative to minimum bias events containing only the lighter quarks.

The trigger was implemented by weighting the signals from the SLIC and Hadrometer in order to favour events with high transverse energy. The weights increased linearly

with distance away from the beam line as shown in FIGURE 3.33. The lines in the figure correspond to the weights for the X planes of each calorimeter. The weights in the other views are identical to the weights in the X plane. The weighted calorimeter energies were summed and integrated over the 200ns E_T gate and required to pass a threshold cut before producing the E_T trigger. The E_T(standard) threshold varied between about 5 and 6 GeV during the run.

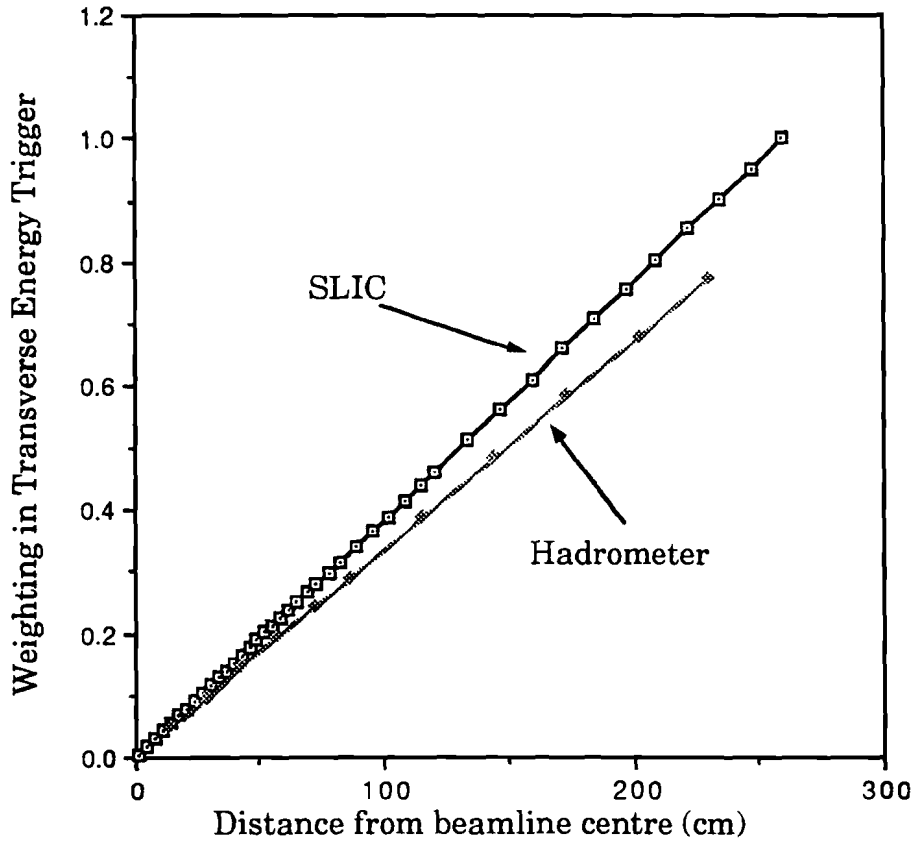

FIGURE 3.33
Weighting Scheme for the E_T trigger

Starting at run 1772 the E_T trigger required that a special 'Killer Bit' (KB) be OFF (see APPENDIX A). The KB was implemented for the TRD to eliminate events on tape which contained one or more beam particles in nearby buckets. It was also used for the E_T trigger because if two (or more) interactions occured within the target during the gate time of the E_T

trigger then some fraction of the E_T from those successive events would be added to the E_T of the first interaction. This would increase the probability that the event be written to tape in an undesired manner. The KB was ON whenever a beam particle was detected in any bucket within ±150ns of an interacting particle. The KB was not sensitive to multiple particle bucket occupancy in the same bucket as the interacting particle.

The E_T trigger had a rejection of about 3 and was prescaled by factors ranging from 5 to 60. The E_T(stnd) triggers were prescaled in order to maximize the number of E_T(kaon) triggers. The prescaler setting was changed in order to maximize the event rate to tape. By comparing the yield of $D^{\pm}$ in the set of Interaction triggers to the yield of $D^{\pm}$ in the set of E_T(standard) triggers we have found that this trigger had an enrichment factor of about 1.4 for charm events. By determining the fraction of the D^o and $D^{\pm}$ in the Interaction triggers which also had the E_T(stnd) trigger bit active we found that this trigger had an overall efficiency of about 80±16%.

The E_T(Kaon) Trigger

The E_T(Kaon) trigger was identical to the E_T(standard) trigger except that it required a four fold-coincidence between the eight DISC phototubes and did not require the KB to be OFF. At least one DISC phototube hit was required in each of the four DISC phototube quadrants. Since kaons made up only about 6% of the beam in both negative and positive running conditions, the E_T(Kaon) triggers were not prescaled in order to write as many kaon-nucleon interactions to tape as possible. The final sample of DISC tagged events on tape comprised about 25% of the total number of events written to tape.

The E_T(high) Trigger

The E_T(high) trigger was identical to the E_T(standard) trigger except that it imposed a higher threshold of about 8GeV. It was intended to further enhance the fraction of events on tape containing charm quarks and had a final enhancement over the entire run of about 2.

The E_T(high) triggers were prescaled by factors ranging from 7 to 100. The final sample of E_T(high) triggers was about 16% of the entire data sample.

The ElectonTrigger

The electron trigger was installed during positive data taking to study bottom quark production utilizing the semi-leptonic decays of the B mesons (e.g. $B^{\pm} \rightarrow e\nu_e$+hadrons). It required the E_T(high) trigger as well as a large deposition of energy in the SLIC consistent with an electron signal. No studies have been made to examine the efficiency of this trigger. It accounts for roughly 7% of the data written to tape.

The Data Acquistion System

Components and Operation

The goal of the E769 Data Acquisition system (DA) was to reach a 400 event/s output rate with only 30% dead time. It achieved an event rate of almost 500 event/s with a 30-40% dead time using a parallel architecture, buffered input memory and multiple output tape drives. The system is shown schematically in FIGURE 3.35 and described in detail elswhere.[44]

The first stage in providing a fast DA system occured in the readout of the CAMAC crates where one Smart Crate Controller (SCC) was used per crate for parallel readout of the digitized information. The trigger signal from the fast electronics was sent to each of the seven SCCs which then read the information sequentially from the modules within their respective crates. The order of readout for the CAMAC modules was determined by the speed at which they digitized their data and programmed into a SCC in the form of a progam list known as CALEX (CAmac List EXecutor).

---

44 C. Gay and S. Bracker, IEEE Transactions on Nuclear Science, 34 (1987) p. 870.

The information from each SCC was sent to a dedicated RBUF (a double buffered memory input module) located in a VME crate. The RBUF was the CAMAC-VME interface and the double memory buffer allowed one memory buffer to be read out while the other was being filled with the results of another event.

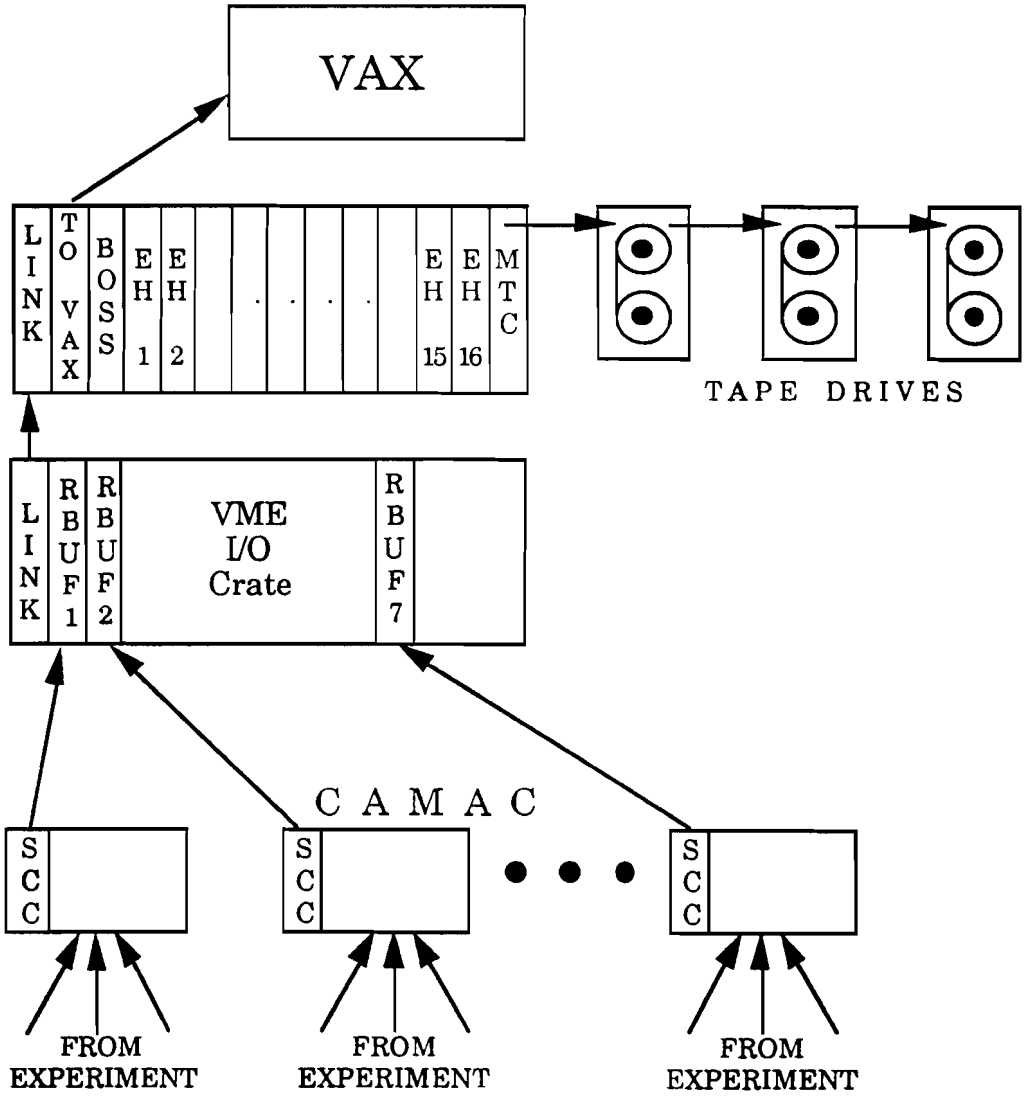

FIGURE 3.34
Schematic of the E769 Data Acquisition System

The event information from each RBUF was read out through a VME crate link by Advanced Computer Project (ACP) parallel processing modules. Seventeen of the ACP modules were used in E769. They were divided into three distinct classes based upon their duty during a spill. Sixteen ACP Event Handlers (EH) were responsible for the retrieval and formatting of the events from the RBUFs. The retrieving and formatting operations were distributed throughout a spill amongst the processors. At any time during the spill two of the ACPs were designated as the Grabbers and were responsible for 'grabbing' the events from the RBUF memories. The other fourteen ACPs were designated as 'Munchers'. Their purpose was to perform event compression and data formatting on the events which they had previously retrieved as Grabbers. The job of deciding which event handlers were to be Grabbers and Munchers, and of ensuring that processed events went to tape and to the VAX, went to the Boss ACP.

FIGURE 3.35 shows that the VAX11/780 had the highest level of control within the DA system (except for the operator). DA system configuration, start and stop commands, pause and resume, abort run, sending events to the on-line event pool and a constant monitoring of all system errors were the responsibility of the VAX and the operator.

E769 Data Format

There were essentially three different types of events written to tape during the run: physics, calibration and scaler events. Physics events were any event satisfying any of the five different triggers. Calibration events were special events used for calibrating different detectors. Calibration events which examined the pedestal levels of the various ADCs in the experiment were taken in sets of five both immediately preceding and following the spill. The same method was used for reading out the ADCs when a phototube laser pulse was sent to the SLIC, Hadrometer and threshold Cerenkov Counters. Other calibration events were taken as a special series of spills for background muons (used in calibrating the SLIC and Hadrometer) and for DC paddle triggers using the background

muons for determining the alignment constants of the DCs. The scaler events were recorded at the end of every spill. They contained the total counts of each scaler used in E769. The Scaler events were important for determining the normalization in the number of incident particles as described in Appendix A. A schematic view of the trigger system with emphasis on the scalers is shown in FIGURE 3.35. A list of the scalers and their definitions are given in TABLE 3.13.

TABLE 3.13
Summary of important Scalers

Scaler	Meaning
Low Level Trigger Scalers	
SEM	Primary Beam Monitor ($\times 10^7$)
BS	Beam Spot scintillator counts
GB	BS • (NO Halo counter pulse)
TRD•GB	GB • (coincidence of two scintillators on either side of TRD)
TGT INT	count in the INT scintillator indicating TarGeT interaction
GB•TGT INT	GB•TGT INT
Trigger Inputs	
KHI	# of DISC 4-fold coincidences w/ at least 1 hit/quadrant
PPI	TRD•GB • (prescaler for non-kaon triggers)
ET STD	E_T(standard) trigger requirement satisfied
INT(PS)	GB•TGT INT • (prescaler for interaction triggers)
ETB(PS)	E_T(beauty) trigger requirement satisfied
PI	TRD•GB • (prescaler for beauty triggers)
ELE	Event satisfied electron trigger requirement
KB	No Beam particle within ±150ns of interaction (only runs > 1773)
Trigger Strobes	
BM STB FI	GB•TGT INT
STB NO BUSY	GB•TGT INT • (DA AND Trigger NOT Busy)
STB B	STB NO BUSY
STB B FO	STB B
Trigger Outputs	
ETK	ET STD • KHI
ETPI	ET STD • PPI • KB
INT	INT(PS) • STB FO
SCC STRB 1	ETK + ETPI + INT
SCC STRB 2	ETB + ELECTRON
ETB	ETB(PS) • PPI • KB
ELECTRON	ETB(PS) • PPI • ELE
SCC STRB	SCC STRB 1 + SCC STRB 2

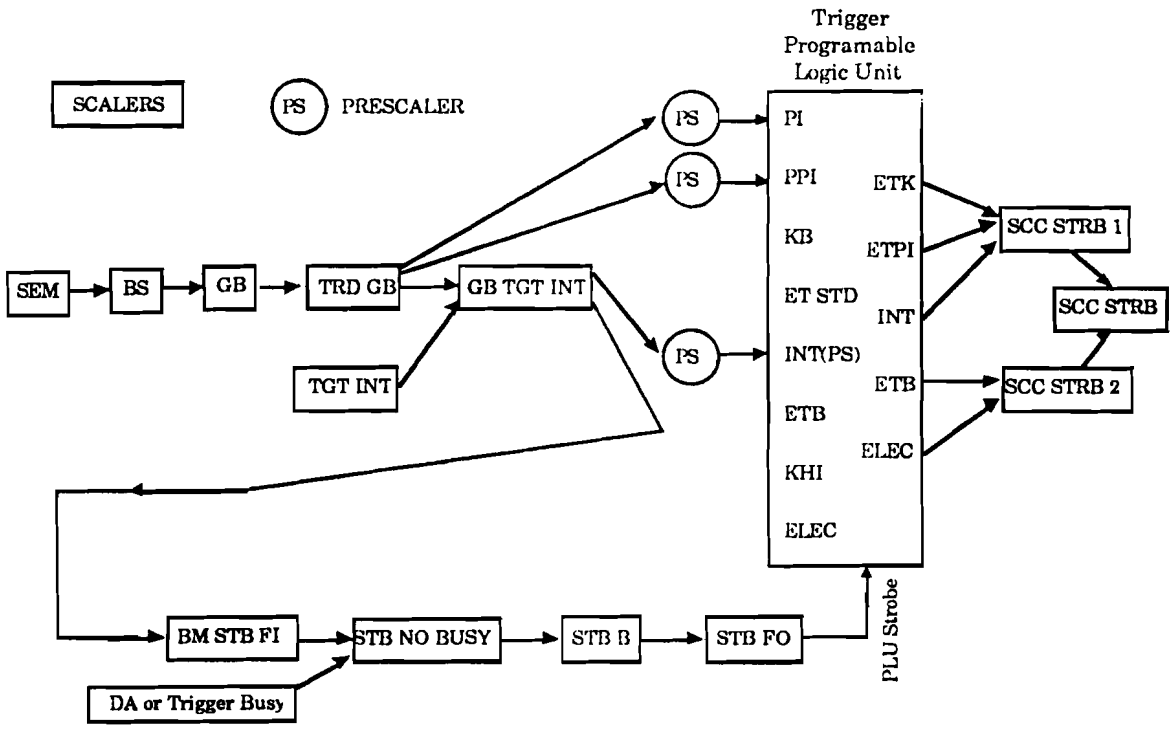

FIGURE 3.35
A simplified/schematic view of the E769 Trigger system

ON-line monitoring

E769 made use of a variety of methods to monitor the progress of the run and the status of its detectors while the experiment was running. The most important on-line systems were the Data Acquisition Process (DAP) and Command Display Process (CDP) systems which allowed the experimenters to monitor the performance of any of the detectors in the spectrometer. This included monitoring all the important High and Low Voltage (HV & LV respectively) levels, all the scalers, and a program which raised warnings and e or messages on a specific terminal when any of the monitored quantities wandered outside acceptable limits of operation. As well as the DAP/CDP package, we used an Intersp. process control package which ran code that accessed the CAMAC crates for calibration purposes during the period between successive beam spills. Two graphics packages, the

General Purpose Interactive Graphics (GPIG) routine and the E769 Event Display (ED) routine, allowed shift personnel a visual presentation of the operation of the detector's components. This section describes the operation of these on-line monitoring packages.

The DAP/CDP system

FIGURE 3.36 shows the operation and flow of information through the Online Monitoring System (OMS). The directions of the arrows represent possible directions for the flow of information between the different parts of the sytem. Raw data from an event could be taken from a data tape, an existing data file or, most commonly, from selected events passed from the DA-ACP system to the VAX. All the scaler and calibration events were automatically passed to the OMS and roughly 2% of all data events were also passed on for immediate analysis.

The events were taken from the desired location and stored in the 'Event Pool' (EP). It was a permanent Global Section of disk space with multiple user read-access. The job of placing events into the EP was handled by a detached process known as the EP Builder (EPB). The EPB was started, monitored and stopped by a user communicating with the EPB through a CDP which, in turn, communicated with the EPB through another permanent Global Section.

Individual DAPs read the events stored in the EP and performed their own analysis on the events. The multitude of allowable DAPs coordinated their access to the EP with the EPB through another permanent Global Section in order to avoid the possibility that the EPB attempts to delete an event while a DAP was reading it.

Users had access to the information accumulated with the DAPs and could control their execution through individually tailored CDPs. The CDPs and DAPs communicated through temporary Global Sections which existed only while the DAP was running. The CDPs might accumulate, histogram, monitor, and/or analyse the information provided by

the DAPs and could send messages to the shift personnel if any aspect of the detector went awry.

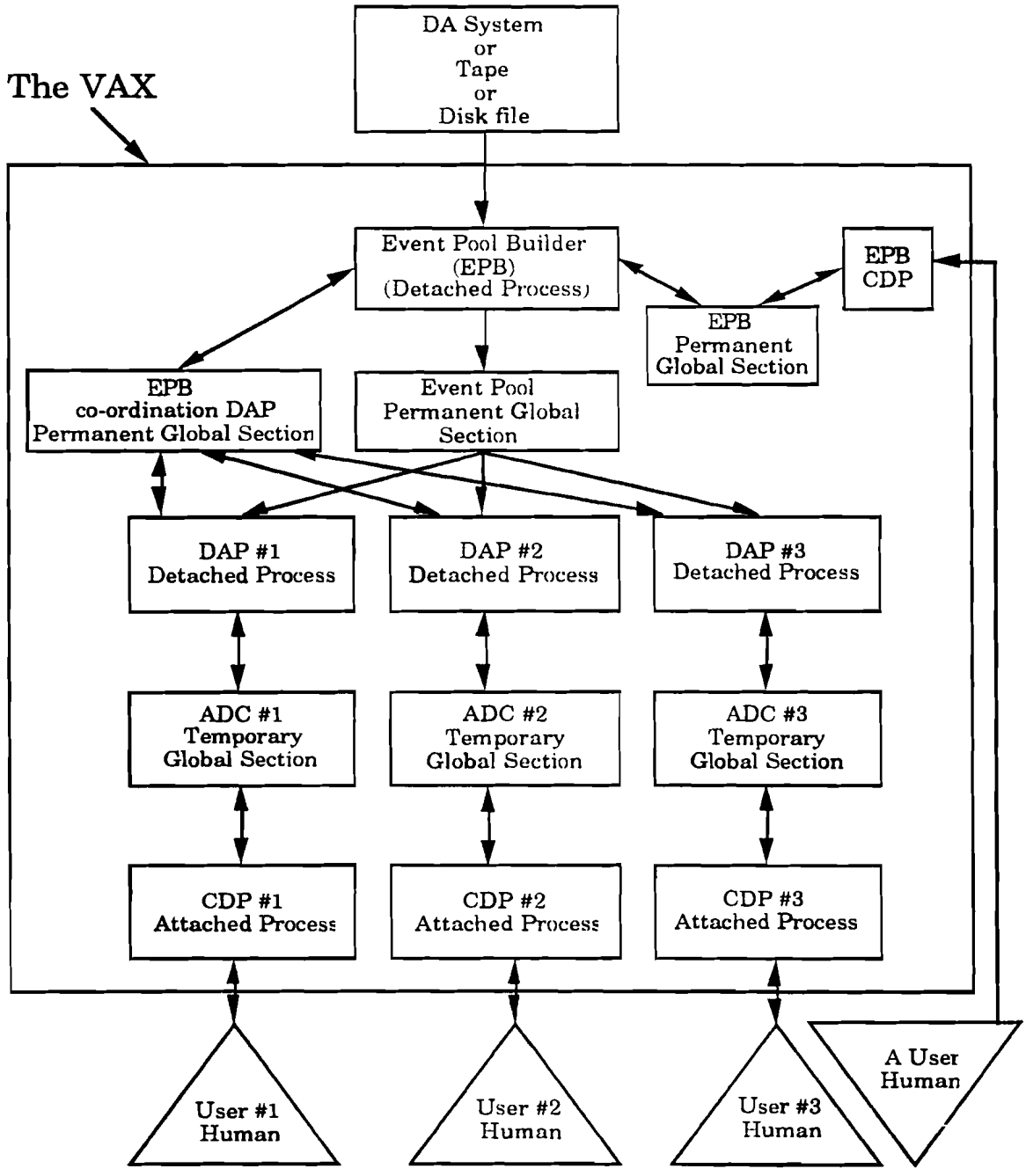

FIGURE 3.36
Basic Configuration of the Online Monitoring System

Two important DAP/CDP processes were the SCALER and LOW Voltage systems which, since they dealt with the operation of all components of the spectrometer instead of one particular detector, are described here. The SCALER program monitored the values and sum of the 212 physical scaler channels (a raw count of some detector's triggers, pulses, etc) recorded in E769. It also allowed the capability of studying 27 software scalers (counters which were a function of some other quantities). The routine displayed a summary of a subset of these 239 scalers including the scaler value for the most recent spill, the accumulated scaler counts since the beginning of the run, and important ratios of these two quantities to other relevant scalers.

The LOW Voltage On-line monitoring process checked the voltage levels provided to the SMD and Drift Chamber systems. HV levels for these two systems were monitored by reducing the HV by a factor of 1000.

All the DAPs could raise warnings and errors to the attention of the shift personnel through the ALARM DAP. The ALARM DAP monitored the messages sent from the other DAPs and displayed the messages as well as sounding a bell when an error was found. This interwoven communication system proved very useful for eliminating problems quickly and efficiently.

The INTERSPILL System

The INTERSPILL system was developed for use in E769 to allow users to have access to the CAMAC data pathways during the time between spills (slightly less than 38 seconds) in order to avoid interference with the DA system's control of the CAMAC system. The system proved useful for calibration and monitoring purposes which were not necessarily conducive to the DAP/CDP environment or which required direct access to the CAMAC system.

GPIG and the E769 Event Display

Two separate interactive graphics routines were used during the operation of E769 to monitor the performance of the detectors. The E769 Event Display allowed immediate observation of tracking through detectors, Cerenkov phototube hits, energy distribution in the calorimeters, etc. The GPIG (General Purpose Interactive Graphics package) allowed the user to examine an event and produce real time histograms of Drift Chamber profiles, SMD hot channels, etc.

"In matters of grave importance it is style, and not sincerity, that is the vital thing." - Oscar Wilde,
The Importance of being Earnest

Chapter 4: Reconstruction, Strip and Analysis Code

E691 used a multi-tiered system for reconstructing their data[45] but E769 decided to amalgamate all the different levels of reconstruction code into a single process. The different parts of the code retained their old functions and name. In general, PASS1 reconstructed track trajectories and momenta while the PASS2 code did preliminary vertexing using the SMD information, threshold Cerenkov analysis and calorimetry. The PASS2 output was the fully reconstructed event. These data were immediately put into a Data Summary Tape (DST) format in order to save the space and cost of output tapes. E769 added a step before PASS1 known as PASS0 which provided the experiment with a useful database of information for every one of the roughly 10,000 data tapes. After recontruction, all the events were put through the 'Pair Strip' which searched through the events looking for those which were consistent with a well separated primary and downstream secondary vertex. The DST format of the Pair Strip served as the input data stream for the KKπ strip for the D_s analysis. All of this code is described in this chapter.

PASS0[46]

Each tape mounted for reconstruction was subjected to a preliminary pass through the first 2000 events on the tape to retrieve data from the raw event such as: SMD hot channels, ADC pedestals, locations and widths of the TRD proton and pion peaks, etc.

The tape was then rewound and during reconstruction (PASS1 and PASS2) the PASS0 code was called for each event on the entire tape to accumulate data such as: mean number

45 Scott Menary, M.Sc. Thesis, University of Toronto, A Study of the Transverse Momentum Distribution of Photoproduced Charged and Neutral D mesons, 1986.

46 Personal correspondence with Joao Mello, December 12, 1990.

of DC hits per plane, the DISC PMT and TRD Plane count frequencies, trigger latch bits, etc.

At the end of the reconstruction job the PASS1 and PASS2 summary files were collected by the PASS0 routines and put into a format suitable for reading with the standard E769 I/O code. This database of information for each reconstructed tape proved invaluable in pointing E769 towards regions of data which were suspicious in a variety of ways.

PASS 1

PASS1 was responsible for tracking particle trajectories through the SMD and DC systems. It also made a preliminary calculation of the beam particle trajectory using the upstream SMD and PWC systems. The trajectory searching routine initiated its search in the SMD system due to the low noise, high efficiency and fine resolution achieved in these planes. Tracks found in the SMD system were extrapolated into the DC system and then tracked through the spectrometer and magnets for momentum determination.

PASS 2 and Data Summary Tapes

The trajectory of the particles determined by the PASS1 code was passed to the PASS2 code in order to extract information from C1 and C2, the SLIC and Hadronic Calorimeters and to match tracks to vertices using only the SMD track information. The PASS2 vertexing worked entirely on the χ^2/DOF of the vertices. It would calculate the χ^2/DOF of the vertex and, if it was greater than 2.0, would remove the track from the vertex which contributed the most to the χ^2/DOF. It would continue this process until the vertex which remained had a $\chi^2/\mathrm{DOF} \leq 2.0$. It would then attempt to fit the tracks which were not in this vertex to another vertex in the same manner until all track combinations had been tried. A list of these vertices was then made available to the user as primary and secondary vertex candidates.

Once the events were entirely reconstructed all information not deemed necessary for a final analysis of the data was discarded and the remaining information was compactified and written to tape. This step gave a reduction factor of two in the number of tapes necessary to maintain the 400 million E769 events.

The Pair Strip

The first analysis pass through the full set of DSTs was a strip intended to select those events containing multiple vertices - candidates for long lifetime secondary charm decay vertices. The PASS2 vertex containing the largest number of tracks was designated as the primary vertex candidate.

All other two-track combinations in the event were tested as secondary decay vertices. If any one of the two-track combinations passed all the cuts the event was written to a Pair Strip Output Tape. A list of the cuts used in this strip is shown in TABLE 4.1.

TABLE 4.1
Pair Strip Cuts

Variable	Cut
z_{pri}	> -6 cm
σ_z	< 180μm
z_{sec}	> -6 cm
$(\chi^2/DOF)_{sec}$	< 5
RAT	< 0.06
SDZ	> 6.0
PT2DK	> 0.1 GeV^2

Since many of these cuts were also used in the D_s analysis they will be explained in some detail here. z_{pri} and z_{sec} are the z-location of the primary and secondary vertices respectively. These cuts gaurantee that the vertices are upstream of the last beam telescope SMD plane. A cut on the error in the z-location of the primary vertex (σ_z) ensures that the

primary vertex candidate is formed from good quality tracks and is itself a good vertex. A loose cut on the χ^2/DOF of the secondary vertex ensures good secondary vertex quality.

The RAT, SDZ and PT2DK cuts are shown schematically in FIGURE 4.1.

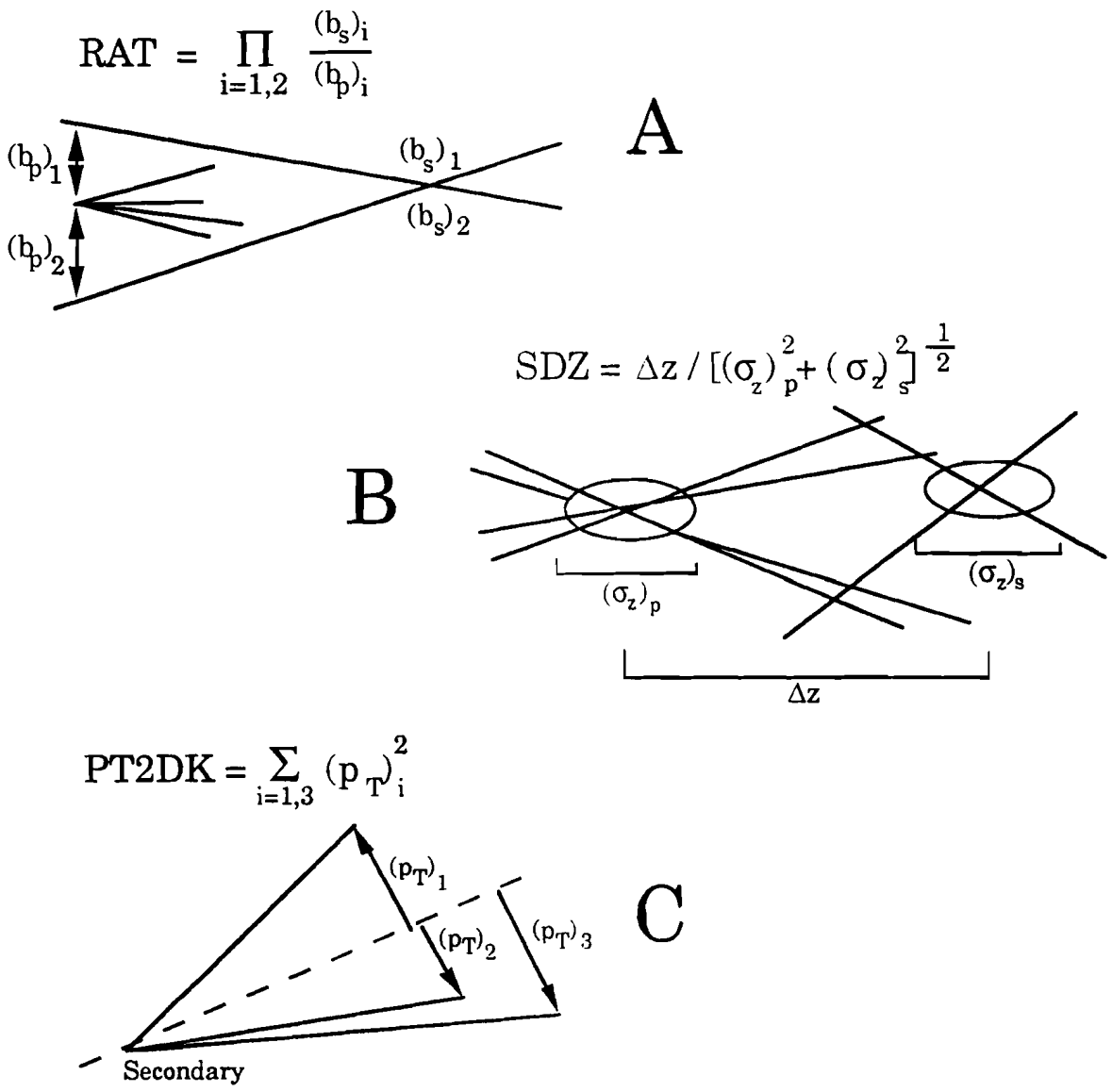

FIGURE 4.1
Various cuts used in the Pair and subsequent Strips
A) the RAT cut B) the SDZ cut and C) the PT2DK cut

The RAT cut is a means of accepting only those secondary candidates which are associated with tracks which pass closer to the secondary than primary candidate. It is defined as:

$$\mathrm{RAT} = \prod_{i=\text{secondary tracks}} \frac{(b_s)_i}{(b_p)_i}$$

where $(b_s)_i$ and $(b_p)_i$ are the impact parameters of the tracks (i) in the secondary vertex candidate to the secondary and primary vertex locations respectively. The SDZ cut checks on the statistical significance of the separation of the primary and secondary vertices and is defined in the following manner:

$$\mathrm{SDZ} = \frac{z_{sec} - z_{pri}}{\sqrt{\Delta z_{sec}^2 + \Delta z_{pri}^2}}$$

where Δz_p and Δz_s are the errors on the fitted primary and secondary vertex locations respectively. PT2DK is the sum of the squares of the transverse momentum of the decay particles with respect to the direction of motion of the decaying particle:

$$\mathrm{PT2DK} = \sum_{i=\text{secondary tracks}} \left(p_T^2\right)_i$$

The Pair Strip had a rejection factor of about 14 while being almost 100% efficient for the final D_s sample.

The $\varphi\pi$ and K*K sub-strips

The D_s strip was run in two separate stages. The first stage was the initial strip from the pair stripped events known as DS3IN1 (for three different $D_s^+ \rightarrow K^+K^-\pi^+$ modes) and the second stage was the strip for each individual mode: DSPHIPI and DSKSTARK (for the obvious resonant modes). All the strip and final analysis cuts are listed in TABLE 4.2 in the order in which they were applied in the final analysis. The cuts are explained in this section.

In DS3IN1 the events were first checked for D_s decays consistent with the $\varphi\pi$ ($\varphi \rightarrow K^+K^-$) decay mode using a tight cut on the φ resonant mass. If the event passed these cuts it was sent to the output tape. If the event was not consistent with the $\varphi\pi$ mode it was checked for consistency with the K^*K ($K^* \rightarrow K^+\pi^-$) mode with slightly looser cuts on the wider K^* resonant mass. Since opening the mass window for this decay mode increased the number of events to pass through this part of the strip a tighter cut was used on the downstream kaon probabilities. Finally, if the event did not satisfy the requirements to pass either the $\varphi\pi$ or K^*K cuts it was checked for consistency with the non-resonant $KK\pi$ decay mode of the D_s. In order to compensate for the lack of a cut on a resonant particle mass the cuts on the downstream Cerenkov kaon probabilities were made even tighter. The non-resonant $KK\pi$ decay mode did not produce a significant D_s signal and was plagued by feedthrough from the high statistics $D^+ \rightarrow K^-\pi^+\pi^+$ signal. It was not used in any of the following analysis. Further discussion of this mode will be suppressed.

The DSPHIPI and DSKSTARK routines separated the two resonant decay modes onto different tapes without including any tighter cuts on the data. They produced the HBOOK/PAW NTUPLE[47] which was used for the remainder of the analysis. In total, 2946 events passed the $\varphi\pi$ strip while 15940 events passed the requirements of the K^*K strip. These numbers correspond to rejections of about 1.4×10^5 and 2.5×10^4 from the raw data respectively.

Most of the final analysis cuts were chosen using a standardized method of maximizing the statistical significance of the Monte Carlo (see Chapter 5) signal to the real background data. This was done in order to avoid optimizing cuts to enhance statistical fluctuations in the signal. First, a histogram (H1) was made of the MC

47 CERN Program Library entry Q121, Version 1.07 (October, 1989). The PAW NTUPLE has become a standard method for interactive analysis of HEP data.

TABLE 4.2
Cuts used in the $\varphi\pi$ and K*K sub-strips
The cuts are described in detail in the text.

Cut	$\varphi\pi$ sub-strip		K*K sub-strip	
	Strip	Final Analysis	Strip	Final Analysis
$(\chi^2/DOF)_{track}$	< 5.0	< 5.0	< 5.0	< 5.0
P_{track}	< 250 GeV	< 250 GeV	< 250 GeV	< 250 GeV
JCAT	3≤JCAT≤15	3≤JCAT≤15	3≤JCAT≤15	3≤JCAT≤15
$C1_K$	≥ 0.13	≥ 0.13	none	none
$C2_K$	≥ 0.13	≥ 0.13	none	none
$C1_K \times C2_K$	none	none	≥ 0.1	≥ 0.1
m_ϕ	± 10 MeV	± 10 MeV	none	none
m_{K^*}	none	none	± 50 MeV	± 50 MeV
DIP_{KK}	≤ 100 μm	≤ 100 μm	≤ 100 μm	≤ 100 μm
m_{Ds}	≥ 1.77 GeV < 2.07 GeV	≥ 1.77 GeV < 2.07 GeV	≥ 1.77 GeV < 2.07 GeV	≥ 1.77 GeV < 2.07 GeV
PT2DK	≥ 0.1 GeV^2	≥ 0.1 GeV^2	≥ 0.1 GeV^2	≥ 0.1 GeV^2
$\lvert \cos\theta \rvert$	none	≥ 0.56	none	none
$(\chi^2/DOF)_{sec}$	≤ 5.0	≤ 5.0	≤ 5.0	≤ 5.0
z_{pri}	≥ -5.5 cm ≤ 0.5 cm	≥ -5.5 cm ≤ −0.9 cm	≥ -5.5 cm ≤ 0.5 cm	≥ -5.5 cm ≤ −0.9 cm
x_F	none	≥ 0	none	≥ 0
p_T^2	none	≤ 10	none	≤ 10
SDZ × PT2DK	none	≥5	none	≥5
SDZ	≥ 6	≥ 8	≥ 6	≥9, ≤3τ(D_s)†
$(\chi^2/DOF)_{pri}$	≤ 5.0	≤ 5.0	≤ 5.0	≤ 5.0
DIP	≤ 100 μm	≤ 100 μm	≤ 100 μm	≤ 60 μm
ISO	≥ 20 μm	≥ 20 μm	≥ 20 μm	≥ 20 μm
RAT	≤ 0.02	≤ 0.02	≤ 0.02	≤ 0.02

† an SDZ cut of 9 and a requirement that the secondary decay vertex be located within 3 D_s lifetimes of the physical location of the SDZ cut for the event.

distribution of the variable for which a cut was to be chosen in the D_s mass window ($1.955GeV \leq D_s \leq 1.985GeV$) while the strip cuts were in effect. Second, a histogram (H2) was made of the same variable, with the same cuts in place, for the MC events in the 70 MeV wings on either side of the D_s window. The contents of each bin of H2 were normalized to the background expected in the signal region and subtracted from the contents of H1 leaving the distribution of the variable for the D_s signal in the MC (H3 = H1 - N×H2). Third, the distribution of the same variable in the real data with the same cuts applied and in the D_s wings was produced (H4). Finally, each bin of H3 was divided by the square root of the corresponding bin in H4 to produce a plot showing a continuous $\frac{S}{\sqrt{B}}$ as a function of the cut on the variable in question (FIGURE 4.2A). The variable was then fixed at the value which produced the best $\frac{S}{\sqrt{B}}$ and the method was repeated to find the next best cut to maximize $\frac{S}{\sqrt{B}}$. The procedure was continued until the $\frac{S}{\sqrt{B}}$ in the real data was at a maximum. FIGURE 4.2B shows the efficiency of the SDZ×PT2DK cut with respect to the value of the cut. The cut suggested by FIGURE 4.2A of SDZ×PT2DK≥5 has an efficiency of about 70%.

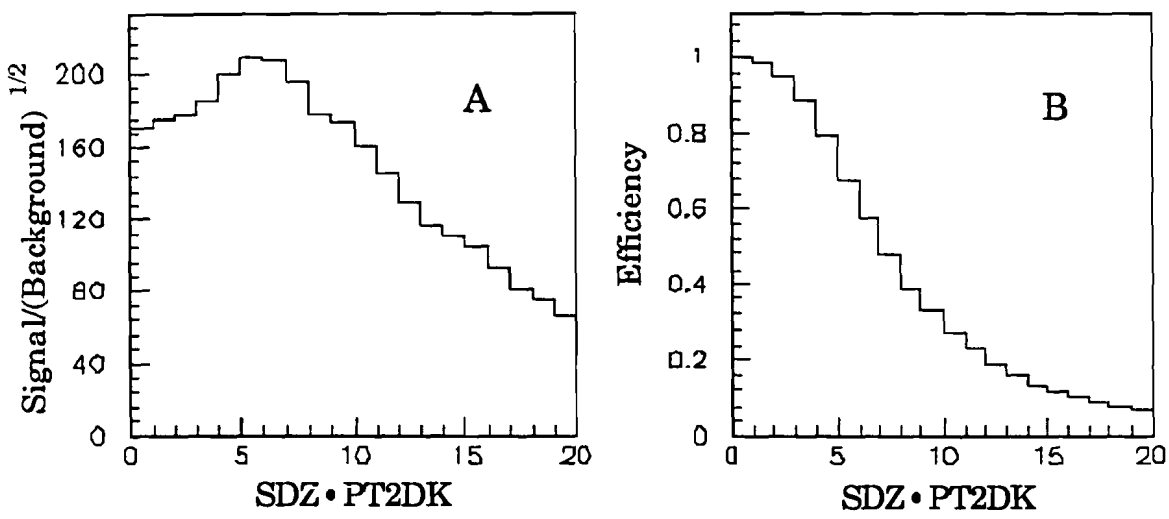

FIGURE 4.2
Efficiency and Signal to background as a function of SDZ×PT2DK for the $D_s \rightarrow \phi\pi$ signal

Other cuts were chosen on a purely physical basis. If the beam momentum was 250 GeV it was impossible to have any track in the detector with a calculated momentum >250GeV. JCAT was a word in which each of the first four successive bits corresponded to the track passing through another DC group. The first bit was turned on if the track passed through the D1 group, the second bit if the track passed through the D2 group and so on. The cut on JCAT is therefore equivalent to requiring that the track at least pass through D2. Since D2 was the first DC after M1 the cut is tantamount to requiring some momentum information. Bits higher than the fourth bit in JCAT were turned on for tracks which were only identified in the DC system. All of the cuts on the χ^2/DOF for each individual K or π track and for the fit to the secondary and primary vertices were set very loose by examining the distribution of these variables in the MC data.

The cuts on the downstream K probabilities (C_{K1} and C_{K2} for the first and second kaons in the decay respectively) as reported by the threshold Cerenkov counters were chosen using the $\frac{S}{\sqrt{B}}$ method. The cut at 0.13 was just above the *a priori* probability for kaons (0.12) after interactions in the target. The m_ϕ and m_{K*} cuts were requirements that the mass of the ϕ and K^* candidates lie within the specified mass ranges. A K^+K^- invariant mass distribution for the ϕ was shown in FIGURE 3.29. Once the resonant particle candidate's mass was found to lie within its allowed mass range its mass was fixed at the accepted values[48] of the ϕ and K^* mass (1019.412MeV and 891.83MeVrespectively) when calculating the D_s mass. This method was tested with the MC and gave a better resolution for the D_s than simply using the calculated ϕ or K^* mass.

The DIP_{KK} cut was a requirement on the impact parameter of the two kaon track candidates. The allowed range on the calculated mass of the D_s candidate was extended to 100 MeV below the $D^\pm$ since the $D^\pm$ has a cabbibo suppressed decay to each of the two

48 M. Aguilar-Benitez et al., The Particle Data Group, 1990 Review of Particle Properties, Physics Letters B239, p. VII.96.

resonant modes studied. The presence of the cabibbo suppressed $D^{\pm}$ decay was a good check on the D_s signal. The cut on z_{pri} was tighter than the cut used in the pair strip in order to guarantee that the primary vertex was in the target.

When a pseudo-scalar ($J^P=0^-$) particle decays into a vector ($J^P=1^-$) particle and another pseudo-scalar, subsequently followed by the decay of the vector particle into two pseudo-scalars, spin conservation requires that the vector particle decays into an l=1 state.

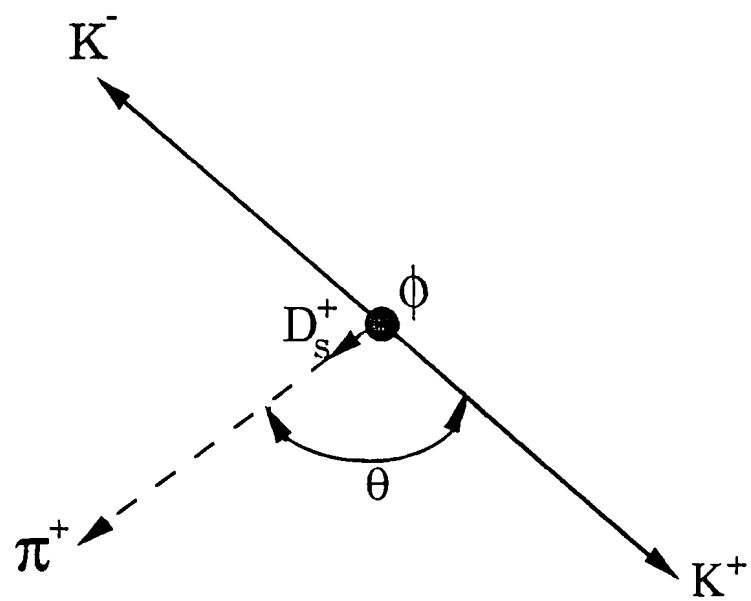

FIGURE 4.3
Schematic representation of the angle θ in resonant $D_s \rightarrow \phi\pi$ decays
The angle is always calculated as the angle between the like-sign particles.

In the rest frame of the vector meson the angle (θ) between one of the vector meson's decay products and the pseudo-scalar meson from the first decay must be distributed according to $\cos\theta$. The cut for this variable was determined analytically by assuming that the distribution of the background events in $\cos\theta$ was flat and that the number of background events was very large relative to the number of D_s events. Under these conditions it was simple to show that the cut which maximized $\frac{S}{\sqrt{B}}$ was $|\cos\theta| \geq 0.56$. The assumption of a flat background distribution in $\cos(\theta)$ was verified in the data. The value of the $|\cos(\theta)|$

cut suggested by the systematic MC method described above is consistent with the analytically determined cut. For the sake of consistency the angle was always calculated as that between the two like-sign particles in the decay. The decay is illustrated in FIGURE 4.3.

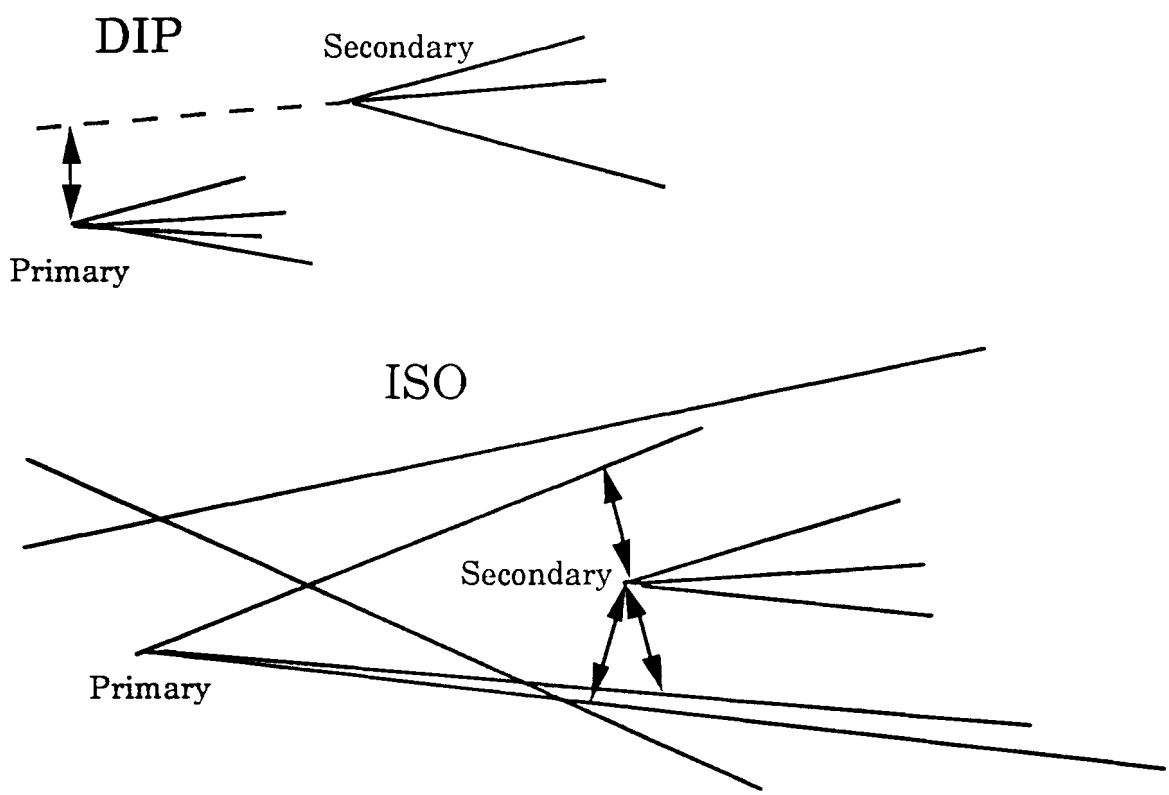

FIGURE 4.4
Schematic representation of the DIP and ISO cuts

The DIP and ISO cuts are shown schematically in FIGURE 4.4. They are respectively: a cut on the impact parameter of the reconstructed 3-momentum of the D_s candidate at the fitted location of the primary vertex candidate and an isolation requirement such that no track in the event other than the three secondary track candidates pass within a certain distance of the fitted location of the secondary vertex. Unlike the pair strip, which assigned the vertex with the most tracks as the primary vertex, the D_s analysis assigned the vertex with the smallest DIP as the primary.

The rejection factors for the final analysis cuts from the raw data were about 1.3×10^6 and 1.0×10^6 respectively. The $KK\pi$ invariant mass plots using these analysis cuts will be shown in Chapter 6: Results and Discussion.

"There are three types of lies: lies, damned lies, and statistics."
- Benjamin Disraeli

Chapter 5: The E769 Monte Carlo

The E769 Monte Carlo (MC) used PYTHIA 4.8[49] to generate the interaction between the incoming beam particles and the target particle. PYTHIA generates the charmed quarks using a LO QCD motivated generator which ignores the charm quark mass and introduces a cut off in p_T^2 to avoid singularities. JETSET 6.3[49] was then called to hadronize the partons into observable particles and specify their properties (e.g. momentum, energy, etc). The JETSET routine is based on the LUND string fragmentation model.

A detector tracking routine was then called which extrapolated the trajectories of these particles through the spectrometer performing all the applicable decays of unstable particles, Coulomb scattering and secondary interactions in downstream detectors, and bending the particles through the two magnets. This routine would calculate, for each z-plane of the SMD, DC and PWC systems, the (x, y) coordinates of the particles trajectory, the number of photoelectrons produced in the two downstream Cerenkov counters and the tracking of the Cerenkov photons to the z-plane of the Cerenkov mirror system, and the electromagnetic and hadronic energy deposited in the calorimeters. The output of this section of code was known as the 'Truth Table'.

The 'Digitizer' routine used the Truth Table to put the event into the format of an E769 event. It was in this section of code that the modelling of each of the spectrometer's detectors was performed. This included taking into account the efficiencies and adding noise in the Cerenkov Counters, Calorimeter and Muon wall phototubes and also in the SMD and DC planes. The MC also modelled dead channels in the SMD and DC systems as well as the 'efficiency hole' in the DC system caused by non-interacting beam particles.

---

[49] FNAL Publication PM0050 or CERN Long Program Writeups W5035 and W5046.

Using this MC we were able to model the detector in order to correct the observed data for the biasing of the detector triggers and analysis cuts. FIGURE 5.1[50] is a bin-by-bin division of the $D^+ \rightarrow K^-\pi^+\pi^+$ MC and real $D^+ \rightarrow K^-\pi^+\pi^+$ background-subtracted x_F distributions with the D^+ cuts applied. Similarly, FIGURE 5.2[50] shows the same ratio for the p_T^2 distributions. We use the $D^\pm$ to illustrate the utility of the MC since only this signal had a sufficient number of events to justify comparison between data and the MC. FIGURE 5.1 shows that the MC produces more high x_F D^+ than the data. FIGURE 5.2 shows that the MC does not produce enough events in the region $p_T^2<1$.

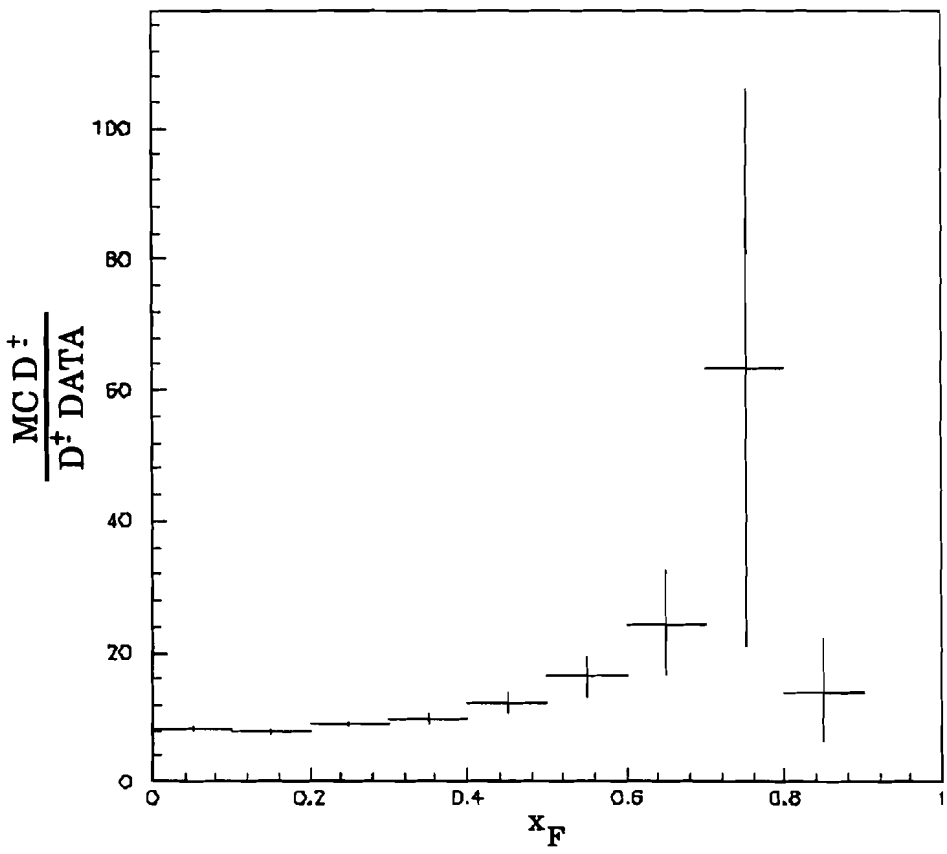

FIGURE 5.1

The ratio of the MC $D^+ \rightarrow K^-\pi^+\pi^+$ x_F distribution to the background subtracted $D^+ \rightarrow K^-\pi^+\pi^+$ distribution with the $D^+ \rightarrow K^-\pi^+\pi^+$ analysis cuts in place

50 courtesy of C. Gay, L. Lueking, E769 members.

The version of the MC used in this thesis has a leading particle effect in which the produced charm quark will often link with a fast quark in the beam particle to produce a high x_F charmed meson or baryon. As stated earlier, it also introduces a p_T cutoff to compensate for m_c=0. These aspects explain the trends in the ratios shown in FIGUREs 5.1 and 5.2. A newer version of the MC reduces these effects. In the new version PYTHIA is replaced by a LO QCD charm quark generator which does not ignore the mass of the charm quark and makes no cut-off in p_T. Once the charm quark pair is produced, the energy of the pair is removed and FRITIOF[51] is called upon to produce the soft processes in the

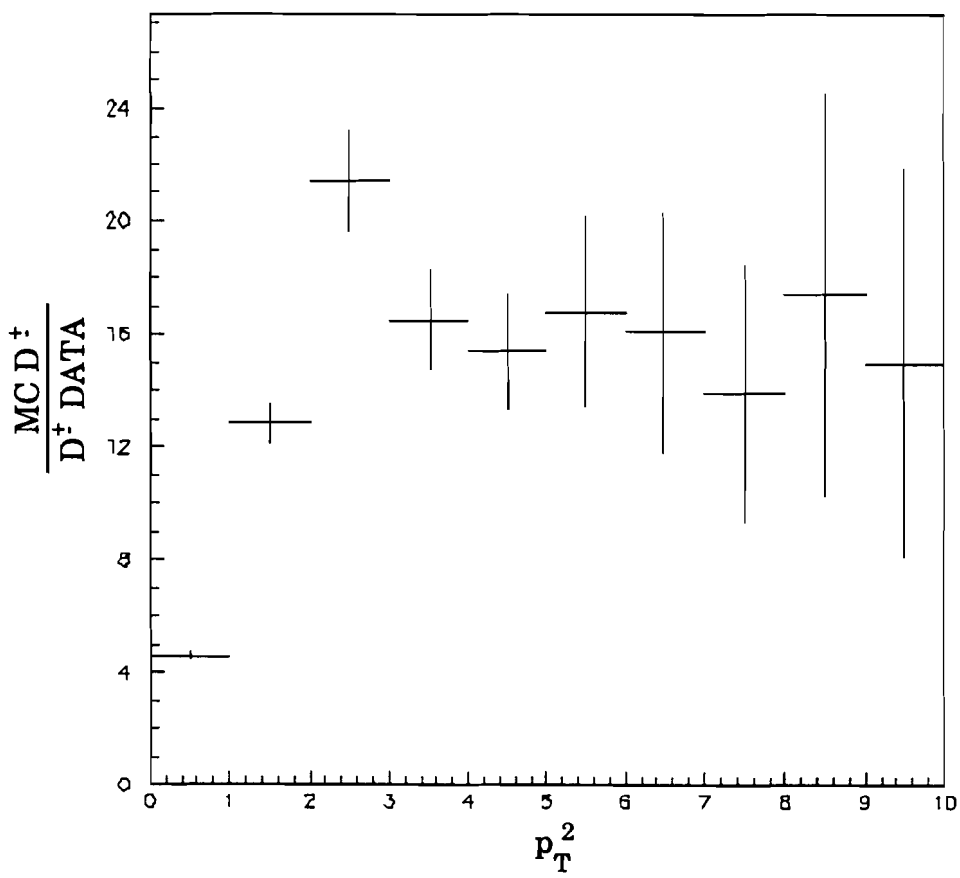

FIGURE 5.2
The ratio of the MC $D^+ \rightarrow K^- \pi^+ \pi^+$ p_T^2 distribution to the background subtracted, D^+ p_T^2 distribution with the D^+ analysis cuts in place

[51] supported and documented in the new CERN Library version CNL201.

underlying event. The new version of the MC is currently under study to determine if it should be used in place of the version used here.

Using the acceptance calculated from the MC the corrected x_F and p_T^2 distributions for the $D^+ \rightarrow K^+\pi^+\pi^-$ are shown in FIGURE 5.3 and FIGURE 5.4 respectively. The D^+ acceptance is very similar to the D_s acceptance in both x_F and p_T^2. The acceptances for the D_s are shown in FIGUREs 6.3 and 6.4. The differential x_F cross section has been fit to a function of the form $(1-x_F)^n$ and n is found to be 3.1±0.3[52] for $x_F>0.0$ in agreement with measurements of the same quantity at other laboratories[53]. Similarly, the p_T^2

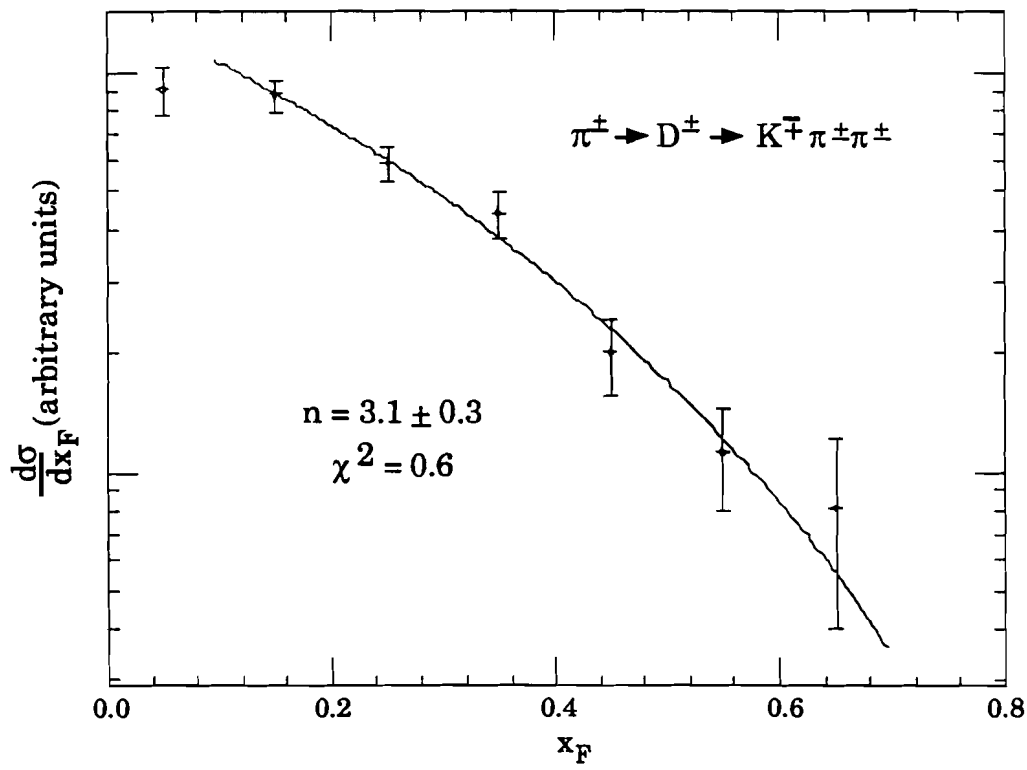

FIGURE 5.3
Acceptance corrected x_F distributions for the D^+ signal.
(Fit for $x_F>0.1$)

52 courtesy of Lee Lueking, E769 member. Error is statistical only.
53 S. Barlag et al., Z. Phys. C 49, (1991) p.555. They report n=3.77±0.40 and b=0.86±0.06.

distribution has been fit to a function of the form $\exp(-bp_T^2)$ and b is found to be 1.02±0.06 (E769, ref. 2), consistent at the 2σ level with other measurements of the same quantity (Barlag et al., ref. 53).

FIGURE 5.5 shows the MC x_F distribution for charmed quarks and the D_s mesons which they produce (all the results discussed in this thesis use MC generated events in a pion beam). Also shown is the fitted value of n for a function of the form $(1-x_F)^n$. The x_F distribution for the charmed quarks agrees exactly with the value of n=4.5 predicted in Chapter 1.

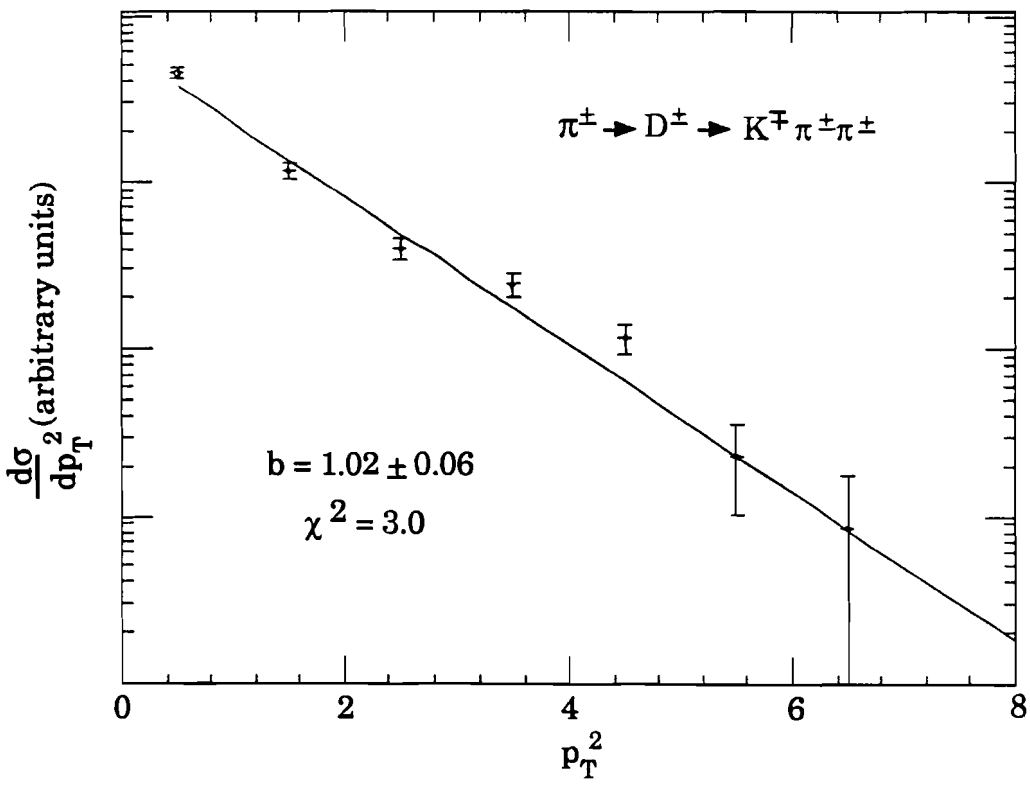

FIGURE 5.4
Acceptance corrected p_T^2 distributions for the $D^\pm$ signal.

Note that, unlike the results shown in Chapter 1 (see FIGURE 1.10 and TABLE 1.2), the MC generated D_s mesons have a harder x_F distribution than the charm quarks. In this MC the charm quark links up with a fast strange sea-quark in the incoming pion to form the

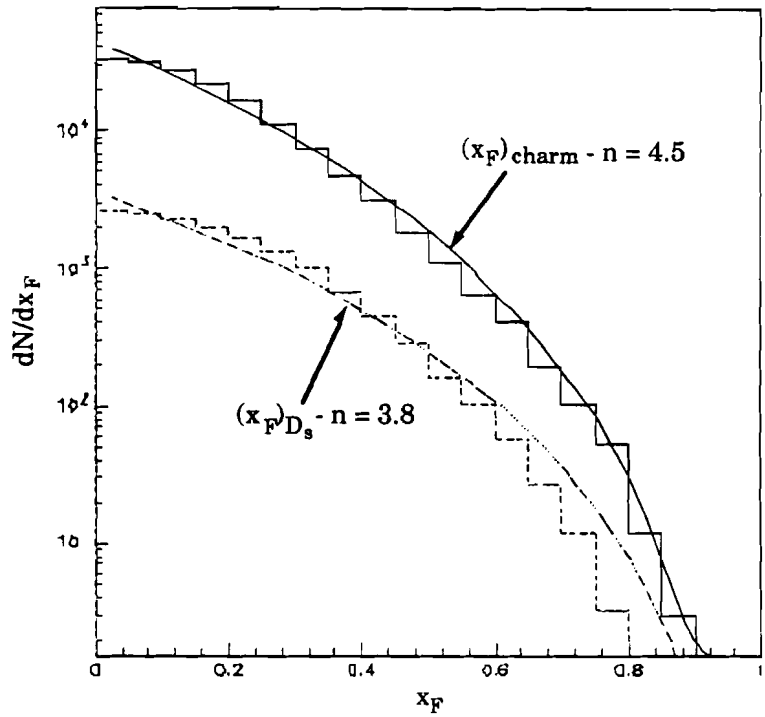

FIGURE 5.5
MC x_F distribution of charm quarks and the D_s mesons they produce

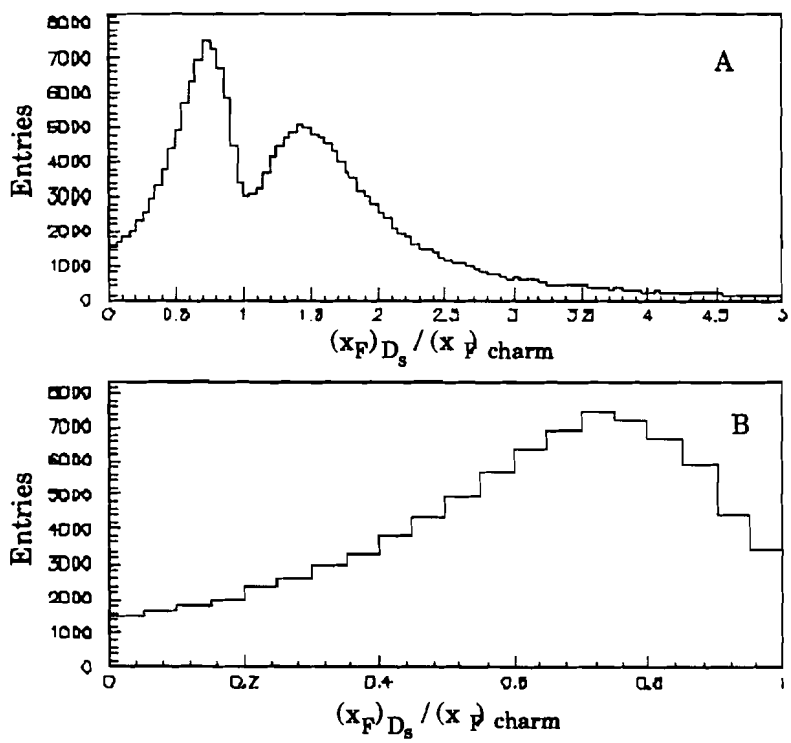

FIGURE 5.6
MC x_F (D_s) / x_F(charm)

D_s. FIGURE 5.6A and 5.6B show that approximately 60% of the D_s mesons are faster than the charmed quark which preceeded them.

When the D_s meson's x_F is less than the charmed quark's x_F as in FIGURE 5.6B the distribution looks very similar to the theoretical fragmentation functions shown in FIGURE 1.15B.

FIGURE 5.7 shows the MC generated p_T^2 distribution for both the charm quarks and the D_s they produce. The plots have been fit to functions of the form $\exp(-bp_T^2)$ as was done in Chapter 1. The fitted value of the parameter b (as shown on the FIGURE 5.7) in the MC agrees with the value shown in FIGURE 1.12 of b=0.46. The D_s mesons have a softer p_T^2 distribution than the charm quark itself.

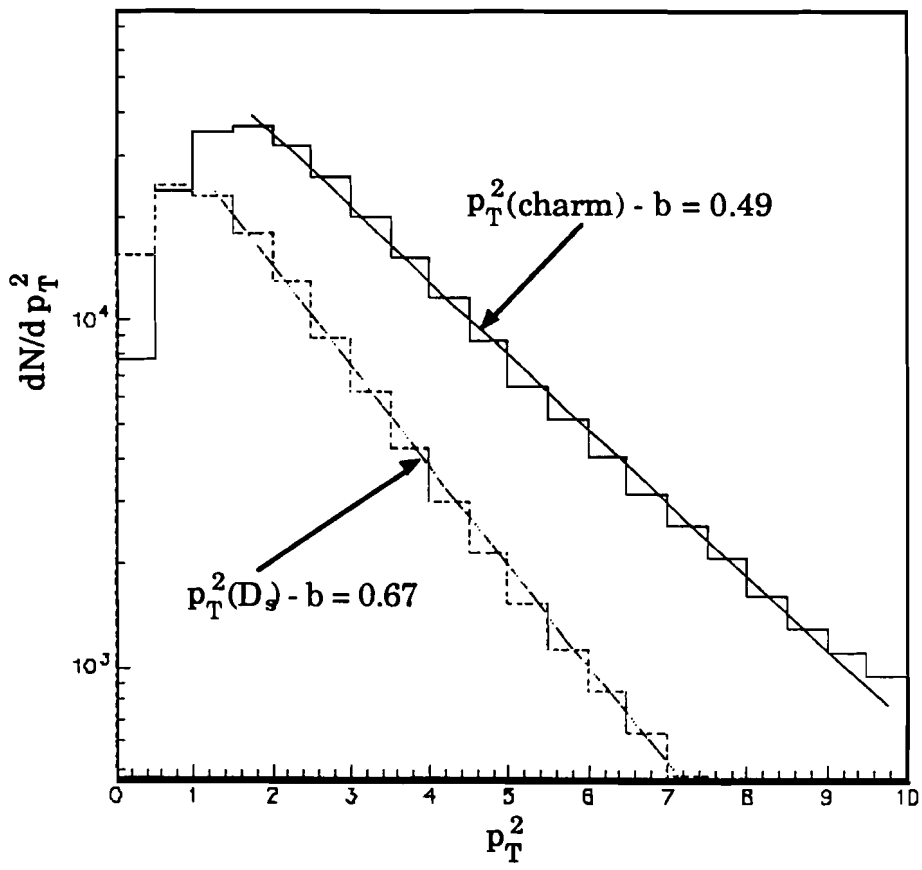

FIGURE 5.7
MC p_T^2 distribution of charm quarks and the D_s mesons they produce

Chapter 6: Results and Discussion

Using the final set of analysis cuts from TABLE 4.2 for both decay modes, the combined $D_s \rightarrow \phi\pi$ and $D_s \rightarrow K^*K$ signals with no requirement on the trigger type are shown in FIGURE 6.1. This mass distribution was first fit with both the peak locations, widths and normalizations of the gaussians representing the D^+ and the D_s floating. All the fits use a linear background distribution. The fitted values of the D^+ and D_s mass were 1.8735±0.0019GeV and 1.9720±0.0020GeV respectively. All subsequent distributions were then fit to gaussians of 10MeV width centred at 1.8735GeV(D^+) and 1.9720GeV(D_s) as

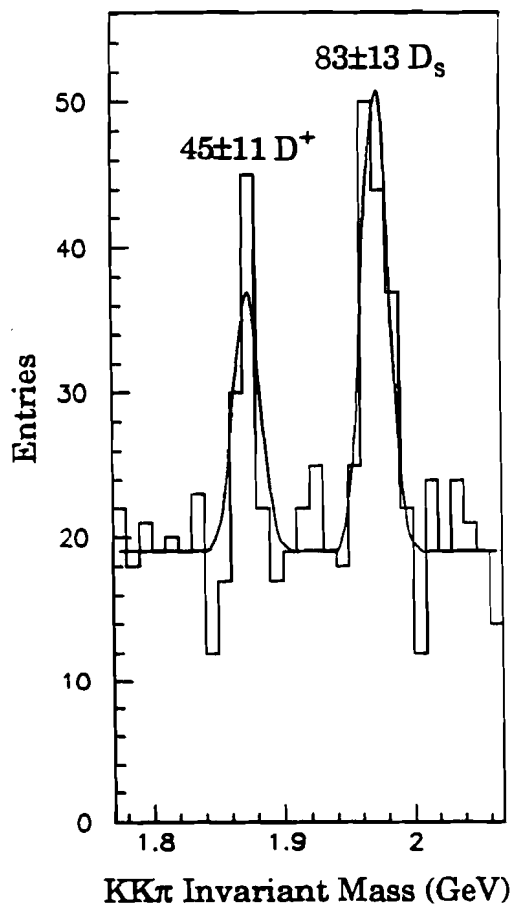

FIGURE 6.1
Final combined $D_s \rightarrow \phi\pi$ and $D_s \rightarrow K^*K$ signals.
No requirement has been made on the trigger or incident particle type.

suggested by the first fit and in agreement with the MC. The fit, shown in FIGURE 6.1, with fixed width and peak locations yielded 83±13 D_s and 45±11 D^+.

In FIGURE 6.2 the signals are divided into the two separate decay modes also with no requirement on the trigger type. The fits yield 43±9 D_s and 29±8 D^+ in the $\phi\pi$ decay mode and 40±10 D_s and 17±8 D^+ in the K^*K decay mode.

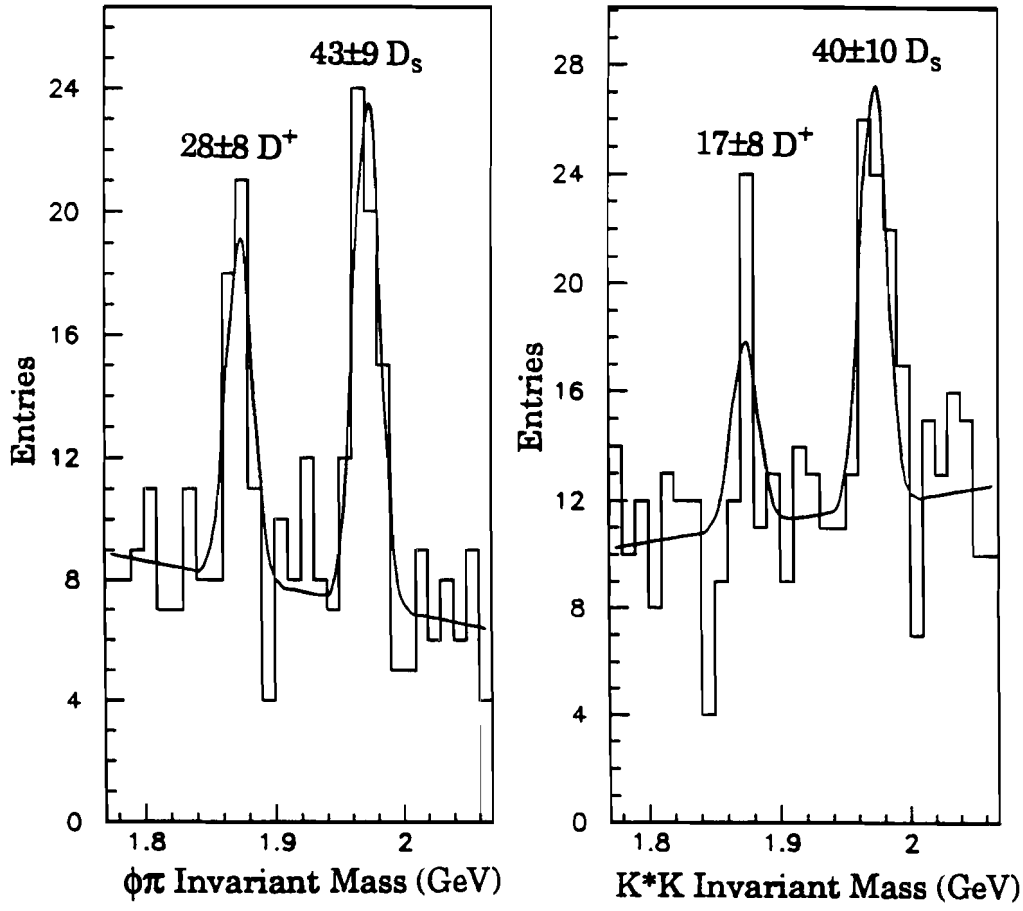

FIGURE 6.2
$D_s \rightarrow \phi\pi$ and $D_s \rightarrow K^*K$ signals.
No requirement has been made on the trigger or incident particle type.

TABLE 6.2 gives the final number of events in each of the two resonant decay modes for the three different beam particles requiring only the E_T(stnd) or E_T(kaon) trigger. Each beam encompasses both the positive and negative data. The cut on each of the beam particle probabilities was >0.9. The numbers in this table were obtained using a maximum

likelihood fit to the mass distributions as explained in APPENDIX C. The total Kaon induced D_s sample is almost 4 times larger than the sample obtained by the ACCMOR collaboration and is the largest single sample of $KN \rightarrow D_s X$ in the world..[54]

TABLE 6.2
Number of D_s decays divided into incident particle and trigger types (x_F>0.0).

	$D_s \rightarrow \phi\pi$			$D_s \rightarrow K^*K$		
Trigger	π beam	K beam	p beam	π beam	K beam	p beam
E_T	9.1±5.1	6.5±3.0	1.1±2.5	20±6	8.3±4.0	4.5±3.4

Cross Section × Branching Ratio and Total Cross Section Measurements

The numbers shown in TABLE 6.2 have been used in the determination of the D_s cross sections as explained in Appendix A and B. The final number of π, K, and p induced D_s in the E_T trigger data are 29±8, 15±5 and 5.6±4.2 respectively. We calculate the average $\sigma \times B$ per nucleon for the two modes in the x_F region to which our experiment was sensitive (x_F>0.0) and the results are shown in TABLE 6.3. The acceptance in this x_F region was 0.0186±0.0037 and 0.0111±0.0022 for the $\phi\pi$ and K^*K modes respectively. The error is dominated by the error due to a correction between the MC and the data downstream Cerenkov counter efficiency (see Chapter 3: Cerenkov Kaon Efficiency).

We use the ratio of the branching fractions ($BR(D_s \rightarrow K^*K)/BR(D_s \rightarrow \phi\pi)$=0.96±0.11) (M. Aguilar-Benitez et al., ref. 1) to normalize the $D_s \rightarrow K^*K$ to the $\sigma \times B$ for the $D_s \rightarrow \phi\pi$ mode. We then calculate a single, weighted average $\sigma \times B$ for the D_s . The weights for the averages are taken as $(\Delta\sigma_{uncommon}^2 + \Delta\sigma_{statistical}^2)^{-1}$ where $\Delta\sigma_{uncommon}$ is the quadratic sum of the non-common systematic errors on each of the cross sections as explained in Appendix B.

54 S. Barlag et al., Z. Phys. C 49, (1991) p.555

The common systematic errors are added back into the total error in quadrature after averaging.

The result using A^1 is included for better comparison to other experiments which have always used A^1 for lack of a good measurement of the A-dependence in charm hadroproduction. The value for the A-dependence measured in our experiment (α=0.95±0.05[55]) for the $D^{\pm}$ is the world's best measurement of this quantity in open charm production. When the measured A-dependence is used to calculate the nucleon cross section the systematic error increases due to the error on α and the extrapolation to A=1.

TABLE 6.3
σ(nucleon)×B for x_F>0.0 assuming A^1 and $A^{0.95\pm0.05}$
averaged over two decay modes (all values in μb/nucleon)

	Average ($D_s \to \phi\pi$ and $D_s \to K^*K$)		
	π beam	K beam	p beam
A^1	0.030±0.011	0.037±0.013	0.029±0.020
$A^{0.95\pm0.05}$	0.036±0.015	0.044±0.018	0.035±0.025

Using A^1 for the π and K beams as shown in TABLE 6.3, we find σ×B in agreement with recent results from the ACCMOR collaboration at CERN (Barlag et al., ref. 54). They quote $\sigma(D_s^+)\times\sum B(D_s^+\to K^+K^-\pi^+)$[56] values of 0.067±0.011±0.010 and 0.11±0.06±0.02 for their π^- and K^- beam respectively for the region x_F>0. The summation is over the branching ratios to the three D_s^+ decay modes: $\phi\pi^+$ ($\phi\to K^+K^-$), K^*K^+ ($K^*\to K^-\pi^+$) and $K^+K^-\pi^+$(non-resonant). Using the world average ratios of the branching fractions of the last two decay modes to the $\phi\pi$ mode of $B(D_s\to\phi\pi)$: $B(D_s\to K^*K)$: $B(D_s\to KK\pi(nr))$ = 1 : 0.96±0.11 : 0.25±0.09 (Aguilar-Benitez et al., ref. 1) implies that ACCMOR's measurement would

55 personal correspondence with Lee Lueking - E769 member. Error is the quadratic sum of the systematic and statistical errors.

56 personal correspondence with Simon Kwan, E769 member and former NA32 member.

yield an average $\sigma \times B$ for the resonant modes of 0.030±0.007 and 0.048±0.026 for their pion and kaon sample's respectively. These values are in agreement with those given in TABLE 6.3.

Using the MC to extrapolate the $\sigma \times B$ to all x_F we find the values shown in the following TABLE 6.4. For all x_F the acceptances were 0.0112±0.0022 and 0.0067±0.0013 for the $\phi\pi$ and K^*K modes respectively.

TABLE 6.4
σ(nucleon)×B for all x_F assuming A^1 and $A^{0.95\pm0.05}$
Averaged over two decay modes (all values in μb/nucleon)

	Average ($D_s \to \phi\pi$ and $D_s \to K^*K$)		
	π beam	K beam	p beam
A^1	0.050±0.018	0.061±0.022	0.048±0.033
$A^{0.95\pm0.05}$	0.060±0.025	0.074±0.030	0.058±0.041

The values in TABLE 6.5 for the total cross sections were calculated by normalizing the K^*K decays to the $\phi\pi$ decays in the same way as in TABLEs 6.3 and 6.4. The world-

TABLE 6.5
σ(nucleon) assuming A^1 and $A^{0.95\pm0.05}$ for limited and all x_F
using the ratio of the two Branching Fractions to normalize the K^*K decays
(all values in μb/nucleon)

	Averaged $D_s \to \phi\pi$ and $D_s \to K^*K$		
	π beam	K beam	p beam
	$x_F>0.0$		
A^1	1.1±0.5	1.4±0.6	1.1±0.8
$A^{0.95\pm0.05}$	1.3±0.6	1.6±0.8	1.3±1.0
	All x_F		
A^1	1.8±0.8	2.2±1.0	1.8±1.3
$A^{0.95\pm0.05}$	2.2±1.1	2.7±1.3	2.1±1.6

average branching fraction of 0.027±0.007 (Aguilar-Benitez et al., ref. 1) was then used to convert from $\sigma \times B$ to σ. The weighting method for the average is also identical. TABLE 6.5 should be compared to the theoretical predictions given in TABLE 1.1. The predicted total charm quark cross sections are 12.1, 13.3 and 13.5 μb/nucleon for the π, K and p beams respectively. These results imply that the charm quark fragments into D_s mesons slightly more than 10% of the time for each of the three beam particle types.

To examine the flavour dependence of the hadro-production of D_s mesons we calculate the ratio of the kaon and proton D_s cross sections to the pion cross section for $x_F>0$ and $A^{0.95}$. The error on the ratio is calculated by assuming that common systematic errors in the cross sections cancel. The results are given in TABLE 6.6.

TABLE 6.6
Ratios of the K and p cross sections to the pion cross section for D_s production

$\frac{\sigma(KN \to D_s)}{\sigma(\pi N \to D_s)}$	$\frac{\sigma(pN \to D_s)}{\sigma(\pi N \to D_s)}$
1.2±0.7	1.0±0.8

Both of these ratios are consistent with being equal to unity. Thus, we see no evidence of a flavour dependence in the cross section for hadronic production of D_s mesons. The K/π ratio is consistent with the value measured by the ACCMOR collaboration at CERN of 1.6±0.6 (Barlag et al., ref. 54).

Differential Cross Section Measurements

We can also examine the flavour dependence in the x_F and p_T^2 distributions for the D_s mesons. The acceptance in x_F and p_T^2 as calculated from the MC are shown in FIGURE

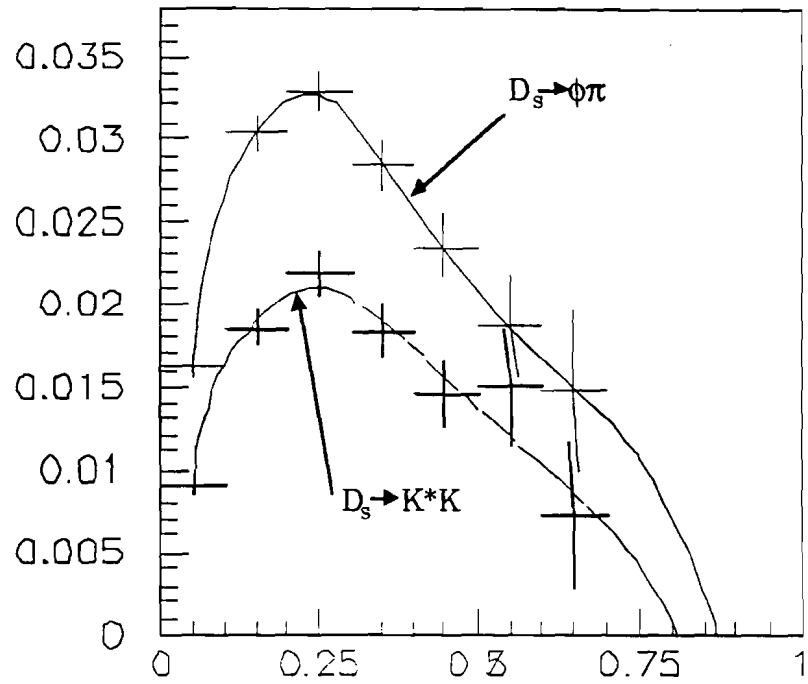

FIGURE 6.3
x_F acceptance as calculated from the MC
The fit is to a fourth order polynomial. The fitted values are given in APPENDIX C.

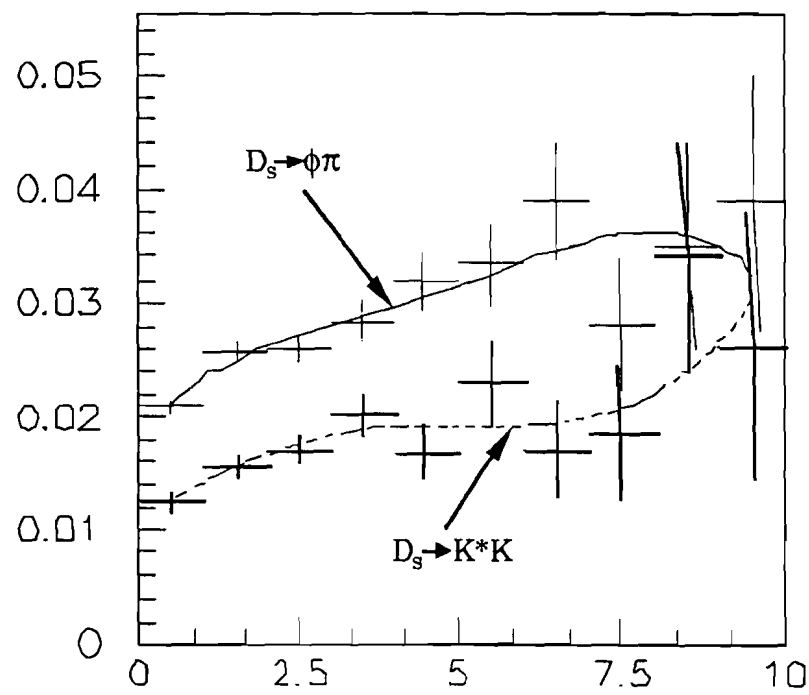

FIGURE 6.4
p_T^2 acceptance as calculated from the MC
The fit is to a fourth order polynomial. The fitted value are given in APPENDIX C.

6.3 and 6.4 respectively. The acceptance drops at x_F~0 mostly due to the geometry of the detector while the drop at high x_F is due mostly to the vertex cuts although the DC hole and trigger also contribute. The acceptance at low p_T^2 is also affected by the DC holes and E_T trigger but is mostly due to the analysis cuts. We see no correlation between the x_F and p_T^2 acceptances.

In each case, the acceptance for the K^*K decay mode is less than that of the $\phi\pi$ mode since the cuts on the former decay are more restrictive. The fit coefficients of the fourth order polynomials used to parameterize the x_F and p_T^2 acceptances are listed in TABLE C.1 in APPENDIX C.

The maximum likelihood method of APPENDIX C was used to simultaneously fit the x_F and p_T^2 distributions of the D_s signal for both resonant decay modes. As in the calculation of the cross sections above, only the E_T(stnd) and E_T(kaon) data were used in the fits. Since the two modes were fit simultaneously in order to increase the statistics in the event sample it was not possible to properly produce a background subtracted, acceptance corrected x_F or p_T^2 distribution. FIGURE 6.5A and 6.5B show the background subtracted, acceptance corrected x_F and p_T^2 distributions as well as the result of the maximum likelihood fit to the data points for all of the E_T(stnd) and E_T(kaon) data for both decay modes combined. The background subtraction in these two figures used the acceptance for the K^*K mode since it dominates the background in the total signal. The results of the maximum likelihood method for the combined pion and kaon beam data as well as for each beam particle type separately is shown in TABLE 6.7. The table lists the n and b of fits to the form $(1-x_F)^n$ and $\exp(-bp_T^2)$. To ensure that the maximum likelihood code was working properly it was tested on fake data generated with known x_F and p_T^2 distribution. The code returned the generated values to within the errors on the fit.

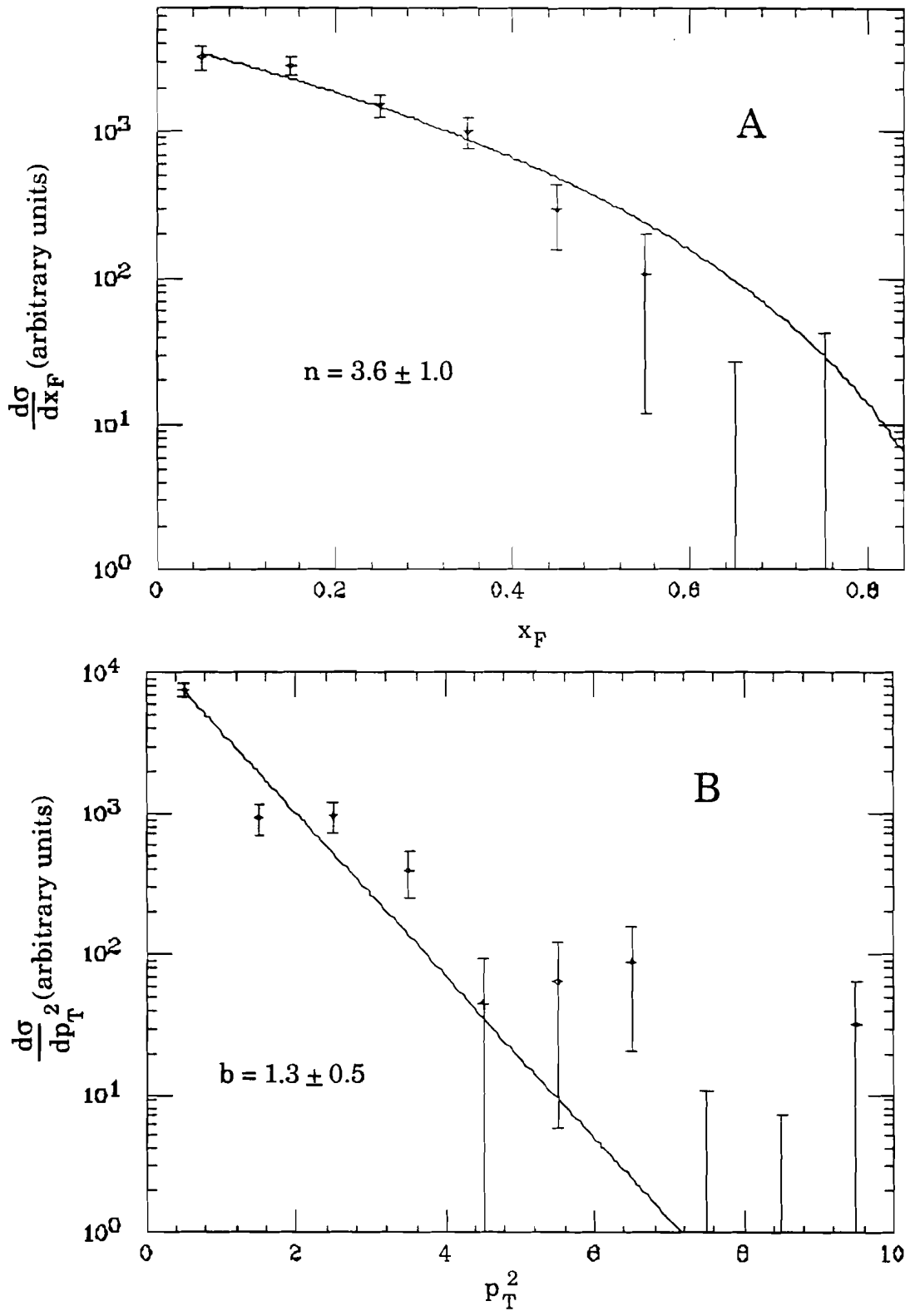

FIGURE 6.5
A) background subtracted, acceptance corrected D_s x_F distribution
B) background subtracted, acceptance corrected D_s p_T^2 distribution

TABLE 6.7
Maximum Likelihood fits to $(1-x_F)^n$ and $\exp(-bp_T^2)$

Beam particle(s)	n (x_F>0.0)	b (GeV^{-2}) (p_T^2<10 GeV^2)
pion + kaon	3.1±1.0	1.1±0.3
pion	3.2±1.2	0.9±0.3
kaon	2.9±1.6	1.3±0.5
proton	7.8±4.1	4.6±4.7

The errors quoted in TABLE 6.7 are statistical only. Recent studies[57] of the systematic error in the measurement of n and b for the D^+ have shown that the systematic errors are about a factor of 4 lower than the errors quoted in the table. We expect that the D^+ systematic errors will be very similar to the D_s systematic errors since both studies are of 3-body decay modes using similar cuts. All of the values of n listed in TABLE 6.7 are consistent with one another as are the values of b in the same table.

The fitted value of n in the pion beam of 3.2±1.2 is in agreement with ACCMOR's measurement (Barlag et al., ref. 54) of 3.94±0.90. The fitted value of b in the pion beam of 0.9±0.3 is also in agreement with their value (Barlag et al., ref. 54) of 0.59±0.10. A recent measurement of the value of n and b for proton production of $D^\pm$ mesons by the WA82 group at CERN[58] gives n=5.5±0.8 and b=0.79±0.08. They have no measurement of the D_s distributions but their results indicate that the proton induced D^+ meson distributions are softer in x_F than the pion induced distributions.

These values should also be compared to the theoretical predictions discussed in Chapter 1 (TABLEs 1.2 and 1.3) and the MC predictions of Chapter 5. In Chapter 1 I

---

57 Zhongxin Wu, Ph.D. Thesis, The Feynman-x dependence of $D^\pm$mesons in $\pi^\pm$-Nucleon Interactions, Yale University, 1991.

58 presented by B. Osculati at the Third Topical Seminar on Heavy Flavours, San Miniato, Italy, 1991.

calculated that the charm quark distribution for the π and K beams should have n=4.5 and 4.6 respectively while b=0.46. The measured values of n for the D_s shown in TABLE 6.7 are consistent with the theoretical values of n for the bare charm quark at the 1σ level. The value of n for π and K beams are consistent with the prediction by the MC for both the bare charm quark (n=4.5) and for the D_s (n=3.8). They are only consistent with the values predicted in Chapter 1 for the D_s after fragmentation at the 2σ level. This may be an indication that, as mentioned in Chapter 1, implementation of the fragmentation outside of the environment of a full MC simulation of the hadronization is inappropriate. It may also indicate that the functions which were used are inappropriate for a hadron beam or the energy range of E769.

Since all the values in the columns of TABLE 6.7 are consistent with one another we see no evidence of any flavour dependence in the differential cross sections for the 3 beams. Since the errors on n and b are much larger than the differences expected due to changes in the form of the kaon's gluon distribution, it is not possible to make a precise measurement of the kaon's gluon structure function. It may be possible, using a simultaneous fit to the cross section and x_F differential distribution for K produced $D^{\pm}$ mesons, to measure the exponent β of the gluons in the kaon.

The values of b predicted by the theory and the MC for the bare charm quark are smaller than those which were measured for the D_s at the $\sim 1\sigma$ level. The measured values in the pion beam are consistent with the value of b=0.67 predicted for the D_s mesons by the E769 MC (see FIGURE 5.7).

Chapter 7: Conclusions

We have measured the $\sigma \times B$, σ, and differential x_F and p_T^2 cross sections for the hadronic production of D_s mesons by π, K and p beams using two resonant decay modes of the D_s: $D_s \rightarrow \phi\pi$ ($\phi \rightarrow KK$) and $D_s \rightarrow K^*K$ ($K^* \rightarrow K\pi$). The $KN \rightarrow D_sX$ sample is the largest single sample of kaon induced D_s events ever obtained, while the proton induced D_s signal is the only such sample in the world.

Our ratio of the K to π D_s cross section, averaged over the two decay modes, is 1.2±0.7 while for the p to π D_s cross section it is 1.0±0.8. These ratios indicate that $\sigma(KN \rightarrow D_sX)/\sigma(\pi N \rightarrow D_sX) < 2.1$ and $\sigma(pN \rightarrow D_sX)/\sigma(\pi N \rightarrow D_sX) < 2.0$ at the 90% confidence limit. The theoretical prediction for both of the ratios for charm quark production is 1.1 as shown in Table 1.1. The theoretical prediction is sensitive to the charm quark mass, renormalization scale and the structure functions for each of the hadrons.

The hadronic cross sections for the production of D_s, averaged over the two decay modes studied, are 1.1±0.5μb, 1.4±0.6μb, and 1.1±0.8μb for the π, K and p beams respectively. The values are for the region $x_F > 0$ and assume an A^1 dependence of the nuclear cross section for better comparison to other experiments. The results are in agreement with other existing measurements of the same quantities. E769 has measured the A dependence of the nuclear cross section for open charm and found that $\sigma \propto \sigma_0 A^{0.95 \pm 0.05}$. This value of the A-dependence implies cross sections of 1.3±0.6μb, 1.6±0.8μb, and 1.3±1.0μb for the π, K and p beams respectively in the same region of x_F.

We have fit the x_F and p_T^2 dependence for the hadronically produced D_s to functions of the form $(1-x_F)^n$ and $\exp(-bp_T^2)$ and find n=3.1±1.0 and b=1.1±0.3 when both decay modes and the pion and kaon data are combined together. The measured n and b for each individual beam particle separately is indistinguishable from the combined measurement. Since the measurements are equal to within the quoted errors there is no evidence of a flavour dependence in the differential cross sections for the three beam particles.

Appendix A

E769 D_S Cross Section Measurement

This Appendix describes the method used to determine the total cross sections (σ) for the production of D_S mesons by the three different types of beam particles. The cross section × branching ratios ($\sigma \times B$) are obtained as a matter of course in the calculation.

The problem is formulated in a matrix notation because this format is particularly well suited to the calculation. Appendix A is broken into two parts. The first covers the basic formulation of the problem while the second covers the detailed calculation of the matrix elements.

Formulation of the E769 Cross Section measurement

The cross section for the production of D_S mesons on a single thin target by an unspecified beam particle is given by:

$$\sigma_{D_s} \equiv \frac{N_{D_s}^{act}}{N^{inc}} \frac{A}{\rho\, N_A\, t}$$

where

A	= molecular weight of target material
ρ	= density of target material
N_A	= the number of Avogadro
t	= thickness of target material
N^{inc}	= number of particles incident on the target
$N_{D_s}^{act}$	= actual number of D_S mesons produced in the target.

If we define $M = \frac{A}{\rho N_A t}$ (M for Material of the target) then the actual number of D_S decays produced in the target is

Appendix A: Formulation of the E769 D_s Cross Section Measurement

$$N_{D_s}^{act} = \frac{1}{M} N_{inc} \sigma_{D_s}$$

If we parametrize the A-dependence of the nuclear cross section by $\sigma = \sigma_o A^{\alpha}$ then, for incident $\pi/K/p$, the actual number of D_S mesons decaying to mode d produced by each particle is given by

$$N_{\pi \to D_s \to d}^{act} = \frac{B_{D_s \to d}}{M} N_{\pi}^{inc} \sigma_o(\pi \to D_s) A^{\alpha_{\pi}^{charm}}$$

$$N_{K \to D_s \to d}^{act} = \frac{B_{D_s \to d}}{M} N_{K}^{inc} \sigma_o(K \to D_s) A^{\alpha_{K}^{charm}}$$

$$N_{p \to D_s \to d}^{act} = \frac{B_{D_s \to d}}{M} N_{p}^{inc} \sigma_o(p \to D_s) A^{\alpha_{p}^{charm}}$$

where

N_i^{inc}	= the real number of incident particles of type i
$N_{i \to D_s \to d}^{act}$	= the real # of $D_S \to d$ decays produced by beam type i
$\sigma_o(i \to D_s)$	= the nucleon cross section for D_S by beam type i
α_i^{charm}	= the alpha value for production of D_S by particle type i
$B_{D_s \to d}$	= Branching ratio of the D_S to mode d

The observed number of D_S ($N_{i \to D_s \to d}^{obs}$) produced by particles of type i decaying into the mode d is related to the actual number by the overall acceptance for this decay mode ($ACC_{i \to D_s \to d}$):

$$N_{i \to D_s \to d}^{obs} = N_{i \to D_s \to d}^{act} ACC_{i \to D_s \to d} = \frac{B_{D_s \to d}}{M} N_i^{inc} \sigma_o(i \to D_s) A^{\alpha_i^{charm}} ACC_{i \to D_s \to d}$$

Unfortunately, we do not know with certainty the identity of every beam particle. Instead, we use $\pi'/K'/p'$ which are admixtures of the real $\pi/K/p$ beam and depend on E769's ability to distinguish between beam particles with the DISC and TRD.

We can determine the number of K' (for instance) on the target ($N_{K'}^{inc}$) and we can also determine the number of $D_S \to d$ decays produced by the K' particles ($N_{K' \to D_S \to d}^{obs}$). Then, define a new set of nine quantities $P(i', j)$ which give the probability that what was

called particle type i' was actually of type j. e.g. $P(K',p)$ is the probability that what was called a kaon was actually a proton. The number of real $\pi/K/p$ in the K' sample is then given by:

$$N^{inc}_{(K',\pi)} = p(K',\pi)N^{inc}_{K'}$$
$$N^{inc}_{(K',K)} = p(K',K)N^{inc}_{K'}$$
$$N^{inc}_{(K',p)} = p(K',p)N^{inc}_{K'}$$

respectively. Using the acceptance for decay mode d of the D_s for each beam particle the observed number of $\pi' \to D_S \to d$ is given by:

$$N^{obs}_{\pi'\to D_s\to d} = \frac{B_{D_s\to d}}{M}\begin{Bmatrix} N^{inc}_{(\pi',\pi)}\sigma_o(\pi\to D_s)A^{\alpha^{charm}_\pi}ACC_{\pi\to D_s\to d} + \\ N^{inc}_{(\pi',K)}\sigma_o(K\to D_s)A^{\alpha^{charm}_K}ACC_{K\to D_s\to d} + \\ N^{inc}_{(\pi',p)}\sigma_o(p\to D_s)A^{\alpha^{charm}_p}ACC_{p\to D_s\to d} \end{Bmatrix}$$

$$= \frac{B_{D_s\to d}}{M}N^{inc}_{\pi'}\begin{Bmatrix} P(\pi',\pi)\sigma_o(\pi\to D_s)A^{\alpha^{charm}_\pi}ACC_{\pi\to D_s\to d} + \\ P(\pi',K)\sigma_o(K\to D_s)A^{\alpha^{charm}_K}ACC_{K\to D_s\to d} + \\ P(\pi',p)\sigma_o(p\to D_s)A^{\alpha^{charm}_p}ACC_{p\to D_s\to d} \end{Bmatrix}$$

Similarly for the K',

$$N^{obs}_{K'\to D_s\to d} = \frac{B_{D_s\to d}}{M}N^{inc}_{K'}\begin{Bmatrix} P(K',\pi)\sigma_o(\pi\to D_s)A^{\alpha^{charm}_\pi}ACC_{\pi\to D_s\to d} + \\ P(K',K)\sigma_o(K\to D_s)A^{\alpha^{charm}_K}ACC_{K\to D_s\to d} + \\ P(K',p)\sigma_o(p\to D_s)A^{\alpha^{charm}_p}ACC_{p\to D_s\to d} \end{Bmatrix}$$

and, obviously, there is a similar equation for the observed number of $p' \to D_S \to d$ decays. We can write these three equations simultaneously in matrix format as:

$$\begin{bmatrix} N^{obs}_{\pi'\to D_s\to d} \\ N^{obs}_{K'\to D_s\to d} \\ N^{obs}_{p'\to D_s\to d} \end{bmatrix} = \frac{B_{D_s\to d}}{M}\times$$

$$\begin{bmatrix} P(\pi',\pi)N^{inc}_{\pi'} & P(\pi',K)N^{inc}_{\pi'} & P(\pi',p)N^{inc}_{\pi'} \\ P(K',\pi)N^{inc}_{K'} & P(K',K)N^{inc}_{K'} & P(K',p)N^{inc}_{K'} \\ P(p',\pi)N^{inc}_{p'} & P(p',K)N^{inc}_{p'} & P(p',p)N^{inc}_{p'} \end{bmatrix}\begin{bmatrix} \sigma_o(\pi\to D_s)A^{\alpha^{charm}_\pi}ACC_{\pi\to D_s\to d} \\ \sigma_o(K\to D_s)A^{\alpha^{charm}_K}ACC_{K\to D_s\to d} \\ \sigma_o(p\to D_s)A^{\alpha^{charm}_p}ACC_{p\to D_s\to d} \end{bmatrix}$$

Appendix A: Formulation of the E769 D_s Cross Section Measurement

The square bracket notation denotes a matrix. We rewrite these matrices in a format which allows us to solve for the D_s cross sections:

$$\begin{bmatrix} \sigma_o(\pi \to D_s) A^{\alpha_\pi^{charm}} ACC_{\pi \to D_s \to d} \\ \sigma_o(K \to D_s) A^{\alpha_K^{charm}} ACC_{K \to D_s \to d} \\ \sigma_o(p \to D_s) A^{\alpha_p^{charm}} ACC_{p \to D_s \to d} \end{bmatrix}$$

$$= \begin{bmatrix} A^{\alpha_\pi^{charm}} & 0 & 0 \\ 0 & A^{\alpha_K^{charm}} & 0 \\ 0 & 0 & A^{\alpha_p^{charm}} \end{bmatrix} \begin{bmatrix} ACC_\pi & 0 & 0 \\ 0 & ACC_K & 0 \\ 0 & 0 & ACC_p \end{bmatrix} \begin{bmatrix} \sigma_o(\pi) \\ \sigma_o(K) \\ \sigma_o(p) \end{bmatrix}$$

$$\equiv \left[\alpha^{charm}\right]\left[ACC\right]\left[\sigma_o\right]$$

and

$$\begin{bmatrix} N_{\pi'}^{obs} \\ N_{K'}^{obs} \\ N_{p'}^{obs} \end{bmatrix} \equiv \left[N'_{obs}\right]$$

and

$$\begin{bmatrix} P(\pi',\pi)N_{\pi'}^{inc} & P(\pi',K)N_{\pi'}^{inc} & P(\pi',p)N_{\pi'}^{inc} \\ P(K',\pi)N_{K'}^{inc} & P(K',K)N_{K'}^{inc} & P(K',p)N_{K'}^{inc} \\ P(p',\pi)N_{p'}^{inc} & P(p',K)N_{p'}^{inc} & P(p',p)N_{p'}^{inc} \end{bmatrix}$$

$$= N_{\pi'}^{inc} \begin{bmatrix} P(\pi',\pi) & P(\pi',K) & P(\pi',p) \\ 0 & 0 & 0 \\ 0 & 0 & 0 \end{bmatrix}$$

$$+ N_{K'}^{inc} \begin{bmatrix} 0 & 0 & 0 \\ P(K',\pi) & P(K',K) & P(K',p) \\ 0 & 0 & 0 \end{bmatrix}$$

$$+ N_{p'}^{inc} \begin{bmatrix} 0 & 0 & 0 \\ 0 & 0 & 0 \\ P(p',\pi) & P(p',K) & P(p',p) \end{bmatrix}$$

$$\equiv N_{\pi'}^{inc}\left[P_{\pi'}\right] + N_{K'}^{inc}\left[P_{K'}\right] + N_{p'}^{inc}\left[P_{p'}\right]$$

where the amount of information in the sub-scripts has been reduced in a straightforward manner.

Using the above notation we can write

$$[N'_{obs}] = \frac{B_{D_s \to d}}{M}\left\{N^{inc}_{\pi'}[P_{\pi'}] + N^{inc}_{K'}[P_{K'}] + N^{inc}_{p'}[P_{p'}]\right\}[\alpha^{charm}][ACC][\sigma_o]$$
$$\equiv \frac{B_{D_s \to d}}{M}[NP][\alpha^{charm}][ACC][\sigma_o]$$

Which can be inverted for $[\sigma_O]$:

$$[\sigma_o] = \frac{M}{B_{D_s \to d}}[ACC]^{-1}[\alpha^{charm}]^{-1}[NP]^{-1}[N'_{obs}]$$

Since $[ACC]$ is a diagonal matrix its inverse is given simply by:

$$[ACC]^{-1} = \begin{bmatrix} ACC_\pi^{-1} & 0 & 0 \\ 0 & ACC_K^{-1} & 0 \\ 0 & 0 & ACC_p^{-1} \end{bmatrix}$$

and similarly for $[\alpha^{charm}]^{-1}$

$$[\alpha^{charm}]^{-1} = \begin{bmatrix} A^{-\alpha_\pi^{charm}} & 0 & 0 \\ 0 & A^{-\alpha_K^{charm}} & 0 \\ 0 & 0 & A^{-\alpha_p^{charm}} \end{bmatrix}$$

The inverse of the [NP] matrix is not so trivial. The derivation of the elements of this matrix is left for the second part of this Appendix.

We are left with a set of three equations which must be solved in order to determine the D_s cross section for each of the three different types of beam particles. This equation applies only to a single, thin target. All of the terms on the RHS of the equation for $[\sigma_O]$ are either known or calculable. $[N'_{obs}]$ is given simply by fits to the D_s distributions to the $i' \to D_S$ histograms. The three probability matrices, $[P_{\pi'}]$, $[P_{K'}]$, and $[P_{p'}]$ are all derivable from the details of the DISC and TRD operation. The number of incident 'pion', 'kaon', and 'proton' particles is calculated from the scaler event records in combination with the DISC and TRD information for each spill and run. These will be specified in detail in the second part of this Appendix.

These equations may be generalized to allow for multiple targets (foils or regions) over which we can average or sum the answers for each individual target. For an individual target (T), which may be a single foil or a group of foils of the same type of material,

$$[\sigma_o] = \frac{M(T)}{B_{D_s \to d}} [ACC(T)]^{-1} [\alpha^{charm}(T)]^{-1} [NP(T)]^{-1} [N'_{obs}(T)]$$

This equation indicates that the nucleon cross sections, type of material, atomic weight, acceptance, number of incident particles of each type and observed number of D_s decays may vary with each target region. The elements of the $M(T)$, $ACC(T)$, $\alpha(T)$ and $N'_{obs}(T)$ matrices are all calculable in the same way for each different target region. The elements of the $NP(T)$ matrix are slightly more complicated in appearance due to the different inelastic nucleon cross sections for pions, kaons and protons.

Interactions upstream of the target in question may reduce the actual number of particles impinging on the target compared to the number expected from the scintillator arrangement around the target region (TRDGB). The number of particles incident on the target assembly is not merely TRDGB (which requires a pulse in the scintillators near the TRD, a Beam Spot pulse and no Halo pulse) because of interactions upstream of the target. This effect is discussed in detail in Appendix A: Correcting TRDGB for upstream interactions.

Recall that

$$\sigma^{in} \equiv \frac{N^{in}}{N^{inc}} \frac{A}{\rho N_A t} \equiv \sigma_o^{in} A^{\alpha^{in}}$$

where σ^{in} is the inelastic cross section, N^{in} is the number of inelastic interactions in the material and the other variables are as defined above. We use the inelastic cross section since the elastic reactions scatter predominantly forward with almost no loss of momentum and therefore do not reduce the number of particles available to produce D_s.

The inelastic and total nucleon cross sections have been calculated[59] at our beam energy (250GeV) and are shown in Table A.1. Since there is very little difference between the proton, neutron and one-half the deuteron cross sections we use the proton inelastic cross section for all future measurements.

TABLE A.1
Inelastic and Total Nucleon Cross Sections at 250 GeV

	Target Particle		
Incident Particle	Proton† Inelastic σ (mb) /Total σ (mb)	Neutron† Inelastic σ (mb) /Total σ (mb)	Deuteron† Inelastic σ (mb) /Total σ (mb)
π^-	21.2 / 24.7	NA	NA / 46.8
π^+	20.9 / 24.2	NA	NA / 46.7
K^-	18.5 / 21.3	NA / 11.7	NA / 40.5
K^+	17.2 / 19.9	NA / 20.3	NA / 39.5
p^-	34.8 / 41.8	NA / 37.6	NA / 77.8
p^+	32.4 / 39.3	NA / 39.6	NA / 74.6

† No errors quoted because the errors on the fit to the cross sections are highly correlated.

The number of incident particles which pass unheeded to the target in question is simply

$$N^{pass} = N^{inc} - N^{in} = N^{inc}\left(1 - \frac{A^{\alpha^{in}}\sigma_o^{in}}{M}\right)$$

where M is as defined above. If we let A_i and M_i be the atomic number and $\frac{A}{\rho N_A t}$ of foil i respectively the number of particles incident on each foil (f) is given by:

$$N_f^{inc} = N^{inc}\prod_{i=1}^{f-1}\left(1 - \frac{A_i^{\alpha^{in}}\sigma_o^{in}}{M_i}\right)$$

59 M. Aguilar-Benitez et al., The Particle Data Group, 1990 Review of Particle Properties, Physics Letters B239, p. III.77.

for $f>1$. The correction to the number of particles incident on the first foil was implemented as a small decrease in TRDGB as described later. The number of real pions incident on foil f is then given by

$$\left(N_{\pi}^{inc}\right)_f = P(\pi',\pi)N_{\pi'}^{inc}\prod_{i=1}^{f-1}\left(1-\frac{A_i^{\alpha_\pi^{in}}\sigma_o^{in}(\pi)}{M_i}\right)$$

for $f>1$. The inelastic nucleon cross section for pions is used for the pion beam. The α value to be used here to account for the A-dependence of the cross section is for pion induced minimum bias or all inelastic events. Various target and foil properties as well as the reduction of the π/K/p beams to each individual foil have been tabulated in Table B.1 found in Appendix B which discusses systematic errors in these cross sections.

Even the higher statistics in the D^0 and $D^{\pm}$ decay mode do not warrant breaking the signal into different target foils but only into different target regions defined by the type of material in the foil. Statistics in the D_s and Λ_c decays are low enough to require summing over the entire target and assuming that the A-dependence measured in the charged and neutral D decay modes is applicable to the other charmed particles.

In each of the targets (T) there is a reduction $R_i(T)$ in the number of incident beam particles from that counted by TRDGB as described above. This reduction varies with beam particle type i because of the different inelastic cross sections for each particle. $R_i(T)$ may be the average of the reduction in particles to the first foil of the region and the reduction in particles to the last foil of the region. This correction is implemented in the cross section calculation by introducing a reduction matrix given by:

$$[R(T)] = \begin{bmatrix} R_\pi(T) & 0 & 0 \\ 0 & R_K(T) & 0 \\ 0 & 0 & R_p(T) \end{bmatrix}$$

such that

$$[NP(T)] \rightarrow [NP][R(T)]$$

and then

$$[N'_{obs}(T)] = \frac{B_{D_s \to d}}{M(T)}[NP][R(T)][\alpha^{charm}(T)][ACC(T)][\sigma_o]$$

For low statistics signals such as the D_S we must sum over the entire E769 target before solving for the nucleon cross sections:

$$\sum_T [N'_{obs}(T)] = B_{D_s \to d}[NP]\left\{\sum_T \frac{1}{M(T)}[R(T)][\alpha^{charm}(T)][ACC(T)]\right\}[\sigma_o]$$

If

$$\left\{\sum_T \frac{1}{M(T)}[R(T)][\alpha^{charm}(T)][ACC(T)]\right\} \equiv \left[\sum \frac{R \bullet A^{\alpha} \bullet ACC}{M}\right]$$

which is a diagonal matrix and

$$\sum_T [N'_{obs}(T)] \equiv [N'_{obs}]^{tot}$$

which is clearly the total D_S signal due to each of the three incident beam particles then the nucleon cross sections are given by:

$$[\sigma_o] = \frac{1}{B_{D_s \to d}}\left[\sum \frac{R \bullet A^{\alpha} \bullet ACC}{M}\right]^{-1}[NP]^{-1}[N'_{obs}]^{tot}$$

The real difficulty lies in the determination of the number of incident $\pi'/K'/p'$ on each of the different targets and even more so in the determination of the contamination (*P* matrix) in these beams.

Detailed calculation of the elements of the Probability Matrices

The rest of Appendix A describes the exact method used in calculating the number of incident particles of each type.

Calculation of the corrected beam particle ratios for NON-DISC tagged beam

If f_{i^-} is the *a priori* beam probability for particle type i in the negative beam and ε_i^{DISC} is the DISC efficiency for the same particle type in a given run/spill then, AFTER the DISC tagging, the beam composition ratio in the NON-DISC tagged beam is given by:

$$N_{\pi}^{NODISC}:N_K^{NODISC}:N_p^{NODISC} = (1-\varepsilon_{\pi}^{DISC})f_{\pi}:(1-\varepsilon_K^{DISC})f_K:(1-\varepsilon_p^{DISC})f_p$$

Appendix A: Calculation of the beam particle ratios for NON-DISC tagged beam

The particles which were not DISC tagged were prescaled by the same prescaler. Therefore, the fraction of the negative beam composed of beam particle type i after DISC tagging is given by f'_i :

$$f'_{\pi^-} = \frac{(1-\varepsilon_\pi^{DISC})f_{\pi^-}}{S^-}, \qquad f'_{K^-} = \frac{(1-\varepsilon_K^{DISC})f_{K^-}}{S^-}, \qquad f'_{p^-} = \frac{(1-\varepsilon_p^{DISC})f_{p^-}}{S^-}$$

where

$$\begin{aligned} S^- &\equiv \sum_{i=1}^{3}(1-\varepsilon_i^{DISC})f_i \\ &= (1-\varepsilon_\pi^{DISC})f_{\pi^-} + (1-\varepsilon_K^{DISC})f_{K^-} + (1-\varepsilon_p^{DISC})f_{p^-} \\ &= 1-\sum_{i=1}^{3}\varepsilon_i^{DISC}f_i \end{aligned}$$

A similar set of equations apply for the positive beam.

Calculation of the number of incident $\pi'/K'/p'$

First, we calculate the number of incident particles on the first foil of the target. The NODISC subscript indicates spills when the DISC was not set to tag the particle of interest. The DISC subscript is for spills in which the DISC pressure and temperature were set correctly to tag the particle with which we are concerned and the DISC probability for the particle was greater than some suitable cut on the probability (normally 0.9). For pions,

$$(N_{\pi'})^{inc} = (N_{\pi'}^-)^{inc} + (N_{\pi'}^+)^{inc}$$

$$\begin{aligned} (N_{\pi'}^-)^{inc} &= (N_{\pi'}^-)^{inc}_{NODISC} + (N_{\pi'}^-)^{inc}_{DISC} \\ &= \sum_{-spills}^{DISC_\pi<CUT_\pi} TRDGB \bullet \overline{FOLD4} \times \frac{F_{live}}{PS} \\ &+ \sum_{-spills}^{DISC_\pi>CUT_\pi} TRDGB \bullet FOLD4 \times F_{live} \end{aligned}$$

$$(N^{+}_{\pi'})^{inc} = (N^{+}_{\pi'})^{inc}_{NODISC} + (N^{+}_{\pi'})^{inc}_{DISC}$$

$$= \sum_{+spills}^{DISC_{\pi}<CUT_{\pi}} TRDGB \bullet \overline{FOLD4} \times f'_{\pi^{+}} \times \frac{F_{live}}{PS} \times \varepsilon_{\pi}^{TRD}$$

$$+ \sum_{+spills}^{DISC_{\pi}>CUT_{\pi}} TRDGB \bullet FOLD4 \times F_{live}$$

for Kaons,

$$N^{inc}_{K'} = \sum_{All\ spills}^{DISC_{K}>CUT_{K}} TRDGB \bullet FOLD4 \times F_{live}$$

and for protons,

$$N^{inc}_{p'} = \left(N^{-}_{p'}\right)^{inc} + \left(N^{+}_{p'}\right)^{inc}$$

$$\left(N^{-}_{p'}\right)^{inc} = \sum_{-spills}^{DISC_{p}>CUT_{p}} TRDGB \bullet FOLD4 \times F_{live}$$

$$\left(N^{+}_{p'}\right)^{inc} = \left(N^{+}_{p'}\right)^{inc}_{NODISC} + \left(N^{+}_{p'}\right)^{inc}_{DISC}$$

$$= \sum_{+spills}^{DISC_{p}<CUT_{p}} TRDGB \bullet \overline{FOLD4} \times f'_{p^{+}} \times \frac{F_{live}}{PS} \times \varepsilon_{p}^{TRD}$$

$$+ \sum_{+spills}^{DISC_{p}>CUT_{p}} TRDGB \bullet FOLD4 \times F_{live}$$

where

TRDGB =	scaled value of the TRD Good Beam counter corrected for upstream interactions and multi-particle bucket occupancy
TRDGB•FOLD4 =	the scaled value of DISC 4-fold coincidences gated with *TRDGB* corrected for upstream interactions and multi-particle bucket occupancy
F_{live} =	the fractional live time of the experiment given by the ratio of two scalers - INT(PS) / INT. The live time must be modified for some runs due to the Killer Bit.
PS =	the E_T prescaler setting for each spill - also given by the ratio of two scalers - TRDGB / PIP. For cross sections using the E_T(high) triggers the prescaler was calculated as PI / TRDGB.

Appendix A: Calculation of the number of incident $\pi'/K'/p'$

$DISC_i$ =	DISC probability for particle type i
CUT_i^j =	the cut on the DISC probability for particle type i in beam polarity j
ε_i^{TRD} =	the TRD efficiency for particle type i when a cut is made on the probability for particle type i at CUT_i
f'_{i^-} =	beam fraction for particle type i under negative beam conditions corrected for DISC tagging efficiency

$TRDGB \bullet FOLD4$ was scaled directly. $TRDGB \bullet \overline{FOLD4}$ was given by $TRDGB - TRDGB \bullet FOLD4$.

Correcting TRDGB for Upstream Interactions

Inelastic interactions upstream of the target could produce an interaction trigger if at least five of the products of the interaction passed through the Beam Spot Scintillator and the interaction scintillator and no particles passed through the Halo counter. These TRDGB counts should not be included when calculating the normalizations for the cross sections. Elastic interactions upstream of the target were of little concern since these reactions preserve the identity and energy of the beam particle in the forward direction.

A sample of interaction trigger events were manually examined to determine whether the event was due to an interaction in the target or upstream of the target. About 15±5% of these triggers were from upstream interactions. Thus,

$$\frac{N^{INT}_{upstream}}{N^{INT}_{target}} = \frac{N_{upstream}}{N_{target}} \frac{\varepsilon^{INT}_{upstream}}{\varepsilon^{INT}_{target}} = 0.18 \pm 0.07$$

where $N^{INT}_{upstream}$ and N^{INT}_{target} refer to the number of interaction triggers caused by upstream and target interactions respectively, $N_{upstream}$ and N_{target} represent the actual number of interactions upstream of and in the target respectively, $\varepsilon^{INT}_{upstream}$ and $\varepsilon^{INT}_{target}$ are the efficiencies for the interactions in the two regions to produce an interaction trigger.

Dividing both sides of this equation by TRDGB gives the fraction of TRDGB which interacts upstream of the target relative to the fraction which interacts in the target and still manages to pass the interaction trigger:

$$f_{upstream} = (0.18 \pm 0.07) f_{target} \frac{\varepsilon_{target}^{INT}}{\varepsilon_{upstream}^{INT}}$$

For protons the interaction length of the target is ~2.1% so that f_{target}=0.021 and therefore:

$$f_{upstream} = (3.8 \pm 1.5) \times 10^{-3} \frac{\varepsilon_{target}^{INT}}{\varepsilon_{upstream}^{INT}}$$

From the geometry of the target region we expect that

$$\frac{\varepsilon_{target}^{INT}}{\varepsilon_{upstream}^{INT}} >> 1$$

and therefore using a value of 1 yields a lower limit of $(3.8\pm1.5)\times10^{-3}$ for the fraction.

An upper limit to the fraction was determined assuming that the efficiency for triggering on upstream interactions was 100%. In this case all interactions in the material just upstream of the target would be written to tape. These materials, along with their thicknesses and interaction lengths, are shown in TABLE A.2.

The upper limit to the fraction of TRDGB which could interact upstream of the target was $(6.2\pm0.3)\times10^{-3}$. This implies that the lower limit to the interaction trigger efficiency for upstream interactions was a surprisingly high 0.61±0.24. Since this correction was so small the final correction to TRDGB was TRDGB→TRDGB(1-0.006±0.003) for protons. Since kaons and pions have inelastic cross sections about 3/5 of that for protons at 250GeV a slightly different correction of TRDGB→TRDGB(1-0.003±0.002) was used for these particles.

TABLE A.2
Materials and Interaction Lengths Upstream of the target

Material	Density[60] (gm/cm^3)	Nuclear Interaction Length[68] (gm/cm^2)	Thickness (cm)	Fraction of an Interaction Length
2 Si planes	2.33	106.0	0.06	0.0013
Beam Spot Scintillator	1.032	82.0	0.267	0.0034
Beam pipe window†[61]	7.87	131.9	0.008	0.0005
Air	0.0012	90.0	75±25	0.0010±0.0003
Total				0.0062±0.0003

† values are for Fe

Correcting TRDGB for multi-particle bucket occupancy and KB Livetime

E769 introduced the 'Killer Bit' starting at Run 1773. The Killer Bit inhibited writing to

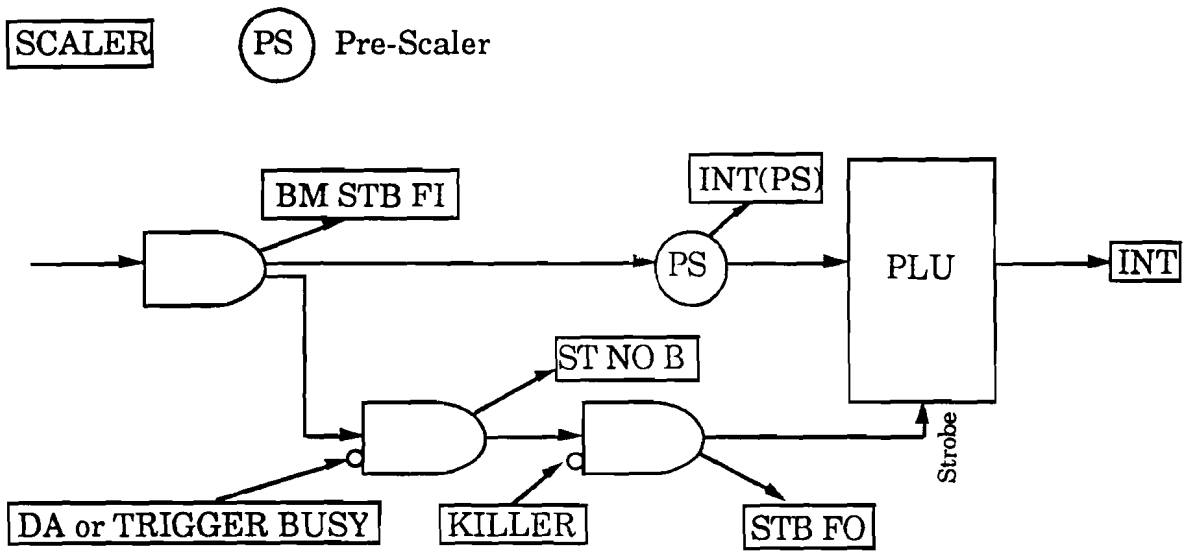

FIGURE A.1
Schematic view of the Scaler system applicable to Livetime calculations

60 Particle Data Group, Review of Particle Properties, Vol. 239, p.III.5, 1990.
61 Carey Kendziora, FNAL Accelerator Division, personal correspondence.

tape any interaction for which another beam particle was present within ±150ns (at 19ns/bucket this corresponds to about ±7 buckets). It was implemented to eliminate contamination of the TRD signals which had a long gate time. This effectively introduced a new source of deadtime into the trigger system beyond the deadtime due to the trigger and the DA system.

From its inception to Run 1850 the Killer Bit was implemented directly in the trigger logic after which it was implemented as a bit in the Trigger PLU and required for some triggers. A schematic view of the scaler system showing only the components relative to the livetime calculations is shown in FIGURE A.1. It shows the Killer Bit implemented in the trigger logic directly. The diagram shows that in this configuration there were two separate methods for calculating the livetime:

$$LIVETIME_1 \equiv \frac{INT}{INT(PS)}$$

$$LIVETIME_2 \equiv \frac{STBFO}{BMSTBFI}$$

where the second calculation is the product of two different livetimes due to the DA (and trigger system) and the Killer Bit given by:

$$LIVETIME_{DA} \equiv \frac{STNOB}{BMSTBFI}$$

$$LIVETIME_{KILLER} \equiv \frac{STBFO}{STNOB}$$

$$LIVETIME_2 = LIVETIME_{DA} \times LIVETIME_{KILLER}$$

During most of the run the two livetime calculations agreed perfectly. The difference between the two calculations correctly indicated the period during which the Killer Bit was implemented in the trigger logic. During this time the first calculation gives the correct livetime. During one other short period of time a small problem in the trigger logic also caused a difference between the two ratios. In this instance $LIVETIME_1$ gave the correct

livetime once again. Thus, $LIVETIME_1$ was used exclusively for the calculation. However, it must still be corrected for the effect of the Killer Bit after Run 1850. The effective livetime for these runs was given by:

$$LIVETIME_{EFF} = LIVETIME_1 \times LIVETIME_{KILLER}(TRDGB)$$

where it has been explicitly indicated that the livetime introduced by the Killer Bit is a function of the beam rate or, equivalently, TRDGB. The calculated value of $LIVETIME_{KILLER}$ is shown plotted versus TRDGB in FIGURE A.2.

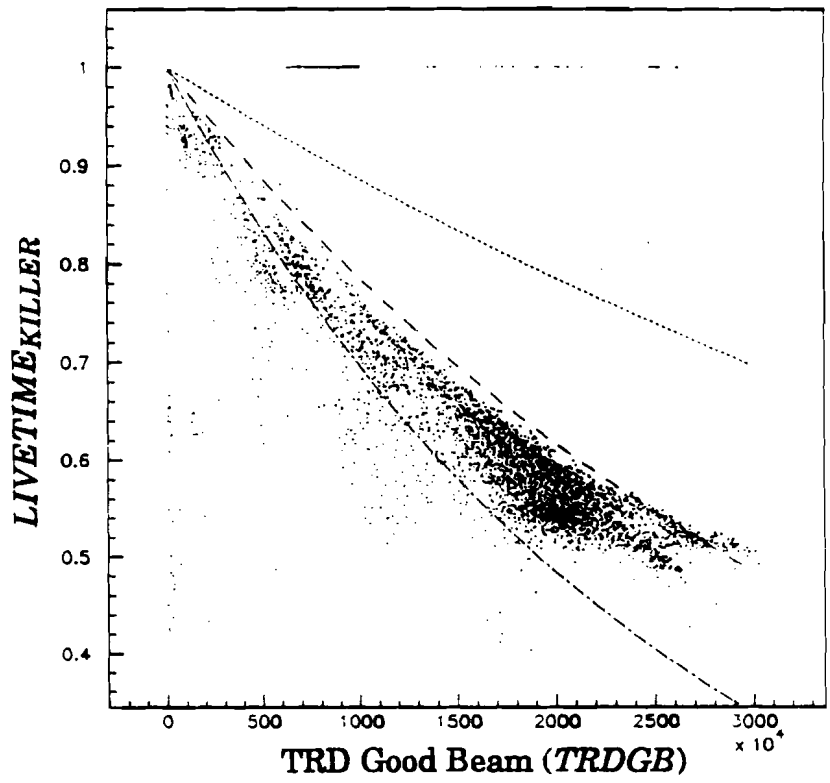

FIGURE A.2
$LIVETIME_{KILLER}$ as a function of TRDGB (beam rate)

The plot also shows the theoretical effect of the Killer Bit assuming that the TRDGB particles were distributed evenly throughout the 22 second spill and obeyed Poisson statistics. In this case the probability that a single bucket contains n particles is simply:

$$P(n) = \frac{\mu^n e^{-\mu}}{n!}$$

where μ is the mean bucket occupancy given by μ = TRDGB(particles/spill) / 22×10^9(ns/spill) × 19(ns/bucket) = TRDGB × 8.6×10^{-10}. A target interaction was not killed by the killer bit if there were no beam particles within ±7 buckets of the interacting particle but the killer bit could not distinguish between multiple particles in the bucket in which the interaction occured. Therefore, the probability that an interaction would not be killed is given by:

$$\begin{aligned} P_{NOKILLER} &= P(0)^7 \left(\sum_{n=1}^{\infty} P(n) \right) P(0)^7 \\ &= e^{-14\mu}(1-e^{-\mu}) \end{aligned}$$

while the probability that an interaction would be killed is given by:

$$\begin{aligned} P_{KILLER} &= (1-P(0)^{14}) \left(\sum_{n=1}^{\infty} P(n) \right) \\ &= (1-e^{-14\mu})(1-e^{-\mu}) \end{aligned}$$

Finally, the fraction of events which were not killed by the Killer Bit assuming a Poisson distributed beam is:

$$\begin{aligned} F_{NOKILLER} &= \frac{P_{NOKILLER}}{P_{NOKILLER} + P_{KILLER}} \\ &= e^{-14\mu} \end{aligned}$$

The highest curve in FIGURE A.2 is the function $e^{-14\mu}$ while the next two curves show the prediction if the beam actually had a bucket occupancy probability of 2μ and 3μ respectively. This measurement indicates that the actual bucket occupancy probability is about 2.5±0.5 times the occupancy rate expected from Poisson statistics for a given TRDGB. Since TRDGB counts only once per occupied bucket even though there may be more than one particle in the bucket we must correct TRDGB to give us the actual number of particles incident on the target. The correction is simply TRDGB→TRDGB×(1+2.5±0.5μ).

Appendix A: Correcting TRDGB for Upstream Interactions

This correction does not allow for 'super-buckets' in which perhaps tens of particles occupy the same bucket. These super-buckets are little-understood glitches in the operation of the accelerator and occur at an unknown but small frequency. There effect on this calculation is expected to be small.

Calculation of the contamination of the K' beam

It is relatively simple to calculate the K' elements (the elements of the second row) of the Probability matrix since only the DISC was able to tag kaons and it was used in both beam polarities. Recall that:

$$N_{K'}^{inc} = \sum_{All\ spills}^{DISC_K > CUT_K} TRDGB \bullet FOLD4 \times F_{live}$$

where $DISC_i$ is the probability reported by the DISC for particle type i for a given run/spill. Then, of the $N_{K'}^{inc}$ particles the number of these which were actually pions is given by:

$$N_{(K',\pi)}^{inc} = \sum_{All\ spills}^{DISC_K > CUT_K} TRDGB \bullet FOLD4 \times F_{live} \times DISC_\pi$$

and the number which were actually kaons and protons is given by:

$$N_{(K',K)}^{inc} = \sum_{All\ spills}^{DISC_K > CUT_K} TRDGB \bullet FOLD4 \times F_{live} \times DISC_K$$

$$N_{(K',p)}^{inc} = \sum_{All\ spills}^{DISC_K > CUT_K} TRDGB \bullet FOLD4 \times F_{live} \times DISC_p$$

respectively. Similar equations will apply to the proton and pion samples when the DISC is used to tag these beam particles. The probability elements are then simply:

$$P(K',\pi) = \frac{N_{(K',\pi)}^{inc}}{N_{K'}^{inc}}, \qquad P(K',K) = \frac{N_{(K',K)}^{inc}}{N_{K'}^{inc}}, \qquad P(K',p) = \frac{N_{(K',p)}^{inc}}{N_{K'}^{inc}}.$$

Calculation of the contamination of the π' beam

Now consider the case of non-DISC tagged π in the negative beam. Recall that:

$$(N^{-}_{\pi'})^{inc}_{NODISC} = \sum_{-spills}^{DISC_{\pi}<CUT^{-}_{\pi}} TRDGB \bullet \overline{FOLD4} \times \frac{F_{live}}{PS}$$

Where it was assumed that everything which was not DISC tagged was a pion. Since the non-DISC tagged negative beam was not tagged in any other manner the number of real $\pi/K/p$ in the negative π' beam is given by:

$$(N^{-}_{(\pi',\pi)})^{inc}_{NODISC} = \sum_{-spills}^{DISC_{\pi}<CUT^{-}_{\pi}} TRDGB \bullet \overline{FOLD4} \times \frac{F_{live}}{PS} \times f'_{\pi^-}$$

$$(N^{-}_{(\pi',K)})^{inc}_{NODISC} = \sum_{-spills}^{DISC_{\pi}<CUT^{-}_{\pi}} TRDGB \bullet \overline{FOLD4} \times \frac{F_{live}}{PS} \times f'_{K^-}$$

$$(N^{-}_{(\pi',p)})^{inc}_{NODISC} = \sum_{-spills}^{DISC_{\pi}<CUT^{-}_{\pi}} TRDGB \bullet \overline{FOLD4} \times \frac{F_{live}}{PS} \times f'_{p^-}$$

In the positive non-DISC tagged π' beam which had TRD information recall that the number of incident π' is given by:

$$(N^{+}_{\pi'})^{inc}_{NODISC} = \sum_{+spills}^{DISC_{\pi}<CUT^{+}_{\pi}} TRDGB \bullet \overline{FOLD4} \times f'_{\pi^+} \times \frac{F_{live}}{PS} \times \varepsilon^{TRD}_{\pi}$$

The TRD alone separates pions from non-pions ($\overline{\pi}$ = K and p) with no explicit information on what fraction of the non-pion signal was kaon (although most of it is proton). We let C^{TRD}_{π} be the contamination of the TRD pion signal by the other two particles. It is very important to realize that the fitted TRD distributions were filled from events on tape. This means that the E_T trigger was also in effect when filling these distributions. Thus, C^{TRD}_{π} is the contamination by the non-pion beam particles in the TRD pion *signal* which is NOT the same as the contamination of the non-pion beam particles in the pion beam. This is due to the differences in the total cross sections for the three different beam particles and the possibility that the interactions due to the different particles may produce E_T triggers with different probability. If we assume that the K and p TRD distributions were identical in shape and position (not exactly true) and differed only in their

normalizations, then the fraction of the K and p beams which appear in the pion signal is $0.97C_{\pi}^{TRD}\varepsilon_{\pi}^{TRD}$. This number is the TRD efficiency for tagging protons and kaons when we make the cut on the pion probability. The number of protons in the π' beam is then:

$$(N^{+}_{(\pi',p)})^{inc}_{NODISC} = \sum_{+spills}^{DISC_{\pi}<CUT_{\pi}^{*}} TRDGB \bullet \overline{FOLD4} \times f'_{p^{+}} \times \frac{F_{live}}{PS} \times 0.97 \times \varepsilon_{\pi}^{TRD} \times C_{\pi}^{TRD}$$

and the number of kaons in the π' beam is:

$$(N^{+}_{(\pi',K)})^{inc}_{NODISC} = \sum_{+spills}^{DISC_{\pi}<CUT_{\pi}^{*}} TRDGB \bullet \overline{FOLD4} \times f'_{K^{+}} \times \frac{F_{live}}{PS} \times 0.97 \times \varepsilon_{\pi}^{TRD} \times C_{\pi}^{TRD}$$

and the number of real pions in the non-DISC tagged (TRD tagged) positive beam is given by:

$$\begin{aligned}(N^{+}_{(\pi',\pi)})^{inc}_{NODISC} &= (N^{+}_{\pi'})^{inc}_{NODISC} - (N^{+}_{(\pi',\bar{\pi})})^{inc}_{NODISC} \\ &= \sum_{+spills}^{DISC_{\pi}<CUT_{\pi}^{*}} TRDGB \bullet \overline{FOLD4} \times \frac{F_{live}}{PS} \times \varepsilon_{\pi}^{TRD} \times (f'_{\pi^{+}} - 0.97(f'_{K^{+}} + f'_{p^{+}})C_{\pi}^{TRD})\end{aligned}$$

For the DISC tagged pion beam the contamination of the π'signal is given in a similar manner to that given above for the contamination in the K'beam:

$$(N_{(\pi',\pi)})^{inc}_{DISC} = \sum_{All\ spills}^{DISC_{\pi}>CUT_{\pi}} TRDGB \bullet FOLD4 \times F_{live} \times DISC_{\pi}$$

$$(N_{(\pi',K)})^{inc}_{DISC} = \sum_{All\ spills}^{DISC_{\pi}>CUT_{\pi}} TRDGB \bullet FOLD4 \times F_{live} \times DISC_{K}$$

$$(N_{(\pi',p)})^{inc}_{DISC} = \sum_{All\ spills}^{DISC_{\pi}>CUT_{\pi}} TRDGB \bullet FOLD4 \times F_{live} \times DISC_{p}$$

where the summation is over ALL spills and the appropriate cuts for negative and positive beams must be used in the sum.

Therefore, the probability values for the first row of the probability matrix become:

$$P(\pi',\pi)=\frac{(N^{-}_{(\pi',\pi)})^{inc}_{NODISC}+(N^{+}_{(\pi',\pi)})^{inc}_{NODISC}+(N_{(\pi',\pi)})^{inc}_{DISC}}{N^{inc}_{\pi'}}$$

$$P(\pi',K)=\frac{(N^{-}_{(\pi',K)})^{inc}_{NODISC}+(N^{+}_{(\pi',K)})^{inc}_{NODISC}+(N_{(\pi',K)})^{inc}_{DISC}}{N^{inc}_{\pi'}}$$

$$P(\pi',p)=\frac{(N^{-}_{(\pi',p)})^{inc}_{NODISC}+(N^{+}_{(\pi',p)})^{inc}_{NODISC}+(N_{(\pi',p)})^{inc}_{DISC}}{N^{inc}_{\pi'}}$$

Calculation of the contamination of the p' beam

For the DISC tagged proton beam the real number of $\pi/K/p$ in the p' sample is given by:

$$(N_{(p',\pi)})^{inc}_{DISC}=\sum_{All\ spills}^{DISC_p>CUT_p} TRDGB\bullet FOLD4\times F_{live}\times DISC_{\pi}$$

$$(N_{(p',K)})^{inc}_{DISC}=\sum_{All\ spills}^{DISC_p>CUT_p} TRDGB\bullet FOLD4\times F_{live}\times DISC_{K}$$

$$(N_{(p',p)})^{inc}_{DISC}=\sum_{All\ spills}^{DISC_p>CUT_p} TRDGB\bullet FOLD4\times F_{live}\times DISC_{p}$$

exactly as was done for the K' and π' beam.

For the positive data with NO DISC tag but with TRD information:

$$(N^{+}_{(p',\pi)})^{inc}_{NODISC}=\sum_{+spills}^{DISC_p<CUT^{+}_p} TRDGB\bullet\overline{FOLD4}\times f'_{\pi'}\times\frac{F_{live}}{PS}\times 1.03\times\varepsilon^{TRD}_{p}\times C^{TRD}_{p}$$

where the factor of $1.03C^{TRD}_{p}\varepsilon^{TRD}_{p}$ is actually the efficiency for tagging pions when a cut is made on the TRD proton signal. The number of non-pions in the p' signal is simply:

$$(N^{+}_{(p',\bar{\pi})})^{inc}_{NODISC}=(N^{+}_{p'})^{inc}_{NODISC}-(N^{+}_{(p',\pi)})^{inc}_{NODISC}$$
$$=\sum_{+spills}^{DISC_p<CUT^{+}_p} TRDGB\bullet\overline{FOLD4}\times\frac{F_{live}}{PS}\times\varepsilon^{TRD}_{p}\times(f'_{p'}-1.03\times f'_{\pi'}\times C^{TRD}_{p})$$

$\bar{\pi}$ refers to non-pions rather than anti-pions. Since the shape of the TRD K and p distributions are assumed to be identical the efficiency for accepting K and p with the cut on

the proton probability are identical. The ratio of K to p in this non-pion NODISC p' signal is simply $f'_K:f'_p$ which implies that the fraction of the non-pion signal which is Kaon is actually $\frac{f'_K}{f'_K+f'_p}$:

$$(N^{+}_{(p',K)})^{inc}_{NODISC} = \sum_{+spills}^{DISC_p<CUT_p^+} TRDGB \bullet \overline{FOLD4} \times \frac{F_{live}}{PS} \times \varepsilon_p^{TRD} \times (f'_{p^+} - 1.03 \times f'_{\pi^+} \times C_p^{TRD}) \times \frac{f'_{K^+}}{f'_{K^+} + f'_{p^+}}$$

and the real number of protons in the p' signal is:

$$(N^{+}_{(p',p)})^{inc}_{NODISC} = \sum_{+spills}^{DISC_p<CUT_p^+} TRDGB \bullet \overline{FOLD4} \times \frac{F_{live}}{PS} \times \varepsilon_p^{TRD} \times (f'_{p^+} - 1.03 \times f'_{\pi^+} \times C_p^{TRD}) \times \frac{f'_{p^+}}{f'_{K^+} + f'_{p^+}}$$

The last three elements of the P matrix are then given by:

$$P(p',\pi) = \frac{(N^{+}_{(p',\pi)})^{inc}_{NODISC} + (N_{(p',\pi)})^{inc}_{DISC}}{N^{inc}_{p'}}$$

$$P(p',K) = \frac{(N^{+}_{(p',K)})^{inc}_{NODISC} + (N_{(p',K)})^{inc}_{DISC}}{N^{inc}_{p'}}$$

$$P(p',p) = \frac{(N^{+}_{(p',p)})^{inc}_{NODISC} + (N_{(p',p)})^{inc}_{DISC}}{N^{inc}_{p'}}$$

Elimination of duplicate events and events from bad runs and spills

After reconstruction, the pair strip, the DS3IN1 strip, and the two resonant KKπ strips were complete, the events which passed the last stage of strips were run through a 'weeding' program which removed events from the final data set for a variety of reasons.

It was necessary to remove events from the analysis which came from spills, tapes, or runs which were deemed to be bad or unusual by some signal-independent method. The final scaler counts for the number of incident particles of each type would also not include counts from these spills, tapes, or runs.

The determination of which spills and runs were bad was carried out by examining six independent scaler ratios (see FIGURE 3.41 and TABLE 3.14): the E_T(standard) Pre-Scaler (PS) (TRD • GB / PPI), the E_T(bottom) PS (TRD • GB / PI), the Interaction PS (GB •

TGT INT / INT(PS)), the two livetime measurements discussed earlier (STB FO / BMSTB FI and INT(PS) / PS), and the ratio of the number of DISC 4-fold PMT coincidences to the number of incident particles (KHI / TRD • GB - a measure of the DISC efficiency). A summary of these values, the cuts and the final percentage of events eliminated for each reason is presented in TABLE A.3.

TABLE A.3
Cuts for determining Bad spills, tapes and runs.

Ratio or Value	Cut on Ratio or Value	% of events eliminated from analysis for this reason
R = TRD • GB / PPI (spill)	(R-INT(R+.5))/INT(R+.5) >.025	↓
R = TRD • GB / PI (spill)	(R-INT(R+.5))/INT(R+.5) > .05	↓
R = GB • TGT / INT INT(PS) (spill)	(R-INT(R+.5))/INT(R+.5) > .005	↓
R = STB FO / BMSTB FI (spill)	(R-INT(R+.5))/INT(R+.5) > 1.	↓
R = INT(PS) / PS (spill)	(R-INT(R+.5))/INT(R+.5) > 1.	↓
STB FO / BMSTB FI - INT(PS) / PS	< -0.2	↓
STB FO / BMSTB FI - INT(PS) / PS	> 0.5	↓
R = KHI / TRD • GB (spill)	(R-INT(R+.5))/INT(R+.5) > 1.	~7.3%
fraction of events on tape reconstructed	< 0.90	↓
fraction of events on tape with too many SMD hits	> 0.10	↓
fraction of events on tape with too many fatal DC unpacking problems	> 0.06	↓
Average E_T on tape	> 9.0GeV	~0.6%

For the three PS settings we were able to quantify whether or not the ratio was good by examining the percentage difference between the calculated PS setting and the nearest integer value. The PS value was an integer but the ratio used to calculate the PS setting was a real number usually not equal to an integer due to statistical effects and, possibly, due to real problems (e.g. rate effects) with the PS module. The statistical effects were dominated

by the value of the denominator which counted much slower than the numerator The calculated value of the PS should not differ from an integer by more than 100%/denominator. In practice, we found more variation in the percentage difference than could be accounted for on a purely statistical basis. This effect was understood to be due to rate effects in the PS modules and was not important for normalizing the cross sections. Instead, we eliminated any spills which had PS settings differing by more than $\sim 100/(PS_{min})$ from an integer where PS_{min} was the minimum PS setting for the PS module during the entire running period. If an individual run contained too many spills which were deemed to be bad then the entire run was discarded.

The two livetime measurements were discussed in detail above. In calculating the final livetimes for the experiment we used the $LIVETIME_1$=INTPS2/INTPS measurement. However, in deciding which spills were bad we also examined the difference between the two livetime measurements. When the difference between the two values was too large we eliminated the spill from consideration and, once again, if too many spills from the same run were bad we eliminated the entire run. We also eliminated from consideration any spill which gave an unphysical livetime greater than unity using either of the two techniques.

The DISC4/TRDGB ratio was examined and found to be good throughout all but six spills. In these six spills the ratio was greater than 1 which was physically impossible and these spills were eliminated from consideration.

Events and spills from bad tapes were also eliminated in the 'weeding' program. Bad tapes were found using the information from the PASS0 data base. Unfortunately, the PASS0 information was not available for the 40% of the data which was reconstructed on SiG machines. Bad tapes were defined as tapes for which any of the following conditions were satisfied: less than 90% of the events on the tape were reconstructable, greater than 10% of the events on the tape had too many SMD hits, greater than 6% of the events had too many fatal Drift Chamber data unpacking problems, and tapes for which the average E_T of

the events on tape was greater than 9GeV. Only about 80 tapes were eliminated for these reasons.

When a particular event was duplicated all but one copy of the event were removed. The presence of the duplicate events was an unfortunate consequence of the problems inherent in managing a set of over 10,000 data tapes. With such a large data set it was inevitable that some tapes would be reconstructed or pair stripped two or more times. In the final set of events for the $\phi\pi$ and K^*K strips only about 5% of the events were removed because they were copies of other events. Events were considered to be duplicated if their Run number, SDZ and MASS were identical.

Appendix B

Calculating Statistical and Systematic Errors in the D_S Cross Section

Recall from Appendix A that the calculation of the D_s cross section can be expressed in matrix form as:

$$[\sigma_o] = \frac{1}{B_{D_s \to d}} \left[\sum \frac{R \bullet A^{\alpha} \bullet ACC}{M} \right]^{-1} [NP]^{-1} [N'_{obs}]^{tot}$$

From this matrix equation we can retrieve the expression which gives the nucleon cross section for production of D_s by beam particles of type i ($\sigma_O(i \to D_S)$):

$$\sigma_o(i \to D_s) = \frac{1}{B_{D_s \to d}} \left(\sum \frac{R \bullet A^{\alpha} \bullet ACC}{M} \right)^{-1}_{ii} \sum_{j=\pi,K,p} \left(NP^{-1}\right)_{ij} N^{obs}_{j' \to D_s \to d}$$

Where the observed numbers of D_s is now implicitly the total number found in the entire target. Since the *[R]*, *[A$^{\alpha}$]* and *[ACC]* matrices are all diagonal:

$$\sigma_o(i \to D_s) = \frac{1}{B_{D_s \to d}} \left(\sum_T \frac{R_i(T) A(T)^{\alpha_i^{charm}} ACC(T)_{i \to D_s \to d}}{M(T)} \right)^{-1} \sum_{j=\pi,K,p} \left(NP^{-1}\right)_{ij} N^{obs}_{j' \to D_s \to d}$$

where the variables have the same definition as in Appendix A. $(NP^{-1})_{ij}$ is the element of the ith row and j^{th} column of the inverse of the *NP* matrix. Recall that:

$$M(T) = \frac{1}{N_A} \frac{A(T)}{\rho(T) t(T)}$$

and therefore the nucleon cross section may be written as:

$$\sigma_o(i \to D_s) = \frac{1}{B_{D_s \to d}} \left(\sum_T A(T)^{\alpha_i^{charm}-1} N_A \rho(T) t(T) R_i(T) ACC(T)_{i \to D_s \to d} \right)^{-1} \sum_{j=\pi,K,p} \left(NP^{-1}\right)_{ij} N^{obs}_{j' \to D_s \to d}$$

For convenience we define the following quantities:

$$C(T)_i = N_A A(T)^{\alpha_i^{charm}-1} \rho(T) t(T) R_i(T) ACC(T)_{i \to D_s \to d}$$

$$K_i = \sum_T C(T)_i$$

$$NPN_i = \sum_{j=\pi,K,p} \left(NP^{-1}\right)_{ij} N^{obs}_{j' \to D_s \to d}$$

In this case

$$\sigma_o(i \to D_s) = \frac{1}{B_{D_s \to d}} \frac{1}{K_i} NPN_i$$

To calculate the systematic error introduced in the measurement of the nucleon cross section for D_s we must differentiate the expression for the cross section with respect to every term which has an associated error. The error on the nucleon cross sections due to each of the terms in the above expression (except Avogadro's Number) are as follows:

$$\Delta\sigma_o(i \to D_s)\big|_{\rho(T)} = \left|\frac{\partial\sigma_o(i \to D_s)}{\partial\rho(T)}\Delta\rho(T)\right| = \frac{\Delta\rho(T)}{\rho(T)}\frac{C(T)_i}{K_i}\sigma_o(i \to D_s)$$

$$\Delta\sigma_o(i \to D_s)\big|_{t(T)} = \left|\frac{\partial\sigma_o(i \to D_s)}{\partial t(T)}\Delta t(T)\right| = \frac{\Delta t(T)}{t(T)}\frac{C(T)_i}{K_i}\sigma_o(i \to D_s)$$

$$\Delta\sigma_o(i \to D_s)\big|_{R_j(T)} = \left|\frac{\partial\sigma_o(i \to D_s)}{\partial R_j(T)}\Delta R_j(T)\right| = \delta_{ij}\frac{\Delta R_j(T)}{R_j(T)}\frac{C(T)_i}{K_i}\sigma_o(i \to D_s)$$

$$\Delta\sigma_o(i \to D_s)\big|_{ACC(T)_{j\to D_s\to d}} = \left|\frac{\partial\sigma_o(i \to D_s)}{\partial ACC(T)_{j\to D_s\to d}}\Delta ACC(T)_{j\to D_s\to d}\right|$$

$$= \delta_{ij}\frac{\Delta ACC(T)_{j\to D_s\to d}}{ACC(T)_{j\to D_s\to d}}\frac{C(T)_i}{K_i}\sigma_o(i \to D_s)$$

$$\Delta\sigma_o(i \to D_s)\big|_{B_{D_s\to d}} = \left|\frac{\partial\sigma_o(i \to D_s)}{\partial B_{D_s\to d}}\Delta B_{D_s\to d}\right| = \frac{\Delta B_{D_s\to d}}{B_{D_s\to d}}\sigma_o(i \to D_s)$$

$$\Delta\sigma_o(i \to D_s)\big|_{A(T)} = \left|\frac{\partial\sigma_o(i \to D_s)}{\partial A(T)}\Delta A(T)\right| = \left(\alpha_i^{charm} - 1\right)\frac{\Delta A(T)}{A(T)}\frac{C(T)_i}{K_i}\sigma_o(i \to D_s)$$

$$\Delta\sigma_o(i \to D_s)\big|_{\alpha_j^{charm}} = \left|\frac{\partial\sigma_o(i \to D_s)}{\partial\alpha_j^{charm}}\Delta\alpha_j^{charm}\right|$$

$$= \delta_{ij}\sigma_o(i \to D_s)\frac{\Delta\alpha_j^{charm}}{K_i}\sum_T A(T)^{\alpha_j^{charm}-1}\ln\{A(T)\}\rho(T)t(T)R_i(T)ACC(T)_{i\to D_s\to d}$$

$$\Delta\sigma_o(i \to D_s)\big|_{N^{obs}_{j\to D_s\to d}} = \left|\frac{\partial\sigma_o(i \to D_s)}{\partial N^{obs}_{j\to D_s\to d}}\Delta N^{obs}_{j\to D_s\to d}\right| = \frac{1}{B_{D_s\to d}}\frac{1}{K_i}([NP]^{-1})_{ij}\Delta N^{obs}_{j\to D_s\to d}$$

$$\Delta\sigma_o(i \to D_s)\big|_{([NP]^{-1})_{jk}} = \left|\frac{\partial\sigma_o(i \to D_s)}{\partial([NP]^{-1})_{jk}}\Delta([NP]^{-1})_{jk}\right| = \delta_{ij}\frac{1}{B_{D_s\to d}}\frac{1}{K_j}N^{obs}_{k\to D_s\to d}\Delta([NP]^{-1})_{jk}$$

where the delta function δ_{ij} (equal to 0 for $i \neq j$ and equal to 1 for $i=j$) has been introduced. Note that the statistical error is given by the second to last equation - all other terms represent systematic errors. Note also that the last two equations each represent three separate terms. The square of the total systematic error in the nucleon cross section ($\Delta\sigma_0(i \to D_s)^2$) is given by the quadratic sum of each of the systematic errors given above.

TABLEs B.1 and B.2 list the values and associated errors used in calculating the D_s cross sections.

TABLE B.1
Values Used in the D_s Cross Section Determination for $x_F>0.0$

Quantity	Nominal Value	± Error	Error Type
$B_{D_s \to \phi\pi}$	.027	.007	common
$\frac{B_{D_s \to \phi\pi}}{B_{D_s \to K^*K}}$	0.96	0.11	uncommon
$ACC_{\pi \to D_s \to \phi\pi}$	.0186	.0037	uncommon
$ACC_{K \to D_s \to \phi\pi}$	.0186	.0037	uncommon
$ACC_{p \to D_s \to \phi\pi}$	.0186	.0037	uncommon
$ACC_{\pi \to D_s \to K^*K}$	.0111	.0022	uncommon
$ACC_{K \to D_s \to K^*K}$	.0111	.0022	uncommon
$ACC_{p \to D_s \to K^*K}$	.0111	.0022	uncommon
R_π	.994	.006	common
R_K	.995	.005	common
R_p	.993	.009	common
α_π^{charm}	0.95	0.05	common
α_K^{charm}	0.95	0.05	common
α_p^{charm}	0.95	0.05	common

TABLE B.2
Values Used in the D_S Cross Section Determination for $x_F>0.0$

Quantity	Nominal Value	± Error	Error Type
$N^{obs}_{\pi\to D_s\to\phi\pi}$	9.1	5.1	uncommon
$N^{obs}_{K\to D_s\to\phi\pi}$	6.5	3.0	uncommon
$N^{obs}_{p\to D_s\to\phi\pi}$	1.1	2.5	uncommon
$N^{obs}_{\pi\to D_s\to K^*K}$	19.6	6.3	uncommon
$N^{obs}_{K\to D_s\to K^*K}$	8.3	4.0	uncommon
$N^{obs}_{p\to D_s\to K^*K}$	4.5	3.4	uncommon
$[NP(\pi',\pi)]^{-1}$	6.3×10^{-11}	2.3×10^{-12}	common
$[NP(\pi',K)]^{-1}$	-3.6×10^{-12}	1.5×10^{-12}	common
$[NP(\pi',p)]^{-1}$	-3.5×10^{-12}	6.5×10^{-13}	common
$[NP(K',\pi)]^{-1}$	-1.9×10^{-13}	3.7×10^{-13}	common
$[NP(K',K)]^{-1}$	1.3×10^{-10}	6.5×10^{-12}	common
$[NP(K',p)]^{-1}$	1.1×10^{-14}	1.7×10^{-12}	common
$[NP(p',\pi)]^{-1}$	-1.9×10^{-13}	1.4×10^{-13}	common
$[NP(p',K)]^{-1}$	-6.4×10^{-12}	2.9×10^{-12}	common
$[NP(p',p)]^{-1}$	2.6×10^{-10}	2.8×10^{-11}	common

APPENDIX C

The Maximum Likelihood fit

In order to make use of the maximum amount of information available in the low statistics samples used in the D_s analysis the maximum likelihood method was used to determine the x_F and p_T^2 distributions of the signal. The method is explained in detail elsewhere[62]. This Appendix merely gives the functional forms of the likelihood function used in the fit to the D_s signal.

We define the likelihood function as

$$L \equiv \prod_i \ell(\bar{x}_i, \bar{P})$$

where $\bar{x}_i = (m_i, (x_F)_i, (p_T^2)_i)$

$$\bar{P} = (N_{D_s}, n_{D_s}, b_{D_s}, s, n_B, b_B)$$

The vector **x** contains the mass, x_F and p_T^2 for each candidate as well as an implicit knowledge of the decay mode for the event. The vector P contains the 6 parameters of the maximum likelihood fit. They are in order: the number of D_s in the gaussian signal peak, the n value in a fit to x_F of $(1-x_F)^n$ for the D_s signal, the b value in a fit to $p_T^2$of $\exp(-bp_T^2)$, the slope of a linear background, and the n and b for the background to the D_s. The background x_F and p_T^2 distributions are assumed to be fit by functions of the same form as the signal. This statement is supported by studies of the background in the high statistics $D^{\pm}$ signal. The background x_F and p_T^2 distributions are also assumed to be identical in both decay modes of the D_s.

The fitted values of the parameters are those values which maximize the value of the likelihood function. Since maximizing the logarithm of a function is equivalent to maximizing the function itself it is more common to maximize $\ln(L)$. Since the CERN routine MINUIT minimizes functions I use it to minimize the value of $-2\ln(L)$. The extra

62 Louis Lyons, Statistics for nuclear and particle physicists, Cambridge University Press, 1986.

factor of two is used for a proper error analysis since MINUIT is normally used for χ^2 minimization not the maximum likelihood method.

Each of the terms in the likelihood function must be normalized to unity leading to functions of the following form:

$$\Im \equiv -2\ln L \equiv -2\sum_i \ln \ell(\bar{x}_i, \bar{P})$$

where $$\ell(\bar{x}_i, \bar{P}) \equiv \frac{g \times A_{D_s} \times B_{D_s} + S \times A_B \times B_B}{R_g R_{A_D} R_{B_D} + R_S R_{A_B} R_{B_B}}$$

$$g(m_i, N_{D_s}) = \frac{N_{D_s}}{\sigma\sqrt{2\pi}} \exp\left(-\frac{1}{2}\left[\frac{m_i - m_{D_s}}{\sigma}\right]^2\right)$$

$$A_{D_s}[(x_F)_i, n_{D_s}] = ACC[(x_F)_i]\,|1-(x_F)_i|^{n_D}$$

$$B_{D_s}[(p_T^2)_i, b_{D_s}] = ACC[(p_T^2)_i]\exp[-b_{D_s}(p_T^2)_i]$$

$$S(m_i, s) = (N_{tot} - N_{D_s})\frac{[1 + s(m_i - m_{D_s})]}{(m_H - m_L) + s\left[\frac{m_H^2 + m_L^2}{2} - m_{D_s}(m_H - m_L)\right]}$$

$$A_B[(x_F)_i, n_B] = ACC[(x_F)_i]\,|1-(x_F)_i|^{n_B}$$

$$B_B[(p_T^2)_i, b_B] = ACC[(p_T^2)_i]\exp[-b_B(p_T^2)_i]$$

The width (σ) and location $m(D_s)$ of the gaussian (g) representing the D_s peak were fixed at 10MeV and 1.972GeV respectively as suggested by fits to the D_s signal with the highest statistics (see Chapter 6). m_H and m_L are the highest and lowest event masses allowed in the fit. They were 2.07 and 1.9 GeV respectively. N_{tot} is the total number of entries in the fit. Each of the functions R_i are the normalizations of the respective function i integrated over the allowed range of the variable.

Since $m_H - m(D_s) >> \sigma$ and $m(D_s) - m_L >> \sigma$ R_g is simply the number of D_s in the peak. Then, using the function S for the background R_S is just the number of events not in the peak.

The ACC are acceptance functions for the specified variable where different acceptance functions must be used for each of the two possible decay modes. Plots of the acceptance in

x_F and p_T^2 may be found in FIGUREs 6.3 and 6.4. The acceptances have been fit to fourth order polynomials. e.g. $ACC(x_F) = a + bx_F + cx_F^2 + dx_F^3 + ex_F^4$ and $ACC(p_T^2) = a + bp_T^2 + c(p_T^2)^2 + d(p_T^2)^3 + e(p_T^2)^4$. The values of the parameters in these fits are shown in TABLE C.1 The acceptance is assumed to be flat in the mass of the D_s candidates.

The normalizations R_A and R_B can be determined by integrating the functions A and B over the range of x_F and p_T^2 of interest:

$$
\begin{aligned}
R_A &= \int_0^1 ACC(x_F)(1-x_F)^n \\
&= \int_0^1 (a + bx_F + cx_F^2 + dx_F^3 + ex_F^4)(1-x_F)^n \\
&= \frac{(a+b+c+d+e)}{n+1} - \frac{(b+2c+3d+4e)}{n+2} + \frac{(c+3d+6e)}{n+3} - \frac{(d+4e)}{n+4} + \frac{e}{n+5} \\
R_B &= \int_0^{10} ACC(p_T^2)\exp(-bp_T^2) \\
&= \int_0^{10} [a + b(p_T^2) + c(p_T^2)^2 + d(p_T^2)^3 + e(p_T^2)^4]\exp(-bp_T^2) \\
&\equiv \int_0^{10} [P_0 + P_1(p_T^2) + P_2(p_T^2)^2 + P_3(p_T^2)^3 + P_4(p_T^2)^4]\exp(-bp_T^2) \\
&= \sum_{m=0}^{4} P_m m! \left[\frac{1}{b^{m+1}} - \exp(-10b) \sum_{n=0}^{m} \frac{10^{m-n}}{(m-n)!\,b^{n+1}} \right]
\end{aligned}
$$

where, of course, the appropriate set of parameters (a,b,c,d,e) are used for each decay mode and x_F or p_T^2.

In the calculation of the D_s relative and total cross sections only the total number of D_s produced by each beam particle type is required. In this case the maximum likelihood method was utilized once again for the much simplified case

$$\Im \equiv -2 \ln L \equiv -2 \sum_i \ln \ell(\overline{\mathbf{x}}_i, \overline{\mathbf{P}})$$

$$\ell(\overline{\mathbf{x}}_i, \overline{\mathbf{P}}) \equiv \frac{g + S}{N_{tot}}$$

where the definitions of the functions have not changed.

TABLE C.1
Coefficients of the fits to the Acceptance Functions

	x_F acceptance		p_T^2 acceptance	
	$D_s \to \phi\pi$	$D_s \to K^*K$	$D_s \to \phi\pi$	$D_s \to K^*K$
a	0.0020±0.0010	-0.00022±0.00099	0.0181±0.0011	0.0108±0.0011
b	0.342±0.015	0.224±0.014	0.0070±0.0013	0.0037±0.0013
c	-1.254±0.057	-0.780±0.055	-0.00210±0.00045	-0.00024±0.00045
d	1.69±0.13	1.03±0.12	0.000338±0.000079	-0.000076±0.000080
e	-0.82±0.14	-0.50±0.13	-0.0000188±0.0000059	0.0000087±0.0000059

List of Publications

* published in referreed journal

R. Jedicke, E769 - Hadronic Production of Charm, Physics in Canada, Vol. 45, No. 4, July 1989, p. 105.

*R. Jedicke, Neutrino detectors as early warning devices for supernovae, J. Roy. Astron. Soc. Can., Vol. 83, No. 2, 1989, p. 116.

*D. Errede, M. Sheaff, H. Fenker, L. Lueking, P. Mantsch and R. Jedicke, A High Rate Transition Radiation Detector for particle Identification in a hadron beam, submitted to NIM.

List of Published Talks presented by E769 members

P. Karchin for J.C. Anjos et al., Charm Photo-production results from Fermilab E691 and prospects for Hadro-production in E769, Nuclear Physics B (Proc. Suppl.) 7B (1989) 60-68.

L. Lueking for G. A. Alves et al., Hadroproduction of Charm at Fermilab E769, presented at the 1990 Meeting of the DPF of the APS, Houston, Texas, 3-6 January, 1990.

A. Napier for G.A. Alves et al., Hadro-production of charm and charm-strange states at Fermilab E-769, presented at XXIV Recontre de Moriond, Hadronic Interactions, Les Arcs, France, 12-18 March, 1989.

C. Stoughton for G.A. Alves et al., Beam particle tagging and tracking for FNAL E769, presented at APS-Baltimore, April 20, 1988.

D.J. Summers for G.A. Alves et al., Charm Hadroprodution at Fermilab E769, presented at XXIII Recontres de Moriond, Issues in Hadron Physics, Les Arcs, France, 13-19, March 1988.

R. Jedicke and L. Lueking for G.A. Alves et al., Hadroproduction of Charm at Fermilab E769, presented at the 1991 Meeting of the DPF of the APS, Vancouver, BC, Canada, 17-22 August, 1991.